Structured Environments and Engineered Dissipation in Superconducting Circuits

Bound States, Dissipative Phase Transitions, Purcell Filtering and Power Sensors

Claudia Castillo-Moreno



Department of Microtechnology and Nanoscience CHALMERS UNIVERSITY OF TECHNOLOGY Göteborg, Sweden 2025 Structured Environments and Engineered Dissipation in Superconducting Circuits Bound States, Dissipative Phase Transitions, Purcell Filtering and Power Sensors CLAUDIA CASTILLO-MORENO ISBN 978-91-8103-317-5

© CLAUDIA CASTILLO-MORENO, 2025.

Doktorsavhandlingar vid Chalmers tekniska högskola Ny serie nr 5774 ISSN 0346-718X

Department of Microtechnology and Nanoscience Chalmers University of Technology SE–412 96 Göteborg, Sweden Telephone + 46 (0)31 - 772 1000

Typeset by the author using LaTeX.

Printed by Chalmers Reproservice Göteborg, Sweden 2025

Abstract

Superconducting circuits are a powerful platform for studying and controlling the interaction between light and matter at the quantum level. In these systems, superconducting qubits act as artificial atoms (with matter-like degrees of freedom), whereas microwave resonators play the role of oscillators hosting photons (with photonic-like degrees of freedom). A major advantage of this platform is the ability to tailor the electromagnetic environment to which the qubits are coupled. This degree of control makes it possible to realize well-known quantum optics models, like the Jaynes-Cummings model, as well as more complex systems, like quantum electrodynamics close to a bandgap.

In this thesis, we engineer structured electromagnetic environments and couple superconducting qubits to them to experimentally study their interaction. By coupling multiple microwave resonators together, we create a metamaterial. When an atom interacts with the metamaterial, an atom-photon bound state emerges. We observe the dynamics of the creation and dissolution of the atom-photon bound state, as well as the spectral content of its photonic component, for the first time to our knowledge. Our metamaterial is intrinsically nonlinear because each resonator is formed by an array of Josephson junctions to serve as an inductor. When the system is pumped, its phase diagram exhibits multimode dissipative phase transitions with timescales on the order of hundred seconds. There is ongoing theoretical debate about whether such phase transitions can occur in one-dimensional systems, a question we address and resolve in this work.

Furthermore, we engineer qubit decay using two different approaches. In the first one, we engineer the decay of two coupled atoms to two waveguides by using a symmetric—antisymmetric coupling configuration. This approach enables selective coupling to bright and dark states of the system. In the second one, we suppress the Purcell decay of a qubit using a compact lumped-element Purcell filter. In addition, we characterize the Purcell decay by employing an auxiliary superconducting qubit as a sensitive power detector directly coupled to the feedline waveguide used for the qubit readout.

In summary, this thesis presents three different methods for controlling light—matter interactions in structured quantum systems, including decay suppression with both Purcell filters and symmetry-selective couplings. The thesis also introduces new experimental techniques for probing atom-photon bound states and provides direct evidence of collective phenomena in driven-dissipative quantum metamaterials.

Keywords: Metamaterial, superconducting circuits, high-impedance resonators, lumped resonators, dissipative phase transitions, Purcell filters, waveguide quantum electrodynamics

Acknowledgments

First of all, I would like to thank my supervisor, Simone Gasparinetti, for believing in me and giving me the opportunity to pursue these doctoral studies. I was always very inspired by his determination and critical thinking.

I would like to thank Mohammed Ali Aamir for all the fun we had starting the lab, for being so helpful at all times, and for his guidance throughout my PhD. My thanks go as well to Kazi Rafsanjani Amin for spending countless evenings working together and for teaching me how to keep going and maintain an optimistic attitude, even when we were exhausted. To Ingrid Strandberg, thank you for sitting with me to solve Hamiltonians, Schrödinger equations, and input-output theory together. I truly appreciated having you as a female figure to look up to. To Axel Eriksson and Lukas Splithoff, thank you for your support, encouragement, and assistance throughout this journey. To Mikael Kervinen for spending time in the cleanroom with me.

To my much-appreciated theory collaborators, Timo Hillmann and Théo Sépulcre, thank you for always being open to discussing and sharing ideas, and for engaging with my project. Your enthusiasm for physics and the topic of phase transitions kept me motivated and excited to continue. I am also grateful for our coffee breaks and the positive energy you always brought.

To all of my current and past colleagues — Claire, Simon, Kunal, Vyom, Niranjan, Ludvig, Linus, Kiwmann, Saba, Vittorio, Thomas, Zheshu, Awse, Núria, Alberto, Hanna, Alejandro, Anuj, Achintya, Joey, Paul, Pietro, Veronika, Antoni, Martin, Marina, Francois, Pranjal, Sogeta, Marco — thank you for your encouragement, humor, and for creating a healthy and welcoming working environment. I truly enjoyed the time we spent together, filled with interesting conversations, discussions, and laughter.

To my Gothenburg girls — Alina, Aytan, and Lakshidaa — having you as friends has been one of the best things during these five years, and I am glad to think of you as family now. To the rest of my Gothenburg gang — Raj, Prashanth, Alex, Elliot, Hilda, Sam, William, Linnea, Marina, Nena — thank you for all the fun times we shared playing board games, karaoke, reading books, and in midsummer. To my Drailonitos — Juan Carlos, Drilon, and Albert — thank you for spending all the WACQT events together. To my dancing friends — Hannah, Maryam, Oscar, Erik, Anders, Nicolina, Tessa, Felicia, Maria, and Daniel — it was a pleasure to get to know you, laugh with you, and dance together. To Veronica and Pujita, our conversations healed and filled me with joy and understanding. To my friends back home, Agostina, Irene, Judit, Manuel, Ernesto, Julio, Carmen, Teresa, and María,

thank you for being there after all these years.

To my parents, my sister, nephew, niece and the rest of my family, thank you for your endless love and support. Even when we are so far away, I still feel your love every day. To Sofia, whose support helped me find balance and resilience when I needed it most, this thesis would not have been possible without you. And thanks to Joaquin for being the place I can call home. Thank you for your daily support, your love, and your constant encouragement. Thank you for being silly with me, for dancing, laughing, cooking, and turning the most mundane moments into the most joyful ones. I love you.

Claudia Castillo-Moreno Göteborg, October 2025

List of Publications

This thesis is based on the following appended papers:

- Paper 1 Claudia Castillo-Moreno, Kazi Rafsanjani Amin, Ingrid Strandberg, Mikael Kervinen, Amr Osman, and Simone Gasparinetti. *Dynamical excitation control and multimode emission of an atom-photon bound state*. Physical Review Letters 160, 123604 (2025).
- Paper 2. Claudia Castillo-Moreno, Théo Sépulcre, Timo Hillmann, Kazi Rafsanjani Amin, Mikael Kervinen, and Simone Gasparinetti. Experimental observation of multimode quantum phase transitions in a superconducting Bose-Hubbard simulator. arXiv:2508.20116.
- Paper 3. Claudia Castillo-Moreno, Kunal Helambe, Simona Zaccaria, Thomas Descamps, Antonio Gnudi, Mohammed Ali Aamir, and Simone Gasparinetti. Compact Purcell Filter Based on Josephson-Junction Array Resonators Achieving 3 ms Purcell Decay for Tri-State Qubit Readout. In preparation.
- Paper 4. Mohammed Ali Aamir, Claudia Castillo-Moreno, Simon Sundelin, Janka Biznárová, Marco Scigliuzzo, Kowshik Erappaji Patel, Amr Osman, D. P. Lozano, Ingrid Strandberg, and Simone Gasparinetti. Engineering Symmetry-Selective Couplings of a Superconducting Artificial Molecule to Microwave Waveguides. Physical Review Letters 129, 123604 (2022).

Other relevant publications co-authored by Claudia Castillo-Moreno:

- Paper A. Mohammed Ali Aamir, Paul Jamet Suria, José Antonio Marín Guzmán, Claudia Castillo-Moreno, Jeffrey M. Epstein, Nicole Yunger Halpern, and Simone Gasparinetti. *Thermally driven quantum refrigerator autonomously resets superconducting qubit.* Nature Physics volume 21, pages 318–323 (2025).
- Paper B. Jiaying Yang, Axel Martin Eriksson, Mohammed Ali Aamir, Ingrid Strandberg, Claudia Castillo-Moreno, Daniel Perez Lozano, Per Persson, and Simone Gasparinetti. *Deterministic generation of shaped single microwave photons using a parametrically driven coupler*. Physical Review Applied 20, 054018 (2023).

- Paper C. Axel Martin Eriksson, Théo Sépulcre, Mikael Kervinen, Timo Hillmann, Marina Kudra, Simon Dupouy, Yong Lu, Maryam Khanahmadi, Yiaying Yang, Claudia Castillo-Moreno, Per Delsing, and Simone Gasparinetti. *Universal control of a bosonic mode via drive-activated native cubic interactions*. Nature Communications volume 15, Article number: 2512 (2024).
- Paper D. Jiaying Yang, Ingrid Strandberg, Alejandro Vivas-Viaña, Akshay Gaikwad, Claudia Castillo-Moreno, Anton Frisk Kockum, Muhammad Asad Ullah, Carlos Sánchez Muñoz, Axel Martin Eriksson, and Simone Gasparinetti. Entanglement of photonic modes from a continuously driven two-level system. npj Quantum Information volume 11, Article number: 69 (2025).
- Paper E. Jiaying Yang, Maryam Khanahmadi, Ingrid Strandberg, Akshay Gaikwad, Claudia Castillo-Moreno, Anton Frisk Kockum, Muhammad Asad Ullah, Göran Johansson, Axel Martin Eriksson, and Simone Gasparinetti. *Deterministic generation of frequency-bin-encoded microwave photons*. Physical Review Letters 134, 240803 (2025).
- Paper F. Simon Sundelin, Mohammed Ali Aamir, Vyom Manish Kulkarni, Claudia Castillo-Moreno, and Simone Gasparinetti. Quantum refrigeration powered by noise in a superconducting circuit. arXiv:2403.03373.(2024)

List of Acronyms

1D – One Dimensional

ADC – Analog-to-Digital Converter AWG – Arbitrary Waveform Generator

CPW – Coplanar Waveguide LO – Local Oscillator

QED – Quantum Electro-Dynamics RWA – Rotating Wave Approximation

SQUID - Superconducting Quantum Interference Device

TLS – Two-Level System

VNA – Vector Network Analyzer

WQED - Waveguide Quantum Electrodynamics CQED - Circuit Quantum Electrodynamics

TEM – Transverse electromagnetic

grAl – Granular aluminum

JCM – Jaynes-Cummings model

RF – Radiofrequency

FFT – Fast Fourier Transform APBS – Atom-photon bound state

JJ – Josephson junction

HEMT - High Electron Mobility Transistor

EBL – Electron-Beam LithographyPVD – Physical Vapor Deposition

Contents

A	bstra	et	5
A	cknov	wledgments	7
Li	st of	Publications	9
Li	st of	Acronyms	11
Ι	In	troduction	1
1	Cor 1.1	ntrol light-matter interactions Thesis outline	3
2	Circ	cuit QED Building Blocks	5
	2.1	Introduction	5
	2.2	Coplanar waveguides	5
	2.3	Resonators	
		2.3.1 Distributed resonators	
	2.4	2.3.2 Lumped resonators	
	2.4	Transmon qubit as an atom	
	2.5	Coupling between the elements	
	2.6	2.5.1 Capacitive and inductive coupling	
	$\frac{2.0}{2.7}$	Lindblad master equation	12
	2.8	Black-box superconducting circuit quantization	
II	\mathbf{E}	xperimental results	15
3	Tail	oring the decay rates of artificial atoms and molecules	17
-	3.1	Introduction	
	3.2	Direct coupling of an atom to a waveguide	18
		3.2.1 Emitted field	18
		3.2.2 Input-output theory and scattering parameters	19
	3.3	Selective coupling of a molecule to two waveguides	20

CONTENTS CONTENTS

		3.3.1 Experimental implementation	20
		3.3.2 Formation of the molecule	20
		3.3.3 Selective coupling to the waveguide	21
	3.4	Purcell filter and characterization of the Purcell decay	23
		3.4.1 Experimental implementation	24
		3.4.2 Characterization of the device	25
		3.4.3 Single-shot measurements	27
		3.4.4 Measurement of Purcell decay	30
		3.4.5 Conclusion	32
4	Quk	oits coupled to metamaterials based on Josephson-junction ar-	
	rays		33
	4.1	Introduction	33
	4.2	Metamaterials	34
		4.2.1 Experimental implementation	34
		4.2.2 Tight-binding model Hamiltonian	35
		4.2.3 Scattering parameters	36
		4.2.4 Transmission band	36
	4.3	Atom-photon bound states	37
		4.3.1 Experimental implementation	38
		4.3.2 Tight-binding model Hamiltonian	38
	4.4	4.3.3 Effective model Hamiltonian	39
	4.4	Characterization of the device	39
	4.5	Dynamics in the formation and melting of an atom-photon bound state	41
	4.6	Emission of an atom-photon bound state	43
	4.7	Control of the emission of an atom-photon bound state	45
	4.8	Discrepancies between experimental results and the effective model .	45
	4.9	Conclusion	47
5		sipation engineering and emergent dynamics in a metamaterial	
	5.1	Introduction	49
	5.2	Liouvillian interpretation of first-order dissipative phase transitions .	50
		5.2.1 Liouvillian	50
		5.2.2 Dissipative phase transitions	51
	F 9	5.2.3 First-order dissipative phase transition	51
	5.3	Experimental implementation	51
	5.4	Theoretical model	53 54
	5.5	Observation of multimode phase transitions	54 57
	5.6	Emission from the phase transition and phase diagram	57
	5.7	Dynamics of the transition	58 62
	5.8	Conclusion	62

CONTENTS CONTENTS

ΙΙ	I Conclusion	63
6	Conclusion and outlook 6.1 Outlook	65 66
ΙV	Appendix	69
7	Methods 7.1 Introduction	71 73 74 74 74
Bi	bliography	77
\mathbf{V}	Appended papers	93
1	Dynamical Excitation Control and Multimode Emission of an Ato Photon Bound State	om- 95
2	Experimental observation of multimode quantum phase transition in a superconducting Bose-Hubbard simulator	ons 111
3	Compact Purcell Filter Based on Josephson-Junction Array R onators Achieving 3 ms Purcell Decay for Tri-State Qubit Reado	
4	Engineering Symmetry-Selective Couplings of a Superconducti Artificial Molecule to Microwave Waveguides	ng 143

Part I Introduction

Chapter 1

Control light-matter interactions

The study of light–matter interactions lies at the heart of modern quantum physics. From the first demonstrations of cavity quantum electrodynamics (QED) with atoms in optical cavities [1, 2] to today's circuit-based realizations using superconducting qubits [3–5], controlling how a quantum emitter couples to its electromagnetic environment has enabled profound advances in our understanding of coherence, entanglement, and measurement. In recent years, the ability to engineer the environment itself, through artificial structures such as metamaterials [6–8], has opened entirely new regimes of quantum control.

Circuit quantum electrodynamics (cQED) provides a uniquely powerful platform to study these questions [5, 9]. Superconducting qubits coupled to engineered microwave environments combine strong nonlinearity, long coherence times, and nearly arbitrary design flexibility. By constructing networks of resonators, transmission lines, and Josephson-junction-based metamaterials, one can tailor both the density of photonic states and the dissipative pathways available to the system [10–12]. This level of control enables experiments that probe the interface between quantum optics, condensed matter, and non-equilibrium statistical physics [6, 13, 14].

In waveguide quantum electrodynamics (wQED) [9, 15, 16], emitters are coupled to one-dimensional photonic continua, either open transmission lines [10, 17] or photonic structures with engineered spectral features, such as metamaterial waveguides [12, 18, 19]. Unlike conventional cavity QED systems, where interactions are confined to discrete resonant modes, waveguide QED enables light–matter coupling in open, broadband, and spectrally structured environments. This setting allows for the exploration of phenomena such as collective effects [20–28], non-Markovian dynamics [29, 30], and the formation of atom–photon bound states [12, 18, 31, 32]. These effects highlight the potential of engineered one-dimensional photonic systems as versatile platforms for both fundamental studies of open quantum systems and applications in scalable quantum technologies.

In this thesis, we explore how the coupling to the environment can be designed to control light–matter interactions in superconducting quantum circuits. We present a series of experiments that collectively demonstrate how engineering both the photonic spectrum and the dissipative channels of a quantum system can give rise to new regimes of quantum dynamics. These include the controlled engineering of qubit

4 1.1. Thesis outline

decay through symmetry and Purcell filtering, the realization and characterization of atom—photon bound states in metamaterials, and the observation of multimode dissipative phenomena in nonlinear resonator arrays. Together, these results establish new ways to control and understand light-matter interactions in superconducting quantum systems, showing how engineering the environment and the coupling to it can be used as a powerful tool for quantum science.

1.1 Thesis outline

This thesis is organized into four main chapters.

Chapter 2 establishes the experimental and theoretical foundations on which the subsequent work is built. It introduces the design principles of artificial atoms and quantum resonators, explains their mutual interaction through the Jaynes–Cummings model, and describes their interaction with the environment within the Lindblad master equation formalism.

Chapter 3 examines how decay rates to the environment can be engineered in two distinct systems. The first, discussed in Paper 4, consists of an artificial molecule directly coupled to the environment, where selective coupling into two separate waveguides is achieved. The second system, presented in Paper 3, features an atom dispersively coupled to a lumped-element readout resonator. Here, the insertion of a Purcell filter between the resonator and the feedline suppresses the Purcell decay, while an auxiliary transmon directly coupled to the waveguide enables its direct measurement.

Chapter 4 goes one step forward by structuring the waveguide to which the atom is coupled to. We engineer the waveguide into a metamaterial with transmission bands and bandgaps. When the atom is coupled at the edge of the transmission band of the metamaterial, the excitation gets trapped around the physical position of the resonator that the emitter is coupled to, giving rise to an atom-photon bound state. In Paper 1, we explore the formation of this state and demonstrate direct measurement of its photonic component following a quench.

Finally, Chapter 5 explores the physics that occur in such metamaterial when the system is strongly driven. In this setting, a dissipative phase transition emerges between a quantum, weakly populated dim state and a semiclassical, highly populated bright state. The detailed study of this transition is presented in Paper 2.

We give a conclusion and outlook for future studies in Chapter 6.

Chapter 2

Circuit QED Building Blocks

2.1 Introduction

In this chapter, we review the essential building blocks of the circuit quantum electrodynamics (cQED) framework that underpin the experiments presented throughout this thesis. Circuit QED provides a versatile platform for engineering quantum light—matter interactions by integrating microwave photonic structures with non-linear superconducting elements. A clear understanding of these components and how they couple is essential for interpreting the results discussed in the following chapters.

This chapter is organized as follows. Section 2.2 introduces the coplanar waveguides that define our feedlines. Section 2.3 discusses microwave resonators, one of the central elements of the framework. In Section 2.4, we present the transmon, which serves as an artificial atom and plays a central role in our work. Section 2.5 describes the mechanisms by which these elements are coupled in superconducting circuits. Section 2.6 introduces the Jaynes–Cummings Hamiltonian as the theoretical model governing the interactions between elements arising from their couplings. Finally, Section 2.7 outlines the Lindblad master equation, which provides the framework to account for environmental effects and dissipation.

2.2 Coplanar waveguides

A coplanar waveguide (CPWs) is a type of transmission line used ubiquitously in superconducting circuits. CPWs are coplanar structures – all conducting elements lie in the same plane – fabricated on a dielectric substrate. Their standard geometry, in Fig. 2.1, consists of three superconducting strips: A central signal-carrying strip and a pair of ground conductors side-strips, running parallel to the signal strip. These structures are deposited on a dielectric substrate such as silicon. The propagating mode has both the electric and magnetic field components perpendicular to the propagation direction (TEM mode) [33].

A waveguide is described by a collection of propagating photonic modes with a wavevector k and corresponding frequency ω_k . Therefore, their Hamiltonian is

6 2.3. Resonators

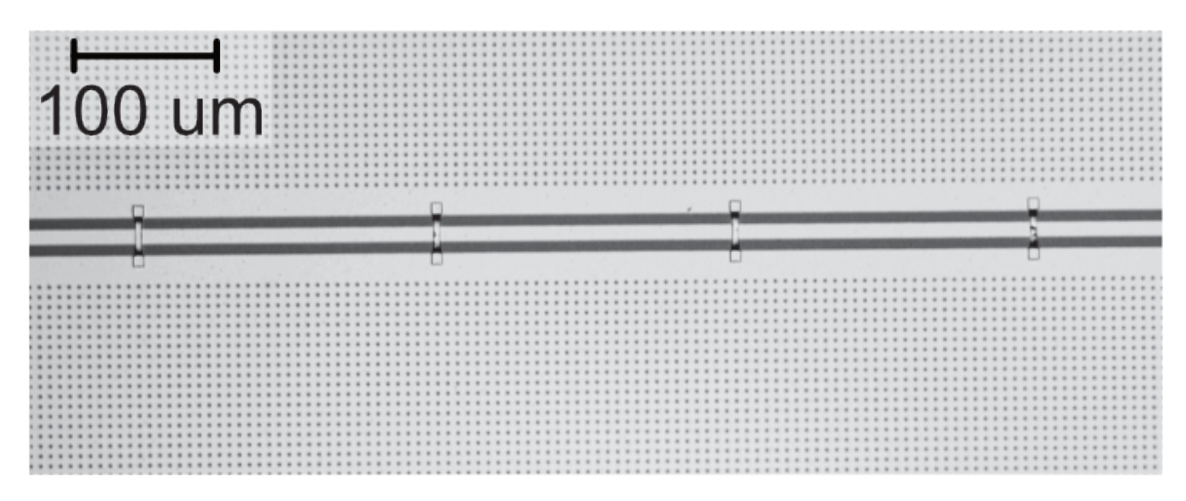


Figure 2.1: Micrograph of a standard CPW design in circuit QED. Superconducting material is in light gray, the dielectric is in dark gray.

$$H_{\text{field}} = \sum \hbar \omega_k a_k^{\dagger} a_k \tag{2.1}$$

Or, in the continuum limit

$$H_{\text{field}} = \int \hbar \omega_k \, a_k^{\dagger} a_k \, dk \tag{2.2}$$

In this expression, ω_k is the angular frequency of the photonic mode energy with wavevector k, a_k^{\dagger} (a_k) is its corresponding creation (annihilation) operator. These operators satisfy the canonical commutation relation $\left[a,a^{\dagger}\right]=1$; \hbar is the reduced Planck constant.

2.3 Resonators

Superconducting microwave resonators possess photon-like degrees of freedom. Their Hamiltonian, derived from an LC circuit and after using second quantization, takes the form:

$$H = \hbar\omega \left(a^{\dagger} a + \frac{1}{2} \right) \tag{2.3}$$

Here, ω is the angular frequency of the resonator. The term $\frac{1}{2}\hbar\omega$ represents the zero-point energy, which does not affect the dynamics and will be omitted in the following.

The resonator behaves as a quantum harmonic oscillator with an infinite ladder of equally spaced energy levels. Their energy is given by

$$E_n = \hbar\omega \left(n + \frac{1}{2}\right), \quad n = 0, 1, 2, \dots$$
 (2.4)

The quantum number n corresponds to the number of photons in our resonator, and corresponds to the Fock state $|n\rangle$. A schematic of a resonator and its energy-level scheme is given in Fig. 2.2. LC resonators in circuit QED play a central role and

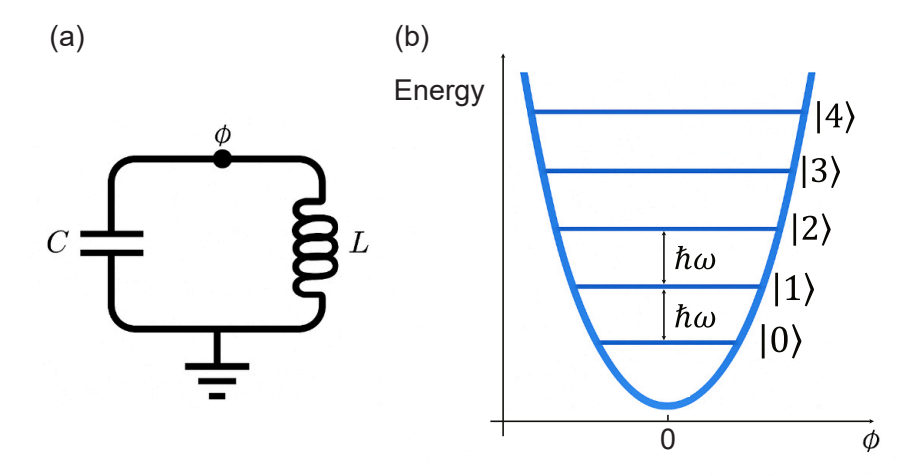


Figure 2.2: Quantum resonator diagrams. (a) Circuit diagram. (b) Harmonic energy diagram.

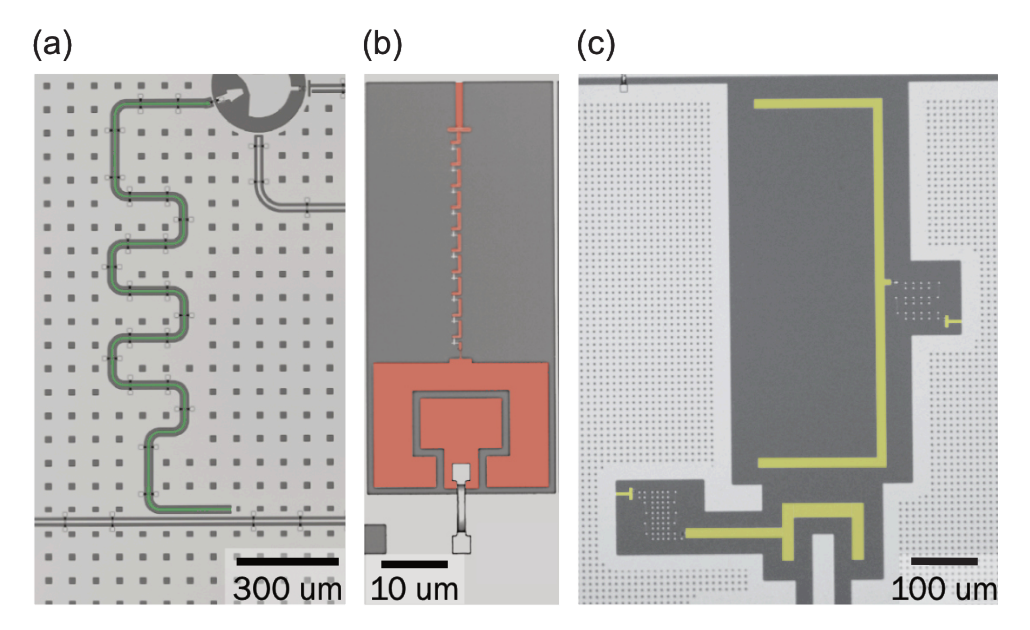


Figure 2.3: False-colored micrographs of different resonator designs in Papers 1, 2, 3. (a) Distributed resonator, (b) Lumped resonator with Josephson junctions, (c) Two lumped resonators with Josephson junctions.

their applications include reading out the qubit state [3] and as unit of computation in continuous variable quantum computing [34, 35].

Depending on their spatial structure we can define two types: Distributed linear resonators and lumped resonators. In Fig. 2.3, we present three different false-colored images of the resonators that were used in Papers 1, 2, 3.

8 2.3. Resonators

2.3.1 Distributed resonators

When a CPW is terminated on both ends with either a short or open boundary conditions, it becomes a distributed resonator, supporting a discrete set of standing-wave modes. The resonant frequencies are determined both by the length and boundary conditions at the ends.

If both ends have the same boundary conditions, either open or shorted, it is a $\lambda/2$ -resonator. In this case, the resonator resonates at frequencies for which the length of the resonator is an integer multiple of $\lambda/2$. On the other hand, if the resonator has asymmetric boundary conditions, one open and the other one shorted, it is a $\lambda/4$ -resonator. In this case, it resonates at frequencies for which the length of the resonator is an integer multiple of $\lambda/4$. These modes have a voltage node at the grounded end and a voltage antinode at the open end. Distributed resonators are widely used in circuit QED because their resonance frequency is set primarily by their physical length, which makes them easy to design and fabricate.

In Paper 1, a $\lambda/4$ -resonator has been used to readout the state of the qubit through dispersive readout [5, 36]. Its microscope picture is false-colored in green in Fig. 2.3(a). In this picture, we observe how the lower end of the meandering structure is left shorted to ground and the one on the top is left open.

2.3.2 Lumped resonators

For scalability of superconducting circuits, compact alternatives to the standard CPW resonators are highly desired. When the physical size of a resonator is much smaller than the wavelength at its resonant frequency, the resonator can be modeled as a lumped LC-circuit. In the frequencies of our interest, this limit occurs when the resonator is less than 3 mm (approximately ten times smaller than the wavelength). Unlike distributed resonators, lumped resonators rely on an inductor (L) and a capacitor (C) to define the resonance frequency, according to

$$\frac{\omega_r}{2\pi} = \frac{1}{2\pi\sqrt{LC}}\tag{2.5}$$

In order to reach the resonant frequencies in the nominal range of $4-8~\mathrm{GHz}$, high inductances are required in the lumped resonators. Three different approaches are commonly used. The first one is to use of high-kinetic inductance materials, such as granular aluminum (grAl), TiN [37] or NbN [38] for the fabrication of the resonators. This approach requires the development of new fabrication techniques. The second one is to use special geometric inductances of superconducting wires, usually thin spiral resonators [12, 39, 40], which require very large elements and precise control of their geometry. The third approach is to integrate arrays of Josephson junctions, which have a large inductance in a compact geometry [41]. However, they introduce non-linearity to the inductance.

In Papers 1 and 2, Fig.2.3(b), our metamaterial array is composed of 21 lumped non-linear resonators with dimensions on the order of 200 μ m, far below the limit. In Paper 3, Fig.2.3(c), we use this type of compact resonator to readout the state of our qubit and as Purcell filters, with dimensions between 100 and 600 μ m. In

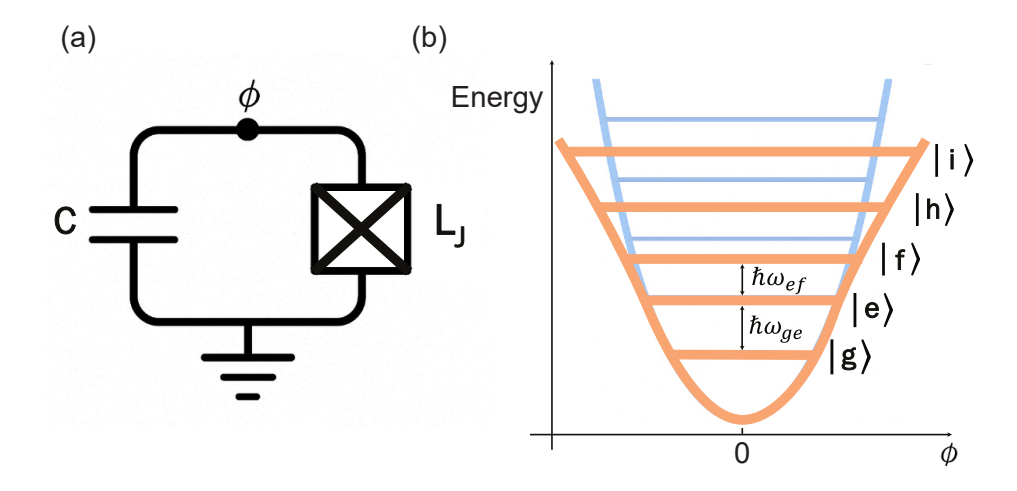


Figure 2.4: **Transmon diagrams.** (a) Circuit diagram. (b) Anharmonic energy diagram in orange compared to the harmonic diagram of the harmonic oscillator in blue.

comparison to the previous approaches mentioned here, our approach uses the high inductance of the Josephson junctions. Still, its non-linearity is scaled by the number of Josephson junctions in series [42], which ranges between 10 and 55.

2.4 Transmon qubit as an atom

The transmon qubit is a superconducting circuit composed of two superconducting elements forming a capacitor as well as shunted via a Josephson junction, which acts as a nonlinear inductor [43, 44]. Together, these components form a quantum anharmonic oscillator, in which the capacitor stores the kinetic (or charging) energy, and the inductor stores the potential (or inductive) energy. The Hamiltonian of the transmon in the second quantized form, is:

$$H = \omega_{\mathbf{q}} b^{\dagger} b + \frac{\alpha}{2} b^{\dagger} b^{\dagger} b b \tag{2.6}$$

In this expression, $\omega_{\rm q}$ is the qubit transition frequency given by $\omega_{\rm q} = \sqrt{8E_JE_C} - E_C$, and α the anharmonicity given by $\alpha = -E_c$. The anharmonicity is crucial: it breaks the degeneracy between transitions, allowing individual energy levels to be addressed [5, 9, 36]. If we compare this Hamiltonian to the quantum resonator in equation 2.3, we observe that their difference is the non-linear term arising from the Josephson junction. The transmon circuit and energy diagram is in Fig.2.4.

If we limit the Hilbert space to the first two levels, this Hamiltonian can be reduced to:

$$H = \frac{1}{2}\hbar\omega_q \sigma_z \tag{2.7}$$

where σ_z is the Pauli z-matrix. Since the transition between the ground state and the first excited state can be well isolated from higher-order transitions, the

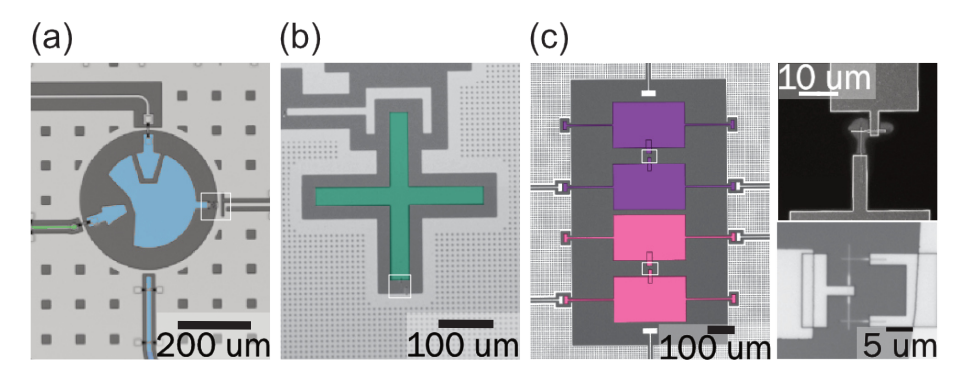


Figure 2.5: False colored micrographs of the different transmon geometries in this thesis. (a) Transmon design with a circular shape colored in blue, from Paper 1. (b) Standard X-mon for Paper 3, (c) Two split transmons for Paper 4. Top inset: SEM picture of JJ similar to the one in the white squares in designs (b) and (c). Bottom inset: Microscope picture of the SQUID in the white square in (a).

transmon is commonly regarded as a two-level system, and we use the Hamiltonian in 2.7 as an approximation at low powers.

In addition, to mitigate sensitivity to charge noise, the transmon is typically operated in the regime $E_J/E_C \geq 50$. In this regime, the energy bands flatten with respect to offset charge, and the qubit energy levels become exponentially less dependent on charge noise. Transmons are designed with a anharmonicity of the order of 200 MHz.

In Fig.2.5, we show the optical micrographs of transmons of various geometries that were used in the Papers of this thesis. Each micrograph also features an inset zooming in on the device's Josephson junction or Superconducting Quantum Interference Device (SQUID), which consists of two parallel Josephson junctions allowing a flux-tunable E_J . When its two junctions are of different areas, the SQUID is asymmetric. The total Josephson energy given in a SQUID, considering its symmetry, is given by [45]

$$E_J(\Phi) = E_{J\Sigma} \cos\left(\frac{\pi\Phi}{\Phi_0}\right) \sqrt{1 + d^2 \tan^2\left(\frac{\pi\Phi}{\Phi_0}\right)}$$
 (2.8)

With E_{J1} and E_{J2} the charging energy of each Josephson junction that forms the loop, Φ the applied flux, and Φ_0 the flux quantum. $E_{J\Sigma} = E_{J1} + E_{J2}$ and $d = (\eta - 1)/(1 + \eta)$ is the junction asymmetry parameter, with $\eta = E_{J1}/E_{J2}$.

2.5 Coupling between the elements

In free space, a single photon traveling through vacuum has a very low probability of interacting with an atom. Even if the two of them happen to interact, their coupling strength is weak, leading to low absorption or emission rates.

To enhance the interaction between atoms and photons, we must confine the photon field, for example, using a cavity. In this chapter, we will explain the different mechanisms to enhance the coupling between the building blocks in our system, giving rise to emergent light-matter interaction phenomena.

2.5.1 Capacitive and inductive coupling

The Hamiltonian between two coupled systems takes the generic form

$$H_T = H_1 + H_2 + H_{int} (2.9)$$

with H_T the total Hamiltonian, $H_{1,2}$ the Hamiltonian of the two systems and H_{int} the interaction Hamiltonian, which couples the two systems.

There are two main coupling mechanisms to make photons and atoms interact: capacitive and inductive couplings. In the capacitive coupling, energy is transferred between two elements through a shared electric field. It occurs when two conductive elements are placed near each other and separated by a dielectric, forming a capacitor. In a parallel plate capacitor, the value of the coupling capacitance is given by:

$$C_c = \varepsilon \frac{A}{d} \tag{2.10}$$

In which C_c is the coupling capacitance, ε the permittivity of the dielectric, A the area of the plates, and d the separation of the plates. The interaction Hamiltonian has the form

$$H_{int} = C_c V_1 V_2 \tag{2.11}$$

with $V_1(V_2)$ the voltage between the two nodes to which the capacitor is connected [36]. In the case of inductive coupling, energy is transferred via a shared magnetic field between two current-carrying conductors, usually coils or loops. When the current in one coil changes with time, it produces a changing magnetic field. Faraday's law relates this changing field to an induced voltage in a second coil given by:

$$V_2 = M \frac{dI_1}{dt} \tag{2.12}$$

In which V_2 is the voltage in the second coil, M is the mutual inductance, which quantifies the strength of the inductive coupling, and I_1 is the current through the first coil. In this case, the interaction Hamiltonian has the form

$$H_{int} = MI_1I_2 \tag{2.13}$$

with $I_1(I_2)$ the current in each one of the loops [36].

In Papers 1 and 2, we implemented capacitive coupling between transmons and resonators, between the charge lines and the transmon, and the resonators to each other (to form the metamaterial). We used inductive coupling to couple the flux line to the SQUIDs and the $\lambda/4$ resonators to the transmission line. In Papers 3 and 4, we used capacitive coupling to couple the transmon to the readout resonator; the readout resonator to the waveguide; and to couple directly the transmons to the transmission line.

2.6 Jaynes-Cummings Hamiltonian

The Jaynes-Cummings model (JCM) describes the interaction between a two-level system (like our transmon qubit) and a single mode of quantized electromagnetic field (a resonator). Under the assumption that the number of excitations is preserved (rotating wave approximation, RWA), the Hamiltonian reads

$$H_{\rm JC} = \hbar \omega_r a^{\dagger} a + \frac{1}{2} \hbar \omega_q \sigma_z + \hbar g \left(a^{\dagger} \sigma_- + a \sigma_+ \right)$$
 (2.14)

In this expression, we combine the two Hamiltonians in 2.7 and 2.3 and add an interacting term. The interaction term, $g\left(a^{\dagger}\sigma_{-}+a\sigma_{+}\right)$ with $\sigma_{-}\left(\sigma_{+}\right)$ the atomic lowering (raising) operators, represents energy exchange between the atom and the field.

In our case, the detuning between the two-level system and the electromagnetic field energies is larger than their coupling, which means that the number of excitations exchanged is suppressed, and the effect of their coupling is that their frequencies get dressed. This is called the dispersive regime, and the Hamiltonian is

$$H_{\rm disp} \approx \hbar \omega_r' a^{\dagger} a + \frac{\hbar \omega_q'}{2} \sigma_z$$
 (2.15)

In which we have substituted what are called, the bare energies ω_r, ω_q with their dressed energies ω_r', ω_q' . The relationship between these two values is

$$\omega_r' = \omega_r + \chi \sigma_z, \omega_q' = \omega_q + \chi \tag{2.16}$$

2.7 Lindblad master equation

We already described the Hamiltonian of a 2-level system interacting with an electromagnetic field. However, the system is not isolated from the environment, so we require a new equation that describes it. This is achieved using the Gorini-Kossakowski-Sudarshan-Lindblad master equation, also known as the Lindblad master equation, which generalizes the Schrödinger equation to open quantum systems. This equation uses the description of the system given by the density operator ρ , in which the system's state could be a statistical mixture of pure states.

$$\rho = \sum_{i,j=1}^{d} \rho_{ij} |\phi_i\rangle \langle \phi_j| = \begin{pmatrix} \rho_{11} & \rho_{12} & \dots & \rho_{1d} \\ \rho_{21} & \rho_{22} & \dots & \rho_{2d} \\ \vdots & \vdots & \ddots & \vdots \\ \rho_{d1} & \rho_{d2} & \dots & \rho_{dd} \end{pmatrix}$$

$$(2.17)$$

In this equation, $|\phi_i\rangle$ and $|\phi_j\rangle$ are the basis states. The diagonal elements of the density matrix, ρ_{ii} , are the populations and they denote the probability of finding the system in the respective basis state. The off-diagonal elements, ρ_{ij} , are known as coherences and quantify the degree of the coherent superposition of the basis states $|\phi_i\rangle$ and $|\phi_i\rangle$.

The Lindblad master equation reads

$$\frac{\mathrm{d}}{\mathrm{d}t}\rho = \mathcal{L}\rho = -i[H, \rho] + \sum_{j} \kappa_{j} \mathcal{D}[L_{j}]\rho \qquad (2.18)$$

in which \mathcal{L} is called the Liouvillian superoperator and the dissipator superoperator \mathcal{D} is defined as

$$\mathcal{D}\left[L_{j}\right]\rho = \mathcal{D}[L_{j}]\rho = L_{j}\rho L_{j}^{\dagger} - \frac{1}{2}\left(L_{j}^{\dagger}L_{j}\rho + \rho L_{j}^{\dagger}L_{j}\right)$$

for any of the dissipation process represented by the operator L_j . For a standard two-level system, we can write the master equation as

$$\frac{d\rho}{dt} = -\frac{i}{\hbar}[H, \rho] + \Gamma_1 \mathcal{D}\left[\sigma_-\right] \rho + \frac{\Gamma_\phi}{2} \mathcal{D}\left[\sigma_z\right] \rho \tag{2.19}$$

Here, Γ_1 is the total energy-relaxation rate defined as $\Gamma_1 = \Gamma_r + \Gamma_n$, containing the radiative part, Γ_r , directly associated with the electromagnetic field and the non-radiative part, $\Gamma_n r$ which is associated with the rest of the environment of the 2-level system. Γ_{ϕ} is the pure dephasing rate.

The energy-relaxation time, also called longitudinal relaxation time, is defined as $T_1 = 1/\Gamma_1$. Caused by sources of transverse noise, energy-relaxation time is the characteristic time of decay of the first excited state to the ground state of the 2-level system.

The pure dephasing time is defined as $T_{\phi} = 1/\Gamma_{\phi}$. This timescale characterizes the randomization of phase relationship in a 2-level system's state without any change to the population of the basis states. Specifically, pure dephasing causes the decay of the off-diagonal terms in the density matrix, and arises from longitudinal noise, does not involve a resonant process, and corresponds to elastic processes, which makes the effect reversible in principle.

The full transverse relaxation time is defined as $T_2 = 1/\Gamma_2 = \Gamma_1/2 + \Gamma_{\phi}$. The parameter T_2 characterizes the overall loss of coherence in a superposition state, arising from the combined effect of the energy relaxation (due to transverse noise) and pure dephasing (due to longitudinal noise).

2.8 Black-box superconducting circuit quantization

When the number of components in a quantum circuit grows, the Jaynes-Cummings model becomes insufficient for describing the system dynamics. To address this challenge, black-box quantization is a semi-classical alternative [36, 46, 47].

The method begins with a linearization of the circuit. All Josephson junctions are treated as linear inductors, allowing the rest of the system to be described in terms of its effective response function, expressed as the admittance seen by the junction. From the admittance, one can directly extract the normal modes of the system, each characterized by a resonance frequency and a dissipation rate. And,

by reintroducing the nonlinearity, the effective Hamiltonian can be obtained. We explain the process in more detail in the following.

When dissipation is weak, the linearized circuit can be accurately approximated as a set of RLC resonators coupled in series. In this case, the total admittance simplifies to

$$Y_j(\omega) \simeq \frac{1}{\sum_m 1/Y_m(\omega)} \tag{2.20}$$

With each element having an admittance

$$Y_m(\omega) = \frac{1}{iL_m\omega} + iC_m\omega + \frac{1}{R_m}$$
 (2.21)

Each RLC resonator represents a normal mode of the circuit with a resonance frequency $\omega_m = 1/\sqrt{L_m C_m}$ and a dissipation rate $\kappa_m = 1/R_m C_m$.

Then, reintroducing the nonlinearity perturbatively, we obtain an effective Hamiltonian that contains both self-Kerr and cross-Kerr terms.

$$H = \sum_{m} \hbar \omega_m a_m^{\dagger} a_m + E_j \left[1 - \cos \varphi_j - \frac{\varphi_j^2}{2} \right]$$
 (2.22)

With $\varphi_j = \sum_m \varphi_{m,j}$ the total phase difference across the josephson junction and the phase difference between the two nodes of each oscillator $\varphi_{m,j} = \varphi_{\text{zpf},m,j} \left(a_m + a_m^{\dagger} \right)$, with $\varphi_{\text{zpf},m,j} = \frac{1}{\phi_0} \sqrt{\frac{\hbar}{2\omega_m C_m}}$. These terms account for the anharmonicity of qubits and the interactions between different modes, making the model well-suited for practical device design and analysis. This approach is used by QuCAT [47], which we used for the designing of the devices in Paper 3 and Paper 4.

Part II Experimental results

Chapter 3

Tailoring the decay rates of artificial atoms and molecules

3.1 Introduction

Quantum systems are not isolated from their environment. On the one hand, coupling to external modes is essential for driving, controlling, and reading out the system. On the other hand, uncontrolled coupling to the bath inevitably leads to dissipation and decoherence, as excitations leak into unmonitored degrees of freedom. In this chapter, we explore two different approaches to tailoring decay rates to the environment.

In the first experiment, we explore the interaction of an artificial molecule comprising two transmon-type elements, directly coupled to a continuum of propagating microwave modes. This work is related to waveguide quantum electrodynamics (WQED). We engineer the coupling of two transmons to two waveguides in a symmetry-selective manner, in such a way that specific transitions appear as bright to one waveguide and dark to the other one [Paper 4]. This scheme enables efficient Raman frequency conversion and the direct generation of spatially-separated Bell states, valuable for distributing quantum entanglement [48–52]. It also opens possibilities for other experiments related to quantum thermodynamics [53] and single-photon microwave photodetection.

In the second experiment, in the context of circuit quantum electrodynamics (CQED) setup [Paper 3], we engineer the dissipation and decay of a transmon coupled to a resonator through the addition of a lumped-element Purcell filter with Josephson junction arrays. Controlling the transmon's decay rate is essential for extending qubit lifetimes, minimizing information loss, and achieving high-fidelity gates. Furthermore, we add an auxiliary, frequency-tunable transmon, directly coupled to the waveguide. This transmon serves as an absolute power sensor to calibrate the input power, from which we can directly determine the Purcell decay.

This chapter is structured as follows. In Section 3.2, we introduce waveguide QED and derive the scattering parameters of an atom directly coupled to the waveguide. In Section 3.3, we describe the experiment reported in Paper 4. Finally, in Section 3.4, we describe the experiment reported in Paper 3.

3.2 Direct coupling of an atom to a waveguide

Waveguide quantum electrodynamics (wQED) studies the interaction between quantum emitters, such as qubits (transmons in our case), and the continuum of modes supported by a one-dimensional (1D) waveguide through which itinerant photons propagate [9, 20–28, 54–56]. This is in contrast to cavity or circuit QED (cQED), which describes how an emitter couples to discrete, confined electromagnetic modes. This distinction leads to fundamentally different phenomena: while cQED emphasizes strong coupling, photon blockade, and dispersive readout through isolated modes, WQED enables controlled dissipation into propagating modes, directional emissions, and direct access to scattering properties of individual photons.

Compared to free-space emission in three-dimensional space, the one-dimensional geometry of WQED further enhances the strength of light–matter interaction, making WQED a powerful platform for probing open quantum systems. In our experiments, we exploit WQED for symmetry-selective dissipation and absolute power calibration.

The Hamiltonian of a two-level system in the presence of a classical drive at frequency ω_L , in the rotating frame of the drive, and within the RWA, is

$$\frac{H}{\hbar} = -\frac{\Delta}{2}\sigma_z + \frac{\Omega}{2}(\sigma_+ + \sigma_-) \tag{3.1}$$

Here, $\Delta = \omega_L - \omega_q$ is the detuning between the drive and the atomic transition, Ω is the Rabi frequency set by the drive amplitude, σ_z is one of the Pauli matrices and σ_+ (σ_-) is raising (lowering) operator. This effective Hamiltonian captures only the coherent part of the dynamics.

3.2.1 Emitted field

In the following measurements, we focus on measuring the radiation field emitted into the waveguide. With the emitter directly coupled to the waveguide, the field amplitude is proportional to the expectation value of the lowering operator.

$$\sigma_{-} = |g\rangle\langle e|, \tag{3.2}$$

which lowers the atom from the excited state, $|e\rangle$, to the ground state, $|g\rangle$. Its expectation value $\langle \sigma_{-} \rangle$ quantifies the atomic coherence and the emitted field. Formally, for any operator O, its expectation value is given by

$$\langle O \rangle = \text{Tr} (O\rho).$$
 (3.3)

Using the Lindblad master equation in 2.18, we write the time evolution of expectation values as:

$$\frac{d}{dt}\langle O\rangle = -\frac{i}{\hbar}\langle [O, H]\rangle + \sum_{j} \gamma_{j} \left(\left\langle L_{j}^{\dagger} O L_{j} \right\rangle - \frac{1}{2} \left\langle \left\{ L_{j}^{\dagger} L_{j}, O \right\} \right\rangle \right) . \tag{3.4}$$

Solving this equation for the lowering operator with the Hamiltonian in Eq. 3.1, and in the steady-state limit, $\left\langle \frac{\mathrm{d}}{\mathrm{d}t}\sigma_i\right\rangle = 0$, yields the expression [57–59]

$$\langle \sigma_{-} \rangle = \frac{\Omega \Gamma_{1} (\Delta - i \Gamma_{2})}{2 \left[\Omega^{2} \Gamma_{2} + \Gamma_{1} \left(\Delta^{2} + \Gamma_{2}^{2} \right) \right]}$$
(3.5)

This equation will be used in the input—output relations to compute the transmission and reflection coefficients of the atom—waveguide system.

3.2.2 Input-output theory and scattering parameters

We treat the waveguide as an environment (bath) that mediates irreversible processes. The emitter is then naturally an open quantum system, and its interaction with the fields in the waveguide is governed by the Linblad master equation and input-output theory. This theory states that the coherent output field, \hat{a}_{out} , is the sum of the incoming coherent field, \hat{a}_{out} , and the field scattered by the two-level system. The scattered field of the two-level system is proportional to the lowering operator σ_- .

In the case, when the emitter is coupled at the end of a waveguide, referred to as the reflection configuration, the input-output theory yields, at steady-state [59]:

$$\alpha_{\text{out}} = \alpha_{\text{in}} - i\sqrt{\Gamma_{\text{r}}} \langle \sigma_{-} \rangle \tag{3.6}$$

Here, $\Gamma_{\rm r}$ is the coupling rate of the emitter to the waveguide and $\langle \hat{a}_{\rm in,out} \rangle = \alpha_{\rm in,out}$ are the steady-state amplitudes of coherent fields. Furthermore, $\alpha_{\rm in} = \frac{\Omega}{\sqrt{2\Gamma_{\rm r}}}$. In another case, when the emitter is coupled in a notch configuration, away from the ends of the waveguide, it scatters the incoming field into two directions. Thus, only half of the radiation is emitted back into the region of incoming field. Therefore, the input-output theory yields [10, 17]:

$$\alpha_{\rm out} = \alpha_{\rm in} - i\sqrt{\Gamma_{\rm r}/2} \langle \sigma_{-} \rangle$$
 (3.7)

Here, $\alpha_{\rm in} = \frac{\Omega}{2\sqrt{\Gamma_{\rm r}}}$.

On solving these equations in conjunction with the Linblad master equation, the reflection coefficient for the reflective configuration is given by

$$r = \frac{\alpha_{\text{out}}}{\alpha_{\text{in}}} = 1 - \frac{i\Gamma_{\text{r}}\Gamma_{1}\left(\Delta - i\Gamma_{2}\right)}{\Omega^{2}\Gamma_{2} + \Gamma_{1}\left(\Delta^{2} + \Gamma_{2}^{2}\right)}$$
(3.8)

Here, $\Gamma_1 = \Gamma_r + \Gamma_{nr}$, $\Gamma_2 = \Gamma_1/2 + \Gamma_{\phi}$, Γ_{nr} is the non-radiative coupling rate to the environment other than the waveguide and Γ_{ϕ} is the pure dephasing rate. In the notch configuration, the transmission coefficient is given by

$$t = 1 - r = 1 - \frac{\Gamma_r}{2\Gamma_2} \frac{1 - i\Delta/\Gamma_2}{(1 + \Delta/\Gamma_2)^2 + \Omega^2/(\Gamma_1\Gamma_2)}$$
(3.9)

These expressions for scattering parameters are used in fitting the experimental data in Paper 3 and Paper 4 to extract the exact values of Γ_r , Γ_2 , Γ_1 and Ω . From Ω , we can extract the input power to the system and the net attenuation in the microwave input line.

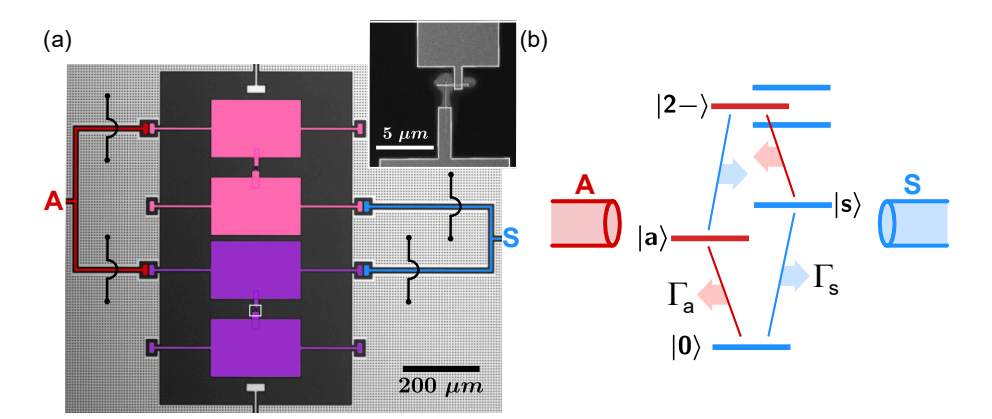


Figure 3.1: (a) False-colored image of the superconducting, artificial molecule. The two transmons are colored in pink and purple, and the two waveguides are in red and blue. Inset: SEM image of the Josephson junction of the purple transmon. (b) Energy levels of the system after the formation of the molecule. Red (blue) color represents the anti-symmetric (symmetric) waveguide and molecule mode.

3.3 Selective coupling of a molecule to two waveguides

In Paper 4, we hybridize two transmon qubits to form an artificial molecule. Because the Hamiltonian of the molecule is invariant under exchange of the two transmons, the resulting collective modes can be classified according to their symmetry under this exchange, represented mathematically by the permutation operator [60]. Specifically, the molecule supports symmetric and antisymmetric eigenmodes, that are also the eigenstates of the permutation operator corresponding to the eigenvalue +1 and -1 respectively. We interface the molecule to two waveguides in a geometry engineered to exploit the symmetry of its eigenmodes to achieve selective coupling.

3.3.1 Experimental implementation

The complete structure of our system includes two nominally identical split-island qubit transmons [colored pink and purple in Fig. 3.1], made from aluminium. Each of these transmons consists of two superconducting islands, which forms the capacitor and a Josephson junction, acting as a non-linear inductor, shunting the two islands. The two transmons are capacitively coupled to each other, with a coupling strength equal to $g/2\pi=296.4$ MHz. In addition, each atom is coupled to a pair of waveguides in a specific geometry such that the modes of the molecule decay into one waveguide or the other depending on the symmetry property of the mode.

3.3.2 Formation of the molecule

When we couple two atoms, their energy levels split, creating what are called the symmetric and antisymmetric states of the molecule. The Hamiltonian of the system is

$$H = \sum_{i=1,2} \left(\omega_i b_i^{\dagger} b_i + \alpha_i b_i^{\dagger} b_i^{\dagger} b_i b_i / 2 \right) + g \left(b_1^{\dagger} b_2 + b_1 b_2^{\dagger} \right)$$
 (3.10)

In this expression, b_i^{\dagger} and b_i are the annihilation and creation operators, ω_i is the transition frequency, α_i is the anharmonicity of atom i; and g is the coupling rate between the two atoms.

When the two atoms have the same transition energy, the resonant states $|01\rangle$ and $|10\rangle$ split by 2g into two hybridized states. The resulting states are $|a\rangle = (|01\rangle - |10\rangle)/\sqrt{2}$ and $|s\rangle = (|01\rangle + |10\rangle)/\sqrt{2}$, which are antisymmetric and symmetric states respectively. The eigenstates and eigenvalues resulting from the diagonalization of the previous Hamiltonian up to the second excited state and their measured values for Paper 4 are given in Table 3.1.

Eigenstate	Bare states composition	Eigenvalue	Value/ 2π
$ 0\rangle$	$ 0,0\rangle$	0	0 GHz
$ a\rangle$	$ 1,0\rangle - 0,1\rangle$	$\omega - g$	$5.6981~\mathrm{GHz}$
$ s\rangle$	$ 1,0\rangle + 0,1\rangle$	$\omega + g$	$6.2909~\mathrm{GHz}$

Table 3.1: Eigentates and eigenvalues of the diagonalized Hamiltonian.

3.3.3 Selective coupling to the waveguide

Since the artificial molecule is much smaller than the wavelength of the excitation frequencies ($\omega_a/2\pi = 5.7$ GHz and $\omega_s/2\pi = 6.3$ GHz), the incoming microwave signals from the waveguide are spatially uniform across the device. In other words, the molecule behaves as a lumped element, and a near-resonant drive does not acquire any appreciable phase difference between the two transmons.

The symmetric and antisymmetric eigenstates correspond to distinct voltage distributions across the circuit nodes (each isolated superconducting island). In the symmetric state, voltage in the inner nodes of the molecule oscillate in phase while being π out of phase with the outer nodes. In the antisymmetric state, voltage in the same side nodes oscillate in phase. This relative phase differences for the modes within the molecule are crucial. In the manner we engineer the coupling geometry, we ensure that each waveguide is sensitive to a particular mode. For waveguide S, the in-phase voltages of the symmetric state add constructively. In contrast, out-of-phase nodes that couple to waveguide A interfere destructively, leaving the symmetric mode to only decay into the waveguide S. Analogously, for waveguide A, the in-phase voltages of the antisymmetric state directly couple and interfere constructively. The two nodes coupled to waveguide S are out-of-phase in voltage and interfere destructively. This phenomenon is illustrated in Fig. 3.2, in which the phase relations of the voltages in the superconducting islands (nodes) make the selective coupling mechanism visually clear.

We characterize the symmetry-selective coupling by measuring the reflection coefficient with a VNA, |r|, for each waveguide for different input powers [Fig.3.3]. The reflection coefficient, given by Eq.3.8, depends on the rate at which each molecular

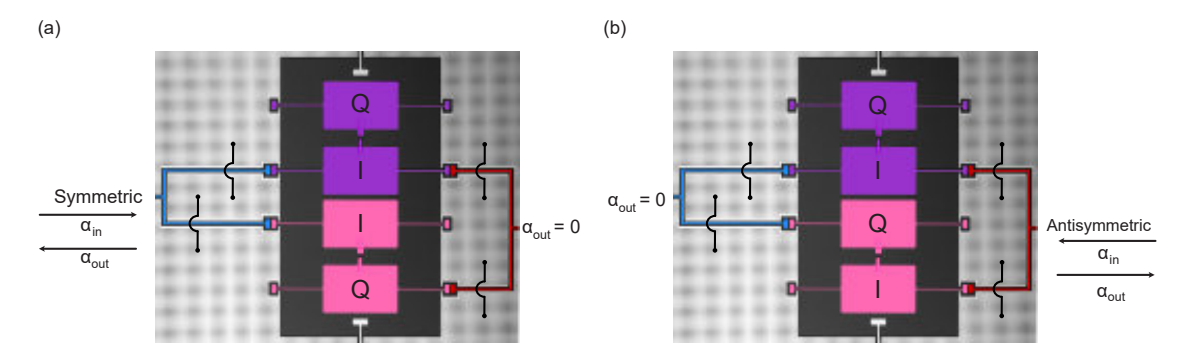


Figure 3.2: Schematic of the symmetric and antisymmetric coupling to the waveguide. (a),(b) A signal is sent through the symmetric (antisymmetric) waveguide, no signal is detected in the antisymmetric (symmetric) waveguide because of destructive interference.

mode couples to its corresponding waveguide, $\Gamma_{a,s}$, as well as its residual decay into other channels, including the cross coupling to the opposite waveguide, $\Gamma_{a,s}^0$.

When driving through waveguide A at an input power that corresponds to what is called the magic power [Fig.3.3(a) in red], there is a complete suppression of the reflection coefficient at the antisymmetric mode frequency $\omega_a/2\pi$. This behavior is a signature that the transition $|0\rangle \leftrightarrow |a\rangle$ is overcoupled to waveguide A and $\Gamma_a > \Gamma_a^0$. At the symmetric mode frequency $\omega_s/2\pi$, we instead observe only a shallow dip in reflection, indicating that the symmetric mode is very undercoupled to waveguide A.

The situation is reversed when probing through waveguide S [Fig.3.3(a) in blue]: the symmetric transition exhibits full suppression, while the antisymmetric transition shows only a weak dip. This complementary behavior directly demonstrates the symmetry-selective coupling of our device.

By analyzing the power dependence of the reflection coefficient, we further confirm our interpretation [Fig.3.3(b)]. At low drive power, the reflection coefficient traces nearly a full circle in the IQ plane, characteristic of coherent scattering from a two-level system. As the power is increased, the circle contracts to a single point, consistent with saturation of the transition and a crossover to incoherent scattering [10].

Fitting Eq.3.8 to the data, we find that the symmetric mode couples more strongly than the antisymmetric one, largely due to the stronger capacitance between the inner nodes connected to waveguide S. In addition, the residual loss channels $\Gamma^0_{a,s}$ are dominated by leakage into the opposite-symmetry waveguide. Overall, the antisymmetric state emits predominantly into waveguide A with a selectivity ratio $\Gamma_a/\Gamma^0_a=35$, while the symmetric state emits predominantly into waveguide S with $\Gamma_s/\Gamma^0_s=47$. We attribute the difference in selectivity between the two waveguides to parasitic capacitance, which causes leakage into the unintended waveguide node. This effect is more noticeable for the antisymmetric mode.

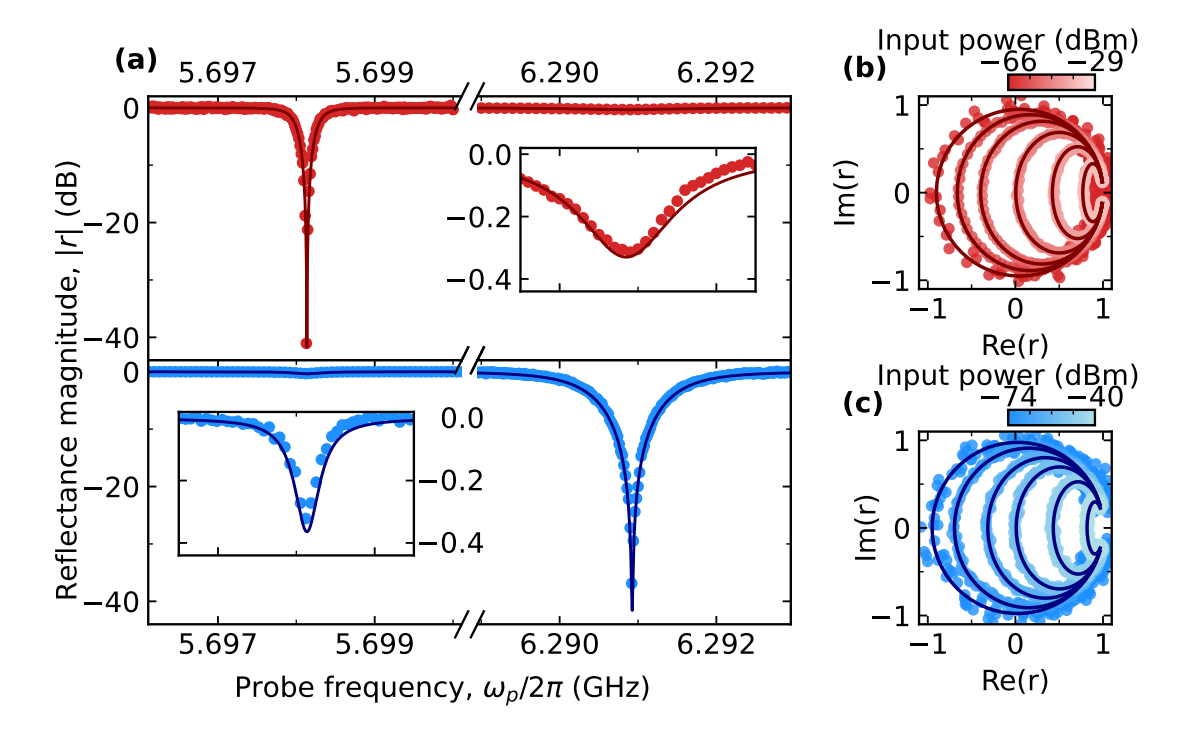


Figure 3.3: Measurement of the reflection coefficient, r, for the two waveguides. (a) Reflection coefficient's magnitude for both waveguides at the magic power for the symmetric and antisymmetric modes. The waveguide A is colored red, the waveguide S is colored blue. (b) IQ plane at different input powers. Solid curves are fits based on the model described in the text.

3.4 Purcell filter and characterization of the Purcell decay

When we couple a qubit to a far detuned resonator for state readout, the system operates in the dispersive regime. In this regime, the energies of the qubit and the resonator get shifted by their interaction, but there is no excitation exchange between the two subsystems. However, the qubit can still decay into the waveguide through the resonator. This occurs because the resonator eigenstate acquires a small qubit component due to the interaction. It is precisely this qubit component of the resonator wavefunction that leaks into the waveguide, leading to an effective qubit decay channel. This effect is called Purcell decay, and cannot be avoided even in the dispersive regime. Moreover, there is a fundamental tradeoff: faster qubit readout requires stronger coupling to the resonator, but this simultaneously enhances Purcell decay, approximately given by $\kappa(\frac{g}{\Delta})^2$, with κ the coupling of the resonator to the feedline, g the coupling between the qubit and the resonator and Δ the frequency detuning between them [5, 36].

In order to reduce the Purcell decay, a standard approach is to include what is called a Purcell filter. This filter, reduces the indirect coupling of the qubit to the waveguide without reducing its coupling to the resonator. Therefore, we can achieve fast readout without qubit decay [61–64].

Several approaches have been taken to implement these filters [15, 65–83]. How-

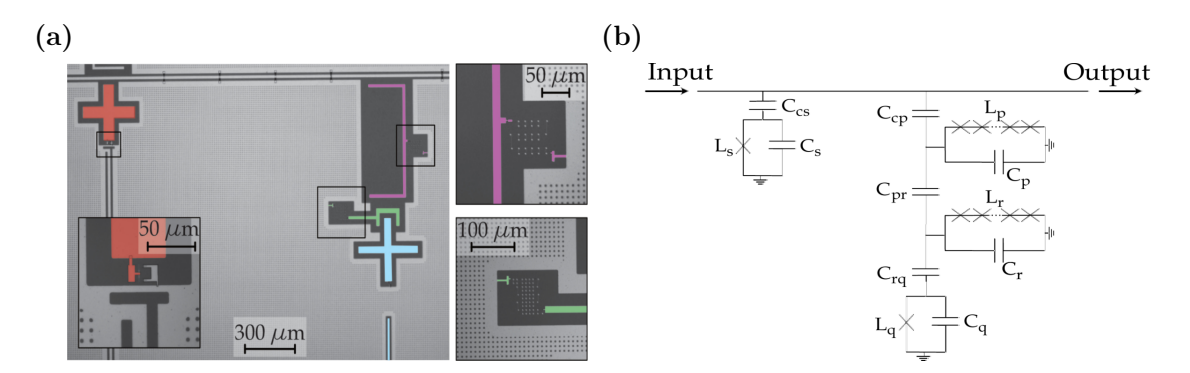


Figure 3.4: Purcell filter device overview. (a) False-colored optical micrograph of the device. In red: The power sensor. In purple: The Purcell filter. In green: The readout resonator. In blue: The transmon qubit. Insets show close-ups of the non-linear inductors. (b) Simplified circuit of the system.

ever, all of these approaches have the main limitation of using distributed resonators, which have a large footprint, close to 4 mm per resonator.

In this work, we propose compact, lumped-element resonators fabricated with Josephson junction arrays as readout resonators with dedicated Purcell filters. The nonlinearity of the resonators is effectively suppressed by distributing it across multiple junctions in each array, enabling measurements in the linear regime [42]. To complement this design, we integrate a frequency-tunable transmon directly coupled to the waveguide, functioning as a power sensor. Once the attenuation has been calibrated in the line, we can estimate the Purcell decay rate of the qubit by measuring the rate of Rabi oscillations when driving the qubit via the readout line [77]. The experimental device is designed to enable fast dispersive readout while keeping the system very compact, similar to the dimensions of the transmon. In addition, the design is extensible for multiplexed readout.

3.4.1 Experimental implementation

Our superconducting device, in Fig. 3.4(a), was designed with an optimizer built on the lumped-element circuit of Fig. 3.4(b), implemented in QuCAT [47]. The optimizer extracted resonance frequencies, decay rates, and couplings, and evaluated them with a cost function that minimized the Purcell decay rate, Γ_p , while keeping the resonator decay to the waveguide, κ , and the dispersive coupling, 2χ , as close as possible to each other to obtain the highest SNR between the ground and the excited state [84] and in the MHz range. Within these constraints, the optimizer was free to adjust the frequency of each circuit element, while operating within the dispersive regime, and the design of the Purcell filter.

The core of the device consists of two capacitively coupled lumped-element resonators fabricated from arrays of Josephson junctions [Fig. 3.4(a)(b)]. Each resonator is composed of a shunt capacitor to ground and an inductive element formed by a series array of Josephson junctions. One of these resonators is coupled to the feedline and functions as a Purcell filter, while the second is directly coupled to the qubit and acts as the readout resonator.

The Purcell filter is constructed from an array of 30 identical Josephson junctions, yielding a total inductance of $L_p = 5.8$ nH. The readout resonator, built with 55 junctions, has a larger inductance of $L_r = 7.79$ nH. We use junction arrays rather than single junctions to suppress the resonators' intrinsic nonlinearities. The nonlinearity scales with $1/N_{JJ}^2$, with N_{JJ} the number of Josephson junctions in the array. The suppression factors reach approximately 900 for the filter and 3025 for the readout resonator. This ensures that both resonators behave linearly over the operating range, avoiding unwanted Kerr effects that could degrade readout fidelity.

In addition, to suppress parasitic couplings to the transmission line, the Purcell filter was realized with an elongated structure that increases the separation between the transmon and readout resonator to the feedline. The readout resonator itself is compact and strongly coupled to the transmon, $g=403.3\,\mathrm{MHz}$. To further enhance compactness and inter-element coupling, the ground plane between them was intentionally removed.

A standard X-mon style transmon qubit is capacitively coupled to the readout resonator, with a single Josephson junction serving as its nonlinear inductor. To facilitate direct microwave control and excitation of the qubit, we include a dedicated charge line in the design. The charge line is designed such that its induced relaxation time exceeds the intrinsic relaxation time of the qubit, $T_1 = 120 \,\mu$ s.

In addition to this protected readout architecture, the device incorporates a second, frequency-tunable X-mon transmon directly coupled to the same transmission line. This auxiliary qubit serves as a sensor for probing the attenuation at the line. This qubit includes a symmetric superconducting quantum interference device (SQUID). Frequency tunability is achieved by injecting magnetic flux into the SQUID loop via a flux line and an external coil.

3.4.2 Characterization of the device

We use a VNA to measure the transmission parameter, S_{21} , through the feedline [Fig. 3.5(a)(b)]. The resonant modes of the system appear as dips in the transmission spectrum, from which we determine the resonance frequencies of the two hybridized resonators, $\omega_1/2\pi = 7.31$ GHz and $\omega_2/2\pi = 7.89$ GHz, and the sensor qubit at its sweet spot, $\omega_s/2\pi = 6.114$ GHz. We use the second hybridized mode as our readout mode, and we restrict our further analysis to the interaction between this mode and the qubit.

We study the nonlinearity of the readout mode by measuring the transmission S_{21} for different pulse amplitudes [Fig. 3.6]. We extract the number of injected photons in the resonator by the readout pulse with a Stark-shift measurement of the qubit frequency [85]. In this measurement, we track the qubit frequency as the resonator gets populated. The average photon number in the resonator is given by $\langle a^{\dagger}a \rangle = \Delta \omega_q/2\chi$, where $\Delta \omega_q$ is the shift in the qubit frequency and 2χ is the dispersive shift, measured directly with standard spectroscopy of the resonator at qubit states $|g\rangle$ and $|e\rangle$.

We compare our measurements with the critical photon number, n_{crit} , which gives an approximate bound for the average intracavity photon population above

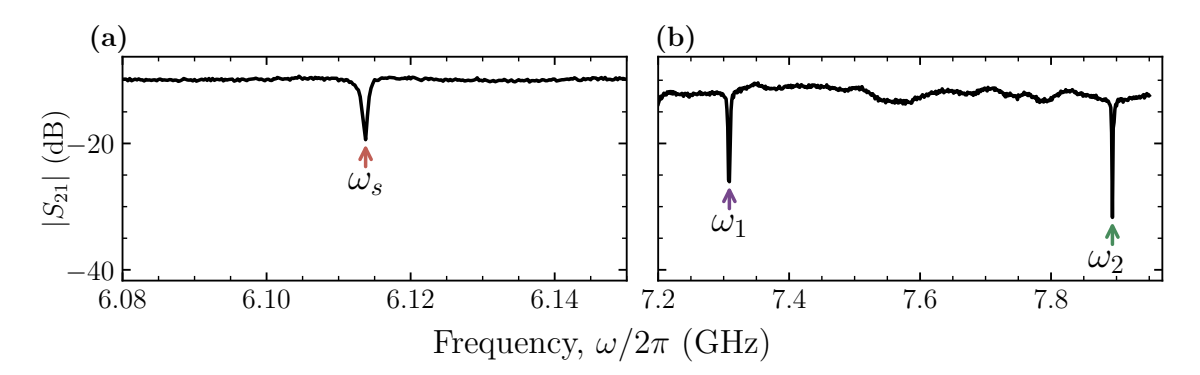


Figure 3.5: Transmission $|S_{21}|$ through the line depending on the frequency. (a) $|S_{21}|$ around the sensor frequency, $\omega_s/2\pi = 6.114$ GHz. (b) $|S_{21}|$ around the Purcell and resonator hybridized frequencies, $\omega_1/2\pi = 7.31$ GHz and $\omega_2/2\pi = 7.89$ GHz, respectively.

which the dispersive approximation breaks down. This value is obtained from $n_{\rm crit} = \Delta^2/(2g)^2 = 27$, where g is the qubit–resonator coupling strength, given by $g = \sqrt{\Delta\chi(1+\Delta/\alpha)} = 403.3$ MHz, and $\alpha/2\pi = -240$ MHz is the qubit anharmonicity directly measured [5].

With increasing input power [Fig. 3.6], the mode frequency of resonator shifts driven by two different mechanisms: the breakdown of the low-power dispersive regime and the self-Kerr nonlinearity. For low photon numbers, $n \ll n_{\rm crit}$, the response is linear and the resonator mode frequency remains unaltered. With the addition of only a few photons, however, small frequency shifts on the order of a few kilohertz emerge. Near the critical photon number, these shifts become larger due to the contribution of both mechanisms, the nonlinearity and the failure of the dispersive approximation. Above $n_{\rm crit}$, nonlinearity dominates, leading to a bistable behavior that is the hallmark of a Duffing oscillator [86].

We model this behavior with the standard Duffing oscillator response, which is valid in the low-photon-number regime,

$$S_{21}(\omega, n) = 1 - \frac{\kappa}{\gamma_T/2 - i(\omega - \omega_r + Kn)}$$
(3.11)

with κ the radiative loss, $\gamma_T = \kappa + \gamma$ the total decay rate, including the non-radiative loss, γ , ω_r the resonance frequency of the resonator, K is the self-Kerr nonlinearity, and n is the intracavity photon number.

In practice, the measured transmission spectrum is also affected by environmental factors, such as impedance mismatches and finite cable delays, which alter the ideal resonance lineshape [87]. We account for these extrinsic effects by introducing an overall amplitude factor, A, a phase offset, α , and a frequency-dependent time delay, τ . The transmission expression becomes

$$\tilde{S}_{21}(\omega, n) = Ae^{i\alpha}e^{-i\omega\tau}S_{21} \tag{3.12}$$

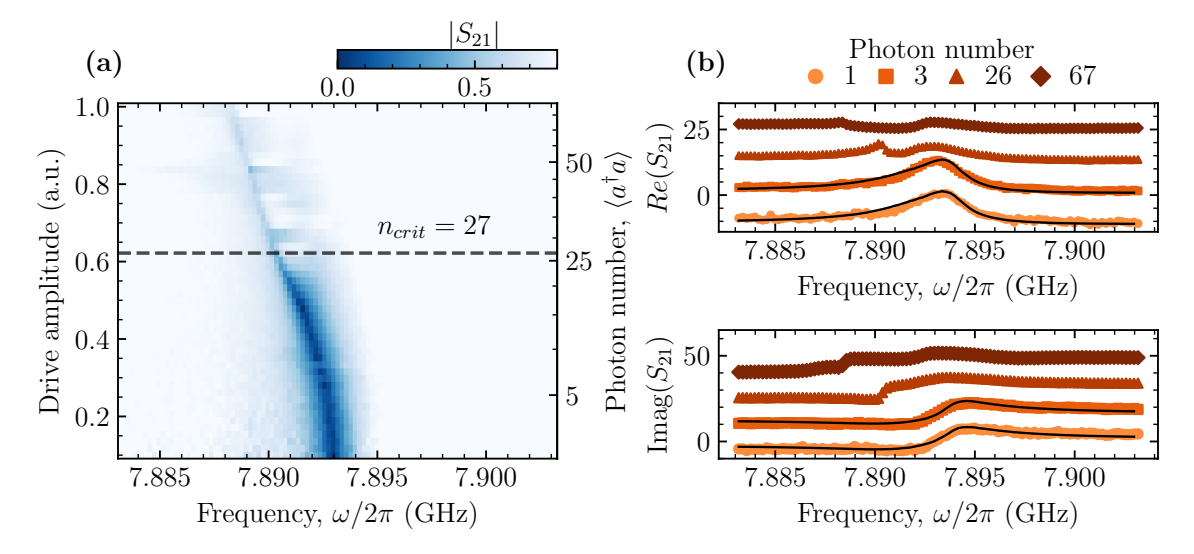


Figure 3.6: Characterization of the nonlinearity of the readout mode. (a) $|S_{21}|$ depending on the readout pulse amplitude and frequency. (b) $|S_{21}|$ depending on the frequency for selected photon numbers, compared to the fitted model (In black). (c) IQ plane of (b).

By fitting this model to the experimental data, we extract $\kappa/2\pi=2.1\,\mathrm{MHz}$, $\gamma/2\pi=1.8\,\mathrm{MHz}$, and $K/2\pi=-39.35\,\mathrm{kHz}$. We compare the fitted value to the nonlinearity expected from a simple two-hybridized model $K=-E_c/(2N_{JJ}^2)=-58.342\,\mathrm{kHz}$, with E_c the charge energy extracted from microwave simulations of the capacitance matrix, and to the one inherited from the qubit, $K=(\frac{g}{\Lambda})^4\alpha=-21.2\,\mathrm{kHz}$.

3.4.3 Single-shot measurements

We characterize the qubit readout by probing the response of the readout mode when the qubit is prepared in the states $|g\rangle$, $|e\rangle$, and $|f\rangle$ [Fig. 3.7(a)(b)]. We prepare the qubit in the first excited state, $|e\rangle$, with a π -pulse at the qubit frequency $\omega_q = 3.73$ GHz. The second excited state, $|f\rangle$, is populated by applying two sequencial π -pulses to drive the $|g\rangle \to |e\rangle$ and $|e\rangle \to |f\rangle$, respectively. The second state is at $\omega_q^{|f\rangle} = 3.49$ GHz. After preparing the desired qubit state, we monitor the corresponding shift in the resonator response to extract the state-dependent dispersive signatures. From this measurement, we extract the dispersive shift, $2\chi/2\pi = 4.36$ MHz, and we identify $\omega_r/2\pi = 7.889$ GHz as the frequency that provides the maximum separation in both the real and imaginary quadratures for the states the three states [Fig. 3.7(a)(b), dashed line].

We compare the dispersive shift to the coupling rate of the resonator to the transmission line, and obtain a ratio $\kappa/2\chi=0.492$. This ratio indicates that the readout operates in a regime where the dispersive shift is sufficiently large to resolve the qubit states, while still comparable to the linewidth of the resonator. This balance is crucial: if $2\chi \ll \kappa$, the qubit states would not be distinguishable in the resonator response, whereas if $2\chi \gg \kappa$, the critical photon number decreases, limiting the number of photons used to readout the state, and the distinguishability does not

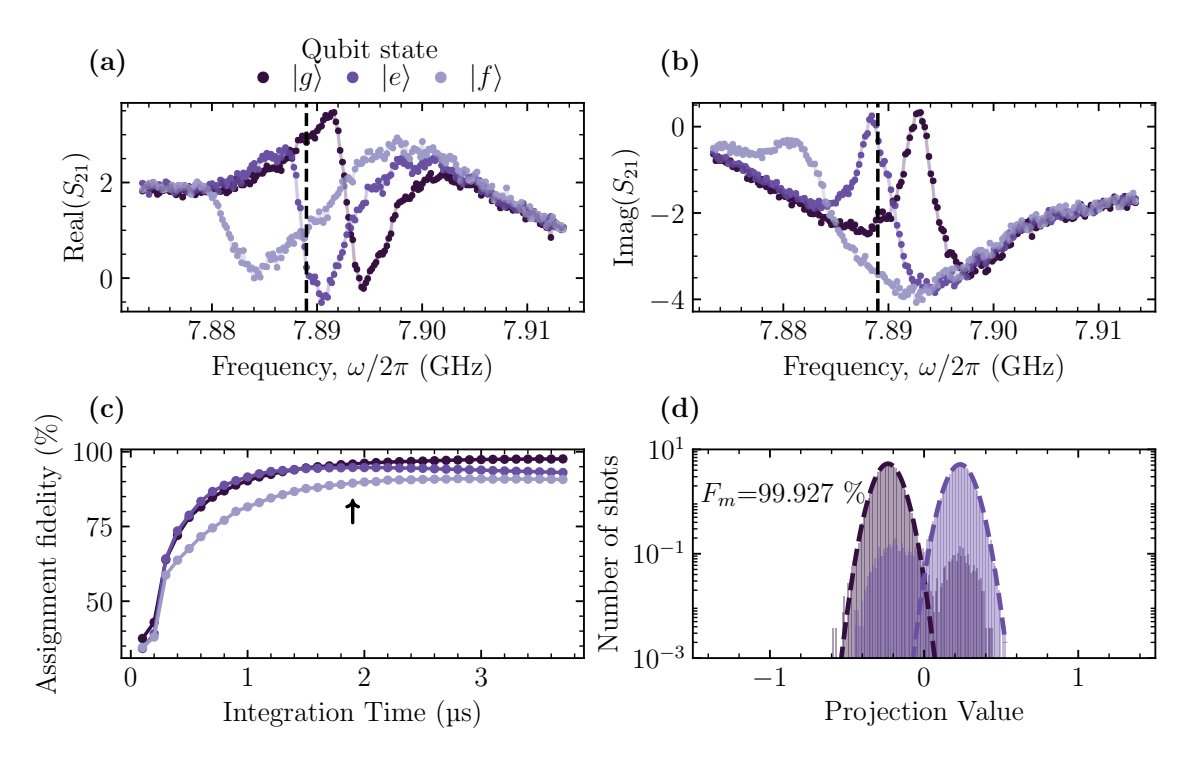


Figure 3.7: **Single-shot characterization.** (a) Real part of the single-tone measurement of the readout resonator when the qubit is in $|g\rangle$, $|e\rangle$, and $|f\rangle$. Dashed line: Measurement frequency for maximum differentiation between the three states. (b) Imaginary part of (a). (c) Assignment fidelity depending on the integration time for the three prepared states. Dashed line: Maximum state fidelity for $|e\rangle$, and $|f\rangle$ states. (d) Projection for the states $|g\rangle$ and $|e\rangle$ and maximum measurement fidelity.

improve further, so the SNR gets reduced.

With the optimal operating frequency of the resonator established, we proceed to characterize the single-shot performance of the readout. In quantum information processing, single-shot readout is essential, since averaging over many repetitions is incompatible with real-time feedback and error correction. For quantum error correction (QEC) protocols in particular, the readout must be both high-fidelity, to ensure reliable syndrome extraction, and fast, to avoid qubit decay or measurement-induced transitions during the pulse. Failure to meet either condition compromises the accuracy of the measurement and the effectiveness of the QEC cycle [88, 89].

The assignment fidelity is the probability of measuring the qubit in the state that it was prepared, $P(i|i\rangle)$. To validate the readout of our system, we record single-shot time traces of the resonator with a square template-matching procedure with an integration window of 100 ns and record times up to $3.8\,\mu s$. Then, we average these integrated traces over a total integration time, t_{int} , and investigate the dependence of the readout assignment fidelity on this time [Fig. 3.7(c)].

From the acquired single-shot histograms, we extract to the signal-to-noise ratio from the single-shot histograms as

$$SNR^{2} \equiv \left| \frac{\mu_{g} - \mu_{e}}{(\sigma_{g} + \sigma_{e})/2} \right|^{2}$$
(3.13)

	Prepared	Prepared	Prepared
	g angle	e angle	$ f\rangle$
Assigned $ g\rangle$	95.90%	3.60%	6.03%
Assigned $ e\rangle$	1.96%	94.73%	4.47%
Assigned $ f\rangle$	2.14%	1.67%	89.50%

Table 3.2: Tri-state assignment fidelity table with an integration time $t_{int} = 1.9 \,\mu\text{s}$.

[75] with $\mu_{g,e}$ are the mean of the Gaussian distributions in states $|g\rangle$ and $|e\rangle$ and $\sigma_{g,e}$ their corresponding standard deviations.

As expected, the assignment fidelity improves with increasing integration time because of the corresponding enhancement of the signal-to-noise ratio (SNR). However, beyond a certain threshold, the fidelities of the $|e\rangle$ and $|f\rangle$ states begin to degrade. This reduction arises from state mixing during the readout pulse. In contrast, the assignment fidelity of the ground state $|g\rangle$ continues to increase monotonically with integration time up to 2.39%. We expect this value to keep increasing until saturation at the value of the thermal population of the qubit 1.8%. This value is extracted independently from the difference in amplitude of the rabi oscillations between $|e\rangle$ and $|f\rangle$ states with and without a π -pulse between $|g\rangle$ and $|e\rangle$ states [90].

We identify $t_{int} = 1.9 \,\mu\text{s}$, as the integration time for which the assignment fidelity for the excited state is maximal. At this integration time, we evaluate the confusion matrix in Table 3.2. The diagonal elements of the fidelity matrix represent cases where the qubit is correctly identified in the state in which it was prepared, and thus should ideally approach 100%. Experimentally, we obtain assignment fidelities of 95.9%, 94.73%, and 89.50% for the qubit prepared in the $|g\rangle$, $|e\rangle$, and $|f\rangle$ states, respectively.

We extract the measurement-induced dephasing in the steady state, $\beta_{\rm m}$, of our qubit using the expression [5],

$$\beta_{\rm m} = \frac{2\kappa \chi^2 \bar{n} \tau_m}{\chi^2 + (\kappa/2)^2} \tag{3.14}$$

with \bar{n} the number of photons injected in the resonator, which we obtain independently from a Stark-shift measurement, $\bar{n} = 17.5$, and τ_m is the integration time of our signal. Then, we can extract the number of added photons by our amplification chain as [5]

$$n_{noise} = \frac{\beta_{\rm m}}{SNR^2} - \frac{1}{2} \tag{3.15}$$

 $n_{noise}=17$ photons, which is well above the quantum limit [84, 91]. The measured infidelity in the prepared $|g\rangle$ state is mainly attributed to residual thermal excitations and charge noise that unintentionally populate the $|e\rangle$ and $|f\rangle$ states. These effects can be mitigated by applying a pre-selection readout pulse to confirm initialization in the ground state before the main experimental sequence [92]. Additionally, cross-assignment errors in the $|e\rangle$ and $|f\rangle$ states can arise from excessive readout amplitude, which distorts the measurement histograms. Reducing the readout drive power and shortening the readout pulse duration would help minimize these effects.

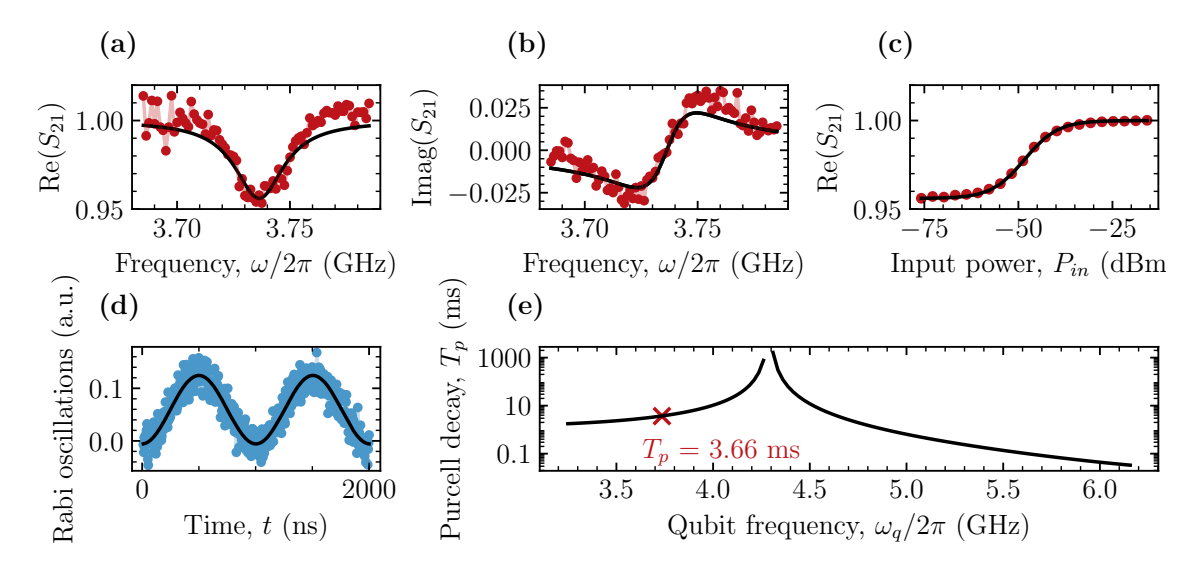


Figure 3.8: **Purcell decay calibration.** (a), (b) Real and imaginary parts of the transmission of the sensor at the frequency of the qubit, $\omega_s/2\pi = 3.735$ GHz for an input power $P_{in} = -78.8$ dBm. In black: The fitting by the model. (c) Real part of the transmission at $\omega_s/2\pi = 3.735$ GHz for different input powers. In black: The fitting by the model. (d) Rabi oscillations when the qubit is excited from the transmission line for an input power $P_{in} = -16$ dBm. (e) Measured Purcell decay (Red cross) compared to the obtained decay from the model.

The added noise by our gain chain limits the achievable signal-to-noise ratio (SNR) during readout, and we require a higher readout amplitude. As a result, even when the qubit is perfectly prepared, we cannot achieve a 100% discrimination fidelity, due to a higher measurement-induced dephasing. The single-shot measurement histograms for the $|g\rangle$ and $|e\rangle$ states [Fig. 3.7(d)] establish an upper bound on the achievable measurement fidelity under the present experimental configuration. The finite overlap between the two distributions results in a maximum fidelity of $F_{\rm m}=99.927\%$ [93], which represents the intrinsic discrimination limit imposed by the current setup. By improving the amplitication chain to four added noise photons, we would approach the same $F_{\rm m}$ with a shorter integration time $t_{\rm int}\approx 447$ ns. In addition, in this case, we expect the assignment fidelities to approach $F_{\rm m}$, as measurement-induced transitions would be reduced.

3.4.4 Measurement of Purcell decay

Having validated the qubit readout fidelity, we next calibrate the Purcell-limited relaxation time to assess the performance of the Purcell filter. For this characterization, we employ the transmon directly coupled to the feedline waveguide, which serves as a calibrated power sensor [Fig. 3.8]. The transmon's transmission response is strongly dependent on the input power and can be accurately modeled using input—output theory for a two-level system coupled directly to an open waveguide, as it was already derived in Section 3.2 [10, 17, 59, 94, 95]. The corresponding transmission coefficient, derived from Eq. 3.2.2 but including the effect of the environment, is expressed as

$$S_{21} = be^{i\theta}e^{-i\omega\rho} \left(1 - \frac{\Gamma_1}{2\Gamma_2} \frac{1 - i\frac{\Delta}{\Gamma_2}}{1 + \left(\frac{\Delta}{\Gamma_2}\right)^2 + \frac{\Omega^2}{\Gamma_1\Gamma_2}} \right), \tag{3.16}$$

where b, θ , and ρ account for port mismatch and cable delay effects. The parameters Γ_1 and Γ_2 denote, respectively, the radiative coupling rate and the total decoherence rate, with $\Gamma_2 = \Gamma_1/2 + \Gamma_{\phi}$, where Γ_{ϕ} represents the pure dephasing rate. The detuning is defined as $\Delta = \omega - \omega_s$, with ω_s the resonance (plasma) frequency of the sensor, and Ω_s the Rabi rate in the sensor, which depends directly on the input power as

$$\Omega_s = 2\sqrt{\frac{A\kappa P_{\rm in}}{\hbar\omega_s}},\tag{3.17}$$

where A is the total input line attenuation, κ the coupling efficiency, and $P_{\rm in}$ the input power at room temperature.

To perform the calibration, we apply a magnetic flux via an external coil to tune the frequency of the transmon sensor to match the qubit frequency at $\omega_s/2\pi = 3.73$ GHz, a point detuned by more than 2 GHz from the sweet spot. At this frequency, we measure the transmission through the feedline at very low input power $(P_{\rm in} = -78.8 \text{ dBm})$ [Fig. 3.8(a–b)]. A reference background for the transmission is obtained by detuning the sensor far from the qubit frequency, allowing subtraction of the microwave components' noise.

At this low-power limit, we assume $\Omega_s \approx 0$ MHz and extract the decay and dephasing rates $\Gamma_1/2\pi = 1.16$ MHz and $\Gamma_\phi/2\pi = 12.6$ MHz, respectively. We attribute the large dephasing rate to the sensor being operated far from its flux sweet spot, where the device is more susceptible to flux noise [96]. A small systematic deviation in the extracted S_{21} parameter is attributed to the qubit frequency $(\omega_q/2\pi)$ being located near the edge of the amplifier bandwidth (nominally 4–12 GHz), which slightly degrades the measurement precision.

To further characterize the system, we measure the power dependence of S_{21} at the sensor frequency [Fig. 3.8(c)]. This dataset is fitted using the theoretical model above, with the input line attenuation A as the only free parameter. All other parameters are fixed to the values obtained from the low-power measurement. From the fit, we extract A = -84.56 dB, which is in good agreement with the nominal line attenuation of -80 dB, excluding the attenuation from the cables.

The Purcell-limited relaxation rate, $\Gamma_P(\omega_q)$, can then be determined directly from the measured Rabi rate Ω_q when the qubit is driven through the feedline at its resonance frequency [77]:

$$\Gamma_P(\omega_q) = \frac{\Omega_q^2}{4} \frac{\hbar \omega_q}{A P_{\rm in}}.$$
(3.18)

Here, Ω_q denotes the Rabi oscillation frequency of the qubit [Fig. 3.8(d)]. The input power is directly calibrated using the attenuation factor A, which was determined from the sensor measurements. This expression provides a quantitative link between the qubit's measured drive strength and its radiative decay into the feedline, enabling an experimental verification of the Purcell filter's suppression performance. For an

input power of $P_{\rm in}=-16$ dBm and a Rabi frequency of $\Omega_q=990$ kHz, we obtain a Purcell-limited lifetime of $T_p=3.66$ ms. This value is significantly higher than the predicted lifetime in the absence of the Purcell filter, $T_p=1/(\kappa g^2/\Delta^2)=0.4\,\mu{\rm s}$, and also exceeds the measured relaxation time of $T_1=120~\mu{\rm s}$. Furthermore, the extracted result is consistent with the expected value obtained from quantum circuit analysis [Fig. 3.8(e)].

3.4.5 Conclusion

In this experiment, we study an individual Purcell filter-resonator structure formed by lumped-element resonators with Josephson junction arrays. The nonlinearity of the resonators is scaled by the number of Josephson junctions in the array.

We obtain tri-state assignment fidelities over 90% even with a noisy amplification chain and characterize the Purcell performance by directly extracting the Purcell decay using an auxiliary transmon as power sensor. We extract a Purcell-limited decay time exceeding 3.5 ms, substantially longer than the measured qubit lifetime $T_1 = 120 \ \mu \text{s}$, confirming the effective suppression of radiative loss through the Purcell filter.

This design is compact and scalable, which makes it suitable for dense multi-qubit architectures. This work provides a practical route toward next-generation quantum processors and contributes to the realization of fault-tolerant superconducting quantum computing platforms.

Chapter 4

Qubits coupled to metamaterials based on Josephson-junction arrays

4.1 Introduction

In this chapter, we go one step forward in structuring the environment and study the effect of an atom coupled to a 1D structured waveguide, a metamaterial, with a spectral density that features bands and bandgaps. When an emitter is coupled to the band edge of a metamaterial, its emission properties are strongly affected, giving rise to an atom-photon bound state. Atom-photon bound states have been studied both theoretically [97–109] and experimentally in different setups [12, 18, 32, 110–123]. These studies have focused on characterizing the exponential localization of the photonic component of the atom-photon bound state using their interaction with the metamaterial edges or making the atom-photon bound states interact with each other [18, 31, 40, 120, 124]. Time-dependent studies have shown non-Markovian dynamics, population exchanges, and photonic hoppings through the metamaterials [19, 30, 120]. However, a detailed study of the dynamics in the formation and melting of the atom-photon bound states and the mode decomposition of these states had remained unexamined. In Paper 1, we addressed these questions.

This chapter is divided as follows: In Section 4.2, we introduce the metamaterial of Paper 1, its experimental implementation, and its dispersion relation. In Section 4.3, we introduce the formation of the atom-photon bound state (APBS). In Section 4.4, we characterize our device. In Section 4.5, we study the dynamics involved in the formation and the melting of the atom-photon bound state and identify the threshold between adiabatic and non-adiabatic regimes. In Section 4.6, we directly measure the photonic part of the atom-photon bound state, which turns into delocalized modes that we collect at the output of our metamaterial after quenching the state. In Section 4.7, we use this technique to characterize the APBS when changing its hybridization state with the metamaterial and the dynamics when forming it.

34 4.2. Metamaterials

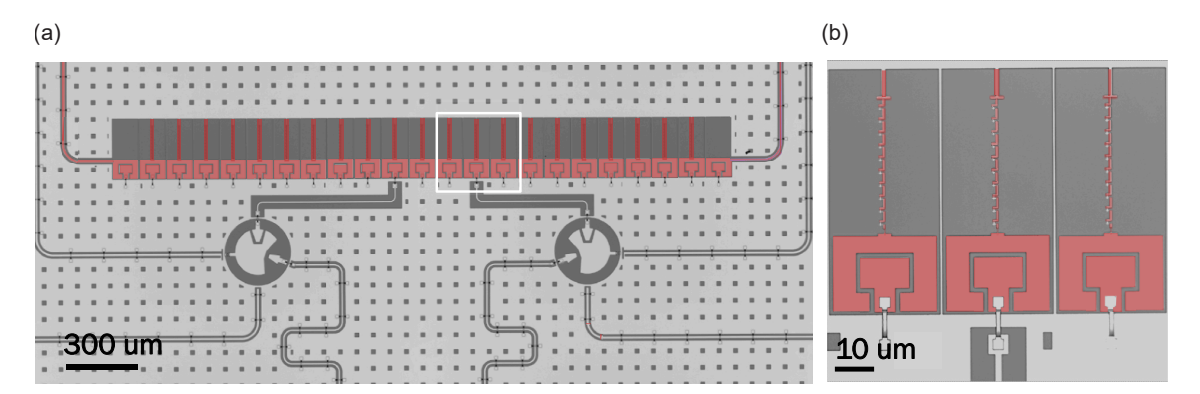


Figure 4.1: Metamaterial false-colored optical micrograph. (a) Metamaterial device showing the resonator arrays and emitters. (b) Three resonators composed of the JJs arrays and superconducing islands forming capacitors with the ground plane.

4.2 Metamaterials

We define a metamaterial as an artificially structured material engineered to have electromagnetic properties not typically found in natural materials. A key feature of these systems is their engineered dispersion relation that features both bands, in which propagation is allowed, and bandgaps, in which propagation is suppressed. This band structure makes them analogous to photonic crystals and electronic band structures well known in solid-state physics, in which spatial periodicity, either in material composition or structural geometry, gives rise to allowed and forbidden energy regions. Within the framework of wQED, the periodicity introduced into the waveguide by the metamaterial modifies the photonic environment experienced by the quantum emitters, enabling exotic light-matter interactions.

4.2.1 Experimental implementation

Standard experimental implementations of metamaterials include the use of distributed and lumped resonators [18, 19, 40, 120, 125]. In our case, we use an array of capacitively coupled high-impedance lumped resonators, represented in Fig. 4.1. Each resonator is formed by an array of Josephson junctions serving as an inductor and a superconducting island capacitively coupled to the ground plane as a capacitor. All resonators in the array are designed to be nominally identical. This homogeneity is crucial because it ensures uniform electromagnetic properties through the structure, so that the resonance frequency of the structures is the same. We include air-bridges to couple the 9th and 11th resonators (counted from left) to two emitters realized with transmons (Section 4.3 for more details). We add air-bridges to the ground plane for the rest of the resonators to maintain electromagnetic homogeneity. In addition, capacitive couplings between resonators are controlled by their physical design and distance and give rise to nearest-neighbor couplings.

The characterization of the metamaterial's resonators is obtained from microwave simulations of their capacitance matrix and room-temperature resistance measurements of their JJ arrays (in its non-superconducting state). From this, we extract

the inductance of the array, $L_r \approx 11.7$ nH, and the capacitance, $C_r \approx 75$ fF. In addition, the coupling capacitance between the resonators is $C_i \approx 5.3$ fF.

From these simulations, the frequency of the resonator is $\omega_r/2\pi = 1/(2\pi\sqrt{L_rC_r}) \approx 5.34 \ GHz$. The relatively large inductance of these resonators leads to enhanced impedance, $Z_r = 1/(\omega_r C_r) \approx 390 \ \Omega$. Based on the equation for the capacitive coupling between two resonators

$$g/\hbar = \frac{1}{2}C_c\omega_1\omega_2\sqrt{Z_1Z_2} \tag{4.1}$$

with C_c the coupling capacitor, $\omega_{1,2}$ is the resonance frequency of each resonator, C_c the coupling capacitor and $Z_{1,2}$ the impedance of each resonator. The large impedance in our resonators has two direct consequences: the coupling between the resonators is enhanced proportional to Z_r and the coupling to an atom is enhanced proportionally to $\sqrt{Z_r}$. From the simulated values and the previous expression, we obtain a resonator-resonator coupling, $J/2\pi \approx 190 \text{ MHz}$.

The nonlinearity scales as $U' = U/N_r/N_{JJ}^2$, with N_r the number of resonators and N_{JJ} the number of junctions. Therefore, we assume that the system's anharmonicity is sufficiently small to be negligible at low powers, allowing us to approximate it as a linear system in the following sections.

4.2.2 Tight-binding model Hamiltonian

The tight-binding model describes our system with nearest-neighbor interactions, which lead to the formation of a photonic band structure. The Hamiltonian of the metamaterial is

$$H = \sum_{n=1}^{N} \omega_r a_n^{\dagger} a_n + J \sum_{n=1}^{N-1} \left(a_n^{\dagger} a_{n+1} + a_{n+1}^{\dagger} a_n \right)$$
 (4.2)

in which N is the total number of resonators, a_n^{\dagger} and a_n are the creation and annihilation operators of the n-th resonator, ω_r is the bare resonance frequency of each identical resonator, and J is the coupling strength between nearest neighbors. This Hamiltonian is analogous to that of electrons in a periodic potential, and leads to a cosine-shaped dispersion relation for the photonic modes

$$\omega_n = \omega_r + 2J\cos\left(\frac{\pi n}{N+1}\right) \quad n = 1, \dots, N,$$
 (4.3)

In this expression, ω_n is the frequency of the n-th mode of the system. The resulting photonic band structure features a transmission band with a bandwidth of 4J and centered around the bare cavity frequency ω_r , and two bandgaps at higher and lower energies. This tight-binding framework provides a simple yet powerful way to understand the dynamics of the metamaterial and predict its spectral properties.

36 4.2. Metamaterials

4.2.3 Scattering parameters

The dispersion relation provides insight into the mode distribution within the transmission band. However, to model the transmission coefficient, we employ input-output theory. Specifically, we use the Green's function [19] to describe the system's response to excitation at the input port, given by

$$a_{\text{out}}(\omega) = a_{\text{in}}(\omega) - i\sqrt{\kappa_n} \sum_{m} G_{nm}(\omega) F_m(\omega)$$
 (4.4)

In this equation, ω is the probe frequency, $a_{\text{out}}(\omega)$ is the output field for each frequency, $a_{\text{in}}(\omega)$ is the input field, κ_n is the coupling rate of site n to the output port in the waveguide, G_{nm} is the Green's function from site m to n and $F_m(\omega)$ is the drive field at site m. The Green function is

$$G(\omega) = (\omega I - H_{\text{eff}})^{-1} \tag{4.5}$$

The non-Hermitian Hamiltonian of the system is

$$H_{\text{eff}} = \begin{pmatrix} \omega_r - i\left(\frac{\gamma}{2} + \kappa\right) & J & J' & 0 & s & 0 & 0 \\ J & \omega_r - i\frac{\gamma}{2} & J & J' & \ddots & \vdots & \vdots & \vdots \\ J' & J & \omega_r - i\frac{\gamma}{2} & J & \ddots & 0 & 0 \\ 0 & J' & J & \ddots & \ddots & J' & 0 \\ \vdots & \ddots & \ddots & \ddots & \ddots & \omega_r - i\frac{\gamma}{2} & J & J' \\ 0 & \cdots & 0 & J' & J & \omega_r - i\frac{\gamma}{2} & J \\ 0 & 0 & 0 & 0 & J' & J & \omega_r - i\left(\frac{\gamma}{2} + \kappa\right) \end{pmatrix}$$

$$(4.6)$$

In this Hamiltonian, we include a parasitic next-to-nearest neighbor coupling, $J'/2\pi$, to improve the fittings. γ is the non-radiative decay of each resonator, which we assume to be 0, and κ is the coupling of the first and last resonators to the input and output ports. We assume the coupling to the ports is the same on both sides, and the non-radiative decay rates are the same for all resonators.

Combining equations 4.4, 4.5, and 4.6 and assuming that the excitation only occurs at the first resonator, the transmission coefficient, S_{21} , is

$$S_{21}(\omega) = -i\kappa G_{21,1}(\omega) \tag{4.7}$$

4.2.4 Transmission band

We study the transmission band of our metamaterial by measuring the scattering parameter, S_{21} , through the metamaterial input and output ports with a VNA. For this measurement, we keep the two transmons almost 2 GHz detuned from the band edge, so they do not participate in the measurement.

We extract from the transmission band's bandwidth the resonator-resonator coupling, $J/2\pi = 220MHz$, and from the center frequency of the band the resonator

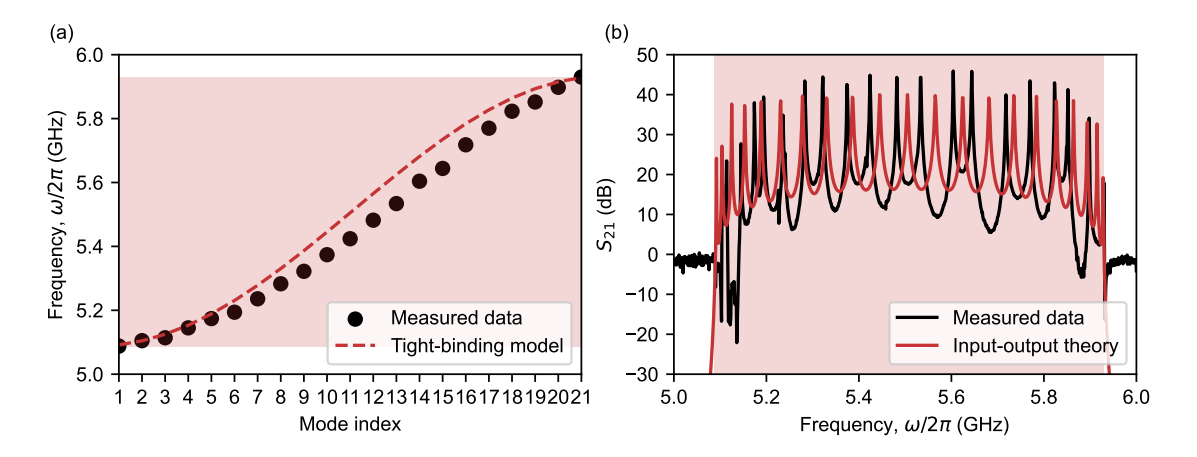


Figure 4.2: Dispersion relation and transmission of the metamaterial using tight-binding model. (a) Dispersion relation of the measured data (circles) compared to that obtained from tight-binding model (dashed curve). (b) Transmission through the resonator array from both experiment (black curve) and theory (red curve).

frequency, $\omega_r/2\pi = 5.5075$ GHz. These values are in good agreement with the ones extracted from the microwave simulations.

We model the system with the tight-binding model using these values and with the best-fit next-nearest-neighbor coupling rates [Fig. 4.2]. The best-fit transmission curve show that the mode distribution in our measured transmission curve does not perfectly match that predicted from the tight-binding model. We attribute this deviation to the disorder that exists in our system, mainly arising from the Josephson junctions in the resonators. Variations in the fabrication of these junctions lead to shifts in the resonator frequencies, causing deviations from the ideal conditions assumed in the tight-binding model. To account for this, we adopt a different modelling approach, which we describe in Section 4.3.3

4.3 Atom-photon bound states

Coupling an emitter to a metamaterial leads to the formation of an atom-photon bound state. Close to the band-edge of the metamaterial, the group velocity of photons is significantly reduced, enhancing the light-matter interaction. As a result, the photonic field becomes spatially localized around the emitter, leading to the emergence of a bound state between the emitter and the photonic mode.

The atom-photon bound state is a hybridized state between an atom and a photon. In this state, the atomic excitation of the emitter becomes entangled with the photonic modes of the metamaterial. Unlike extended photonic states that propagate through the metamaterial, the bound state's photonic part exhibits an exponentially decaying spatial profile centered on the site to which the emitter is coupled. This exponential localization is controlled by the frequency detuning of the atom from the band edge, and can mediate long-distance interactions with tunable range between emitters [18, 19, 40, 97, 101, 120].

This state is mathematically expressed as

$$|\Psi_{\text{APBS}}\rangle = c_E \sigma_+ |g,0\rangle + \sum_{i=1}^N c_i a_i^{\dagger} |g,0\rangle$$
 (4.8)

In this expression, c_E (c_i) is the amplitude coefficient of the emitter-like (ith photon-like) state, $|g,0\rangle$ is the ground state of the composite system, σ^+ is the ladder operator, and a_i^{\dagger} is the creation operator [101]. The probability coefficients depend on the detuning between the emitter and the transmission band of the metamaterial.

4.3.1 Experimental implementation

In our case, we use two frequency-tunable transmon qubits as emitters. These transmons are formed by a circular-like shape superconducting island as a capacitor and an asymmetric SQUID as a non-linear inductor. The two emitters are independently, fully controllable through both their charge (XY-control) and flux lines (Z-control). They are coupled to the metamaterial at sites 10 and 13, respectively, and we include two readout resonators to measure their states.

In Fig. 4.3, we show the complete false-colored optical micrograph of our device, including its external connections and its installation in the dilution refrigerator (More details on the experimental setup in Section 7). We have kept the left transmon uncolored because it is kept at its lowest frequency and does not take part in the following experiments.

Because of the asymmetry in the SQUID, the frequency tunability of the transmons shows two flux-insensitive operating points (sweet spots). One of them is more than 2 GHz detuned from the transmission band of the metamaterial and the other one is deep inside the metamaterial transmission band. This large frequency tunability allows good control of the atom-photon bound state's exponential localization, and transitions between a point far away from the transmission band – in which the emitter acts as a standard transmon and the atom-photon bound state has not been formed – and at the band edge, in which the atom-photon bound state is completely formed.

4.3.2 Tight-binding model Hamiltonian

The Hamiltonian of the complete system using the tight-binding model for the metamaterial is,

$$H = \sum_{n=1}^{N} \omega_r a_n^{\dagger} a_n + J \sum_{n=1}^{N-1} \left(a_n^{\dagger} a_{n+1} + a_{n+1}^{\dagger} a_n \right) + \omega_q b^{\dagger} b + \frac{\alpha}{2} b^{\dagger} b^{\dagger} b b + g \left(a_{13}^{\dagger} b + b^{\dagger} a_{13} \right)$$
(4.9)

In this equation, we use the same terms as in Equation 4.2, adding the terms corresponding to the emitter. b^{\dagger} (b) is the creation (annihilation) operator of the transmon, ω_q is its bare frequency, and α is its anharmonicity. The tight-binding model is defined in real space; therefore, since the transmon is physically coupled

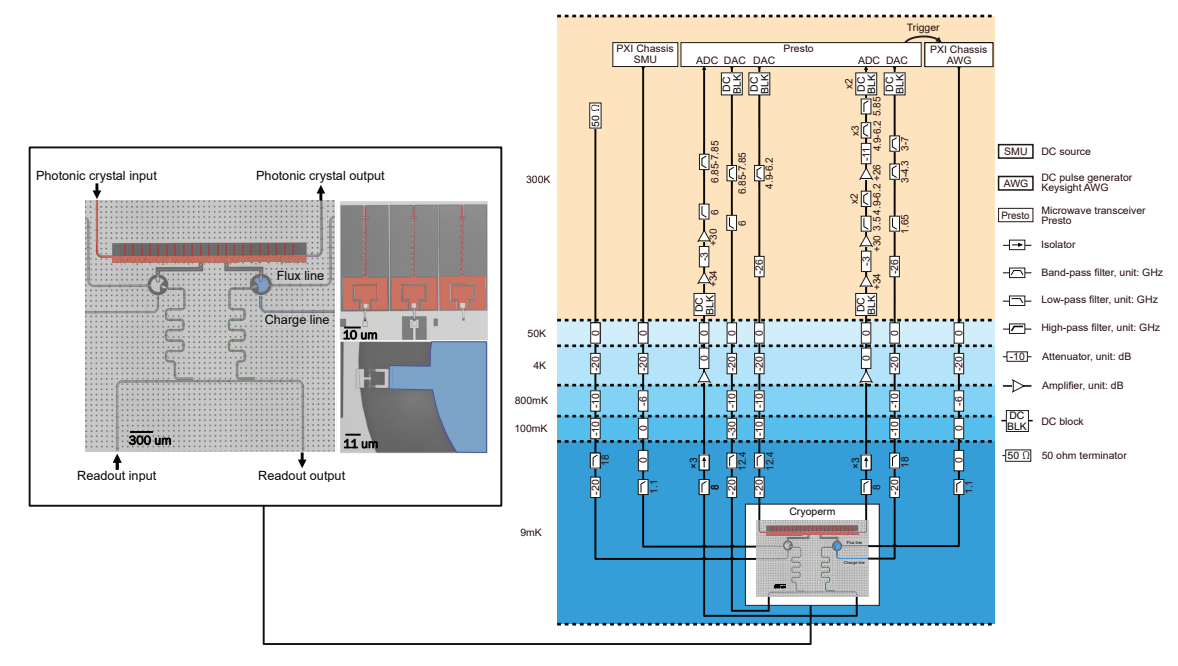


Figure 4.3: False-colored optical micrograph of the device and its experimental setup. The metamaterial device is colored in red, the used transmon is colored in blue and the readout resonator in green. The charge line is also colored in blue and the flux line in orange. The external connections include a Presto from Intermodulation Products to down-convert and up-convert the signals, drive the transmon and capture the emission from the metamaterial. The AWG controls the frequency of the transmon to form and melt the atom-photon bound state.

only to the 13th resonator (from left), the coupling strength, g, is exclusively between this resonator and the transmon.

4.3.3 Effective model Hamiltonian

We consider the effect of the metamaterial modes' disorder in our system, already reported in Section 4.2.3, by using an effective model derived from the measured modes in the metamaterial. The Hamiltonian becomes

$$H = \sum_{n=1}^{N} \omega_n a_n^{\dagger} a_n + \omega_q b^{\dagger} b + \frac{\alpha}{2} b^{\dagger} b^{\dagger} b b + \sum_{n=1}^{N} g_n \left(a_n^{\dagger} b + b^{\dagger} a_n \right)$$
(4.10)

Using directly the dressed modes of the system is effectively a diagonalization of the tight-binding Hamiltonian, with a change of basis from the spatial basis to the energy basis of the system. The effect on the coupling of the transmon to the system is that it is coupled to all the modes with which it interacts.

4.4 Characterization of the device

When the atom-photon bound state forms, the bare frequency of the transmon is affected by its interaction with the metamaterial, and the resulting frequency is shifted. In addition, the frequencies of the metamaterial's modes are also affected

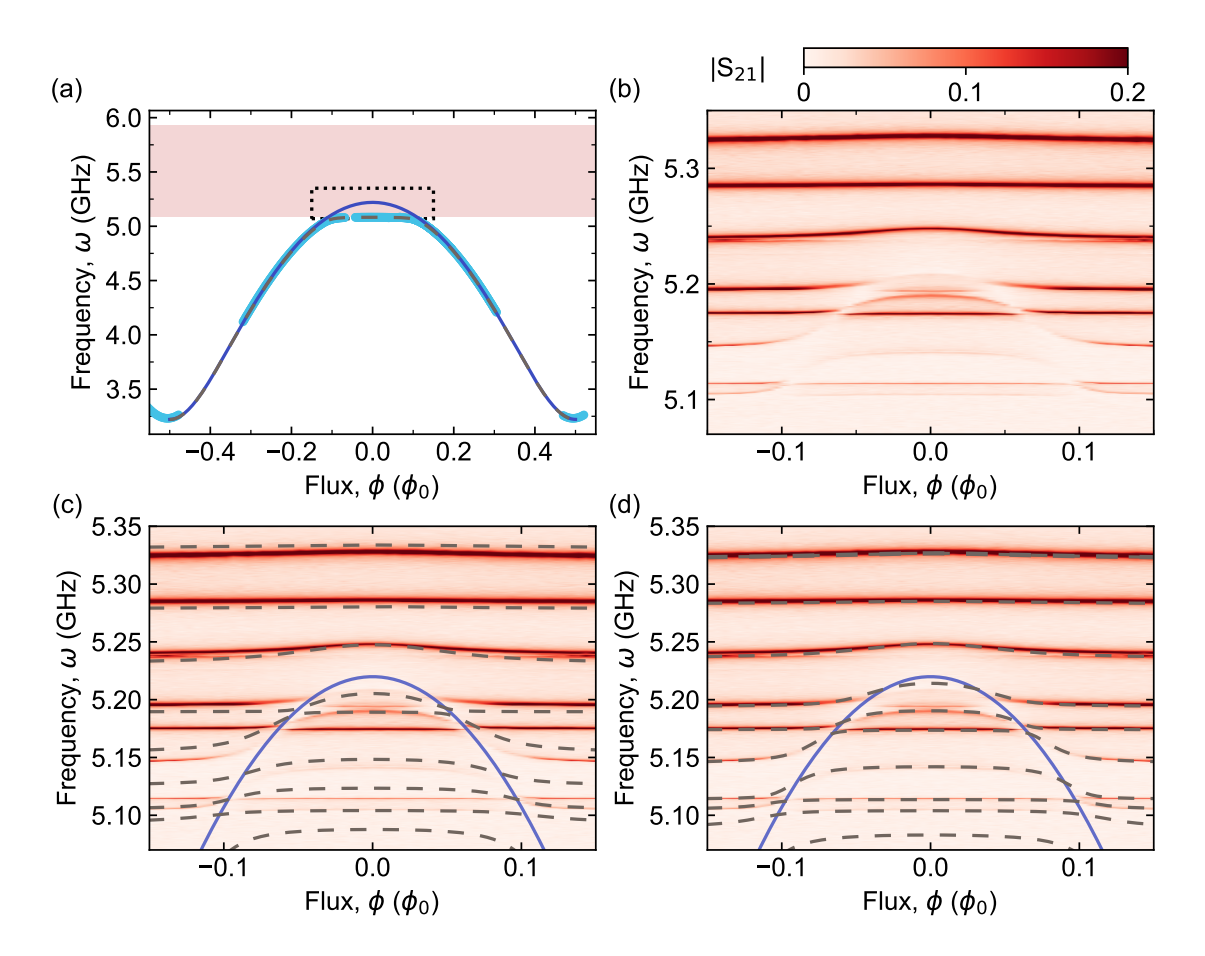


Figure 4.4: Characterization of the formation of the atom-photon bound state. (a) Frequency response of the emitter obtained from two-tone spectroscopy. Measured: Light blue, bare: Dark blue. Dashed: Extracted from the Hamiltonian in Eq. 4.9. (b) Measurement of the transmission and the metamaterial modes deviation when the qubit frequency is swept. (c) Comparison between measurement and prediction from the tight-binding model (dashed lines). (d) Comparison between measurement and the effective model (dashed line).

by the creation of the atom-photon bound state. We measure this interaction both from the transmon and from the transmission band side [in Fig. 4.4].

We measure the effect on the emitter [in Fig. 4.4 (a)] with a two-tone spectroscopy measurement determining the transmon frequency while tuning the magnetic flux in its asymmetric SQUID. Far detuned from the transmission band, the emitter's measured frequency follows the expected trend for an isolated transmon given by Eq. 2.8. However, when the emitter frequency approaches the transmission band, its frequency deviates from this expected frequency response and is prevented from entering the transmission band. This is a clear feature of the creation of the atomphoton bound state.

To measure the effect in the metamaterial modes, we measure the transmission band while changing the emitter frequency. The interaction with the emitter [Fig. 4.4 (b)] affects the 9 lowest-energy modes, which shift in frequency and exhibit avoided crossings.

We model the creation of the atom-photon bound state using both models [Fig. 4.4 (a),(c-d)]. In the tight-binding model [Fig. 4.4 (c)], the positions of the metamaterial modes, especially those near the band-edge, are not accurately reproduced. This discrepancy is expected, as these modes are more sensitive to disorder within the metamaterial. Nevertheless, the model successfully captures the frequency of the atom-photon bound state. In contrast, the effective model [Fig. 4.4 (d)] reproduces both the atom-photon bound state and the metamaterial modes frequencies. For this reason, we use the effective model to analyze subsequent measurements.

4.5 Dynamics in the formation and melting of an atom-photon bound state

In our case, we form the atom-photon bound state by exciting the qubit far detuned from the transmission band and bringing it close to the band-edge. We call the reverse process melting.

To study the dynamics in the formation and melting of an atom-photon bound state, we vary the flux Φ to transition between the flux value Φ_i at which the emitter's frequency is far away from the transmission band, and the flux value Φ_f , at which emitter's frequency is close to the band edge. Importantly, we vary the flux at different rates. When the emitter is at Φ_i , it does not interact with the metamaterial and acts as a standard transmon. However, when the emitter is at Φ_f , it interacts with the metamaterial, and their excitation is completely hybridized, forming the atom-photon bound state.

We measure how the excitation of the transmon is affected when we form and melt the atom-photon bound state between $\omega_q(\Phi_{\rm i}) \approx 4.2$ GHz and $\omega_q(\Phi_{\rm f}) \approx 5.2$ GHz, applying a trapezoidal flux pulse with a varying rise time, $\tau_{\rm r}$, ranging from 10 to 200 ns, a hold time, $\tau_{\rm hold}$, between 0 and 400 ns, and a fall time, $\tau_{\rm f}$, from 10 to 200 ns. The hold time controls the duration for which the atom-photon bound state exists, while the rise and fall times control the dynamics of formation and melting, respectively.

The complete pulse sequence [Fig. 4.5(a)] includes a π -pulse which excites the transmon, the trapezoidal flux pulse described above, and a square pulse to the readout resonator to measure the state of the transmon according to the dispersive shift. The time between the end of the π -pulse and the readout pulse is kept constant to remove the effect of decay in the system. In addition, we normalize the total recovered population, $P_{|1\rangle}$, to a reference taken without the flux pulse.

The recovered population depends on both the hold time and the rise and fall times, and exhibits two main trends [Fig. 4.5(b)]. The first one is that the averaged $P_{|1\rangle}$ is reduced for shorter τ_r and τ_f . The second one is that there are oscillations in the population depending on the hold time.

We study the frequency of these oscillations by doing a Fourier transform (FFT) of the data [Fig. 4.5(c)]. Thereby, we identify that the frequency components of the oscillations correspond to the distance between the modes in our system. This result shows that when the rise and fall times of our system are below 200 ns, the



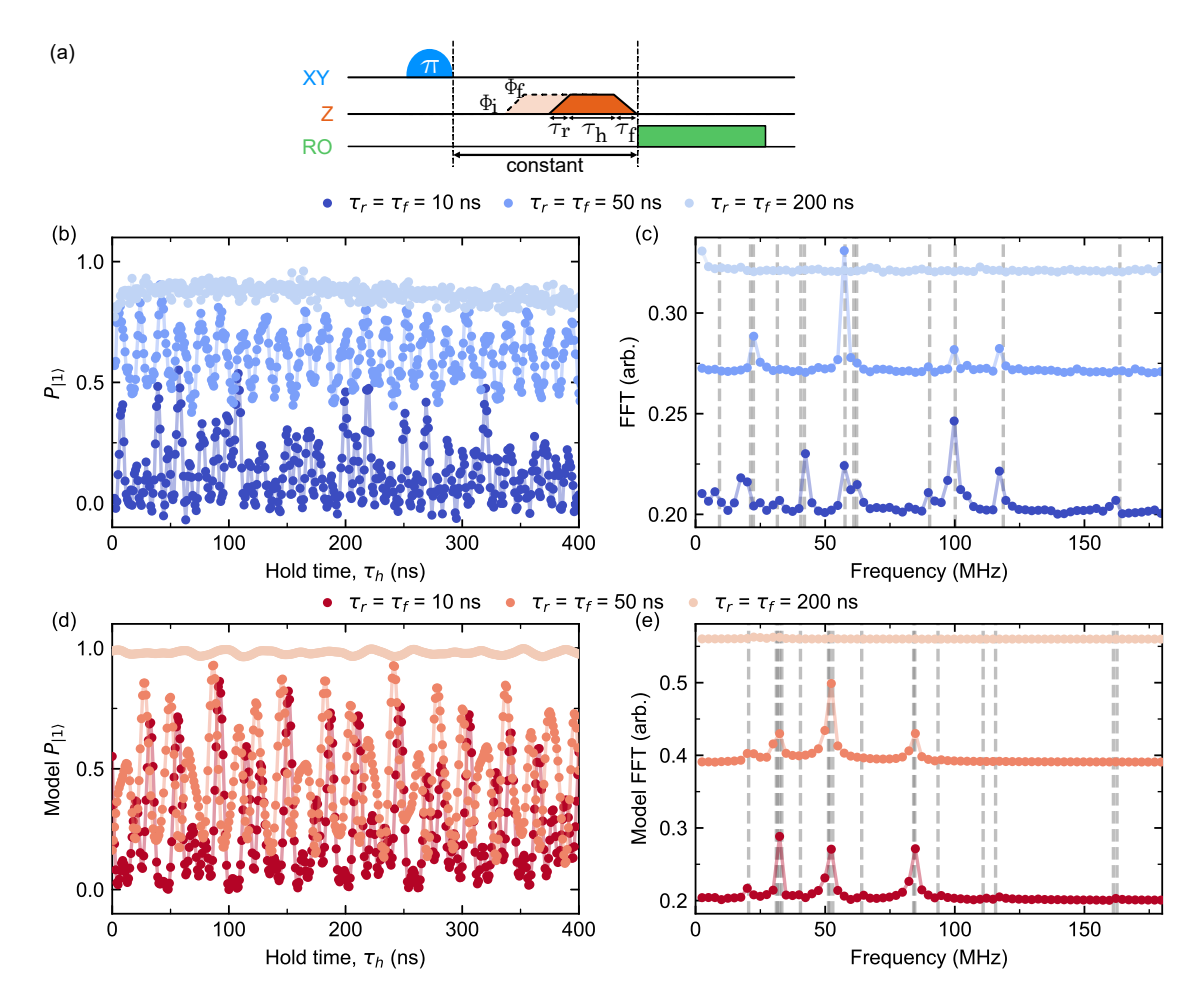


Figure 4.5: **Dynamics in the formation of an atom-photon bound state.** (a) Pulse sequence. (b) Measured recovered population in the excited mode. (c) FFT of (b). (d) Model result of (b). (c) FFT of (d).

excitation in our transmon is transmitted to the metamaterial modes when forming the atom-photon bound state. This is known as the non-adiabatic regime [126–129]. In this regime, there is a non-zero probability of population transitions from one mode to the other, by Landau-Zenner tunneling. On the other hand, when the rise and fall times of our system are 200 ns or higher, the excitation is almost fully recovered, and no visible oscillations appear, proving that our system is in the adiabatic regime.

We study the Landau-Zenner dynamics in our system using the single-mode equation

$$P_{\rm LZ} = \exp(-2\pi\Gamma) \tag{4.11}$$

which gives the probability that a quantum system will not make a transition between two energy levels when they are swept through an avoided crossing. In this expression, $\Gamma = g^2 \Delta t/\Delta E$ with ΔE the energy difference between emitter's initial and final states, Δt the $\tau_{\rm r}$, and g the coupling between the emitter and each metamaterial mode. From this equation, we expect to cross over between two regimes at times between 200-300 ns, which is compatible with our observations.

We model these results with our effective model solving the Shrödinger equation [Fig. 4.5(d-e)], which reproduces the qualitative behavior of our measurements but with some quantitative differences. The difference in the recovered population for $\tau_r = \tau_f = 200$ ns between our model and our experimental results arises likely from a two-level system (TLS) near the metamaterial that reduces the recovered population to $P_{|1\rangle} = 0.9$. There are also differences in the FFT peak positions and intensities, which we attribute to an incorrect model parameter estimate from the spectroscopy data or the uncorrected flux-line transfer function causing distortions in the flux pulses.

4.6 Emission of an atom-photon bound state

After identifying the threshold for the adiabatic and non-adiabatic regimes, we are able to transfer the population from our atom-photon bound state to the metamaterial by quenching the atom-photon bound state with a flux pulse with a $\tau_f = 10$ ns.

For this measurement, we adiabatically form the atom-photon bound state with a $\tau_r = 300$ ns and melt it with a $\tau_f = 10$ ns. From the results we obtained before, we expect this fast quench to transmit all the population of our atom-photon bound state to the metamaterial modes. This population is then transmitted through the metamaterial and collected at the metamaterial output.

Our measurement uses a 1 GHz bandwidth centered at 5 GHz. We choose this center frequency to be able to both excite the transmon and measure the emission up to the first nine modes of the metamaterial. We record the coherent emitted field, $\langle \Psi | a | \Psi \rangle$, of the metamaterial. Because the expectation value of the field amplitude of a Fock state $|n\rangle$ is equals 0, $\langle n|a|n\rangle = 0$, we bring our transmon into a superposition state with a $\pi/2$ pulse. We create the atom-photon bound state, let it stabilize for 40 ns, and finally, quench it quickly.

We measure the coherent component, $\langle a_{\text{out}} \rangle$, of the outgoing field from the output port of the metamaterial for 20 μ s [Fig. 4.6(b)]. The FFT of the emitted field shows peaks at the lowest frequency first nine modes of the metamaterial [Fig. 4.6(c)].

We demodulate the emitted field to extract the corresponding emission from each of the metamaterial modes [Fig. 4.6(d) for modes 1, 4, and 7]. From this measurement we observe that the decay time for the modes closer to the band-edge is longer than for those closer to the center of the band. This result is expected from the dispersion relation in our system. The modes at the band-edge, with a group velocity approaching 0, interact less with the ports, and they decay more slowly compared to those at the middle of the band.

We model the decay as an exponential function, Ae^{-t/τ_n} and $\kappa_n = 2\pi/\tau_n$ and compare the extracted decay rates, κ to the expected trend from tight-binding model in Eq. 4.12 [Fig. 4.6(e)]. There is a correspondence between the two of them. We attribute the deviations to a small SNR in the least-participant modes.

$$\kappa_n = \kappa \sin^2 \left(\frac{\pi(n+1)}{N+1} \right), \quad n = 0, 1, \dots, N-1$$
(4.12)

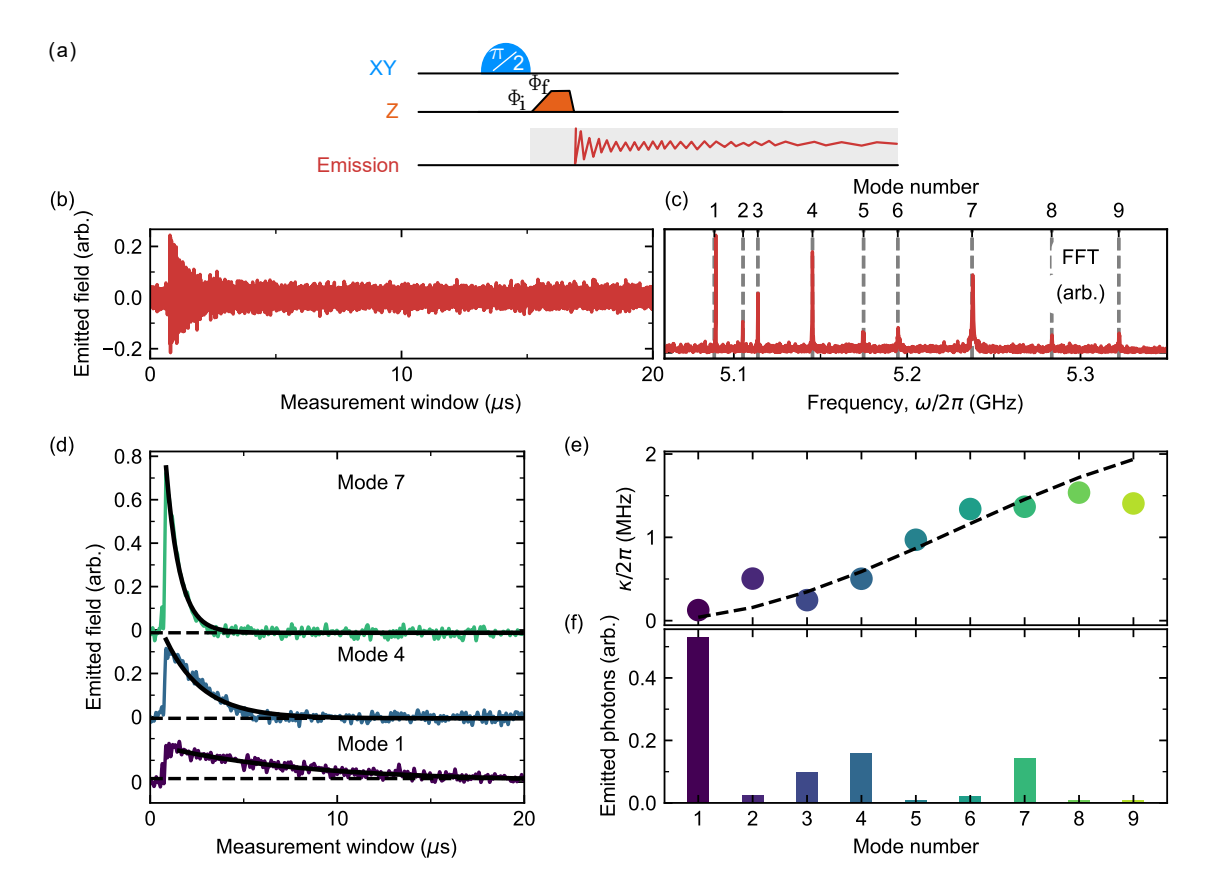


Figure 4.6: **Emission of an atom-photon bound state.** (a) Pulse sequence of the measurement. (b) Time trace of the emitted field over 20 μ s. (c) FFT of the emitted field. (d) Demodulated data for modes 1, 4, 7. (e) Decay rate of the emitted signal compared to the expected one from the tight-binding model. (f) Proportion of the emitted photons from each mode.

In this expression, κ is the decay rate of the center mode, n is the mode number, and N+1 is the total number of modes. Since we cannot estimate the value of κ directly from our measurements, we use it as a fitting parameter. Finally, by integrating the demodulated traces and then taking the results' complex conjugate, we extract the relative number of photons emitted, $\langle a_{\text{out}}^{\dagger} a_{\text{out}} \rangle$, at each mode [Fig. 4.6(f)].

A quench in the emitter frequency effectively "freezes" the system, trapping the populations in the instantaneous eigenstates that existed just before the quench. As a result, the photonic component of these pre-quench states is released into the metamaterial as propagating modes, which eventually decay into the output port and then detected at the output port, with a linear-amplification measurement chain.

We interpret the measured $\langle a_{\rm out}^\dagger a_{\rm out} \rangle$ as a decomposition of the photonic part of the APBS, allowing us to extract a quantitative measure of the relative probability densities described by Eq. 4.8. Since the emission originates from a single excitation initially localized in the APBS, the resulting photonic modes are expected to be quantum mechanically entangled. However, a detailed analysis of the correlations between these modes, necessary to confirm and characterize their entanglement, is beyond the scope of this work and left for future investigations.

4.7 Control of the emission of an atom-photon bound state

We explore the conditions for the formation of the atom-photon bound state and their effect on the final mode composition by changing the final frequency of the atom-photon bound state through Φ_f ; we study the dynamics of the formation through τ_r . The pulse sequence of our measurement is similar to that in Fig. 4.6 but includes the two tuning parameters in the flux pulse [Fig. 4.7 (a)]. Therefore, we drive the transmon into a superposition state with a $\pi/2$ pulse, apply the flux pulse with variable Φ_f or τ_r , and quench the APBS. We finally measure the emission of the photonic populations of the APBS.

We create the APBS adiabatically with a variable final emitter frequency [Fig. 4.7 (a), (d)]. When the emitter is far away from the transmission band, there is no emission, as the APBS is not formed yet. As the emitter approaches the band edge, the emission from the lowest energy mode increases until it saturates close to the band edge. This trend is interpreted as the full hybridization of the transmon with the metamaterial and the formation of the APBS, with an increase in its photonic component as the emitter and metamaterial hybridize. This trend is captured by our model with some quantitative difference in the detuning from the band-edge.

In addition, we have a non-monotonic participation of the rest of the modes with an exponential increase within the transmission band. This participation depends mainly on the specific coupling of the emitter to the metamaterial modes. Our effective model does not capture this trend.

The effect of the dynamics in the creation of the APBS [Fig. 4.7(c),(e)] from adiabatic to non-adiabatic regime shows a transition from single to multimode emission with exponential increase in the participation of modes closer to the band center. Our model captures this trend, albeit with a deviation of approximately 100 ns.

4.8 Discrepancies between experimental results and the effective model

We attribute these deviations between experimental results and effective model to a combination of following factors:

1. Incorrect estimation of the coupling parameters between the emitter and the transmission modes in the metamaterial:

We extract coupling values by fitting the spectroscopy data. This method can introduce errors, especially for band-edge modes. These modes interact less with the environment and need stronger driving, which can shift their frequency response due to their nonlinearity.

We attribute to this factor the deviations in the peaks and frequency components in Fig. 4.5(c),(e), and the non-monotonic participation of the modes close to the band-edge in Fig. 4.7(b),(d).

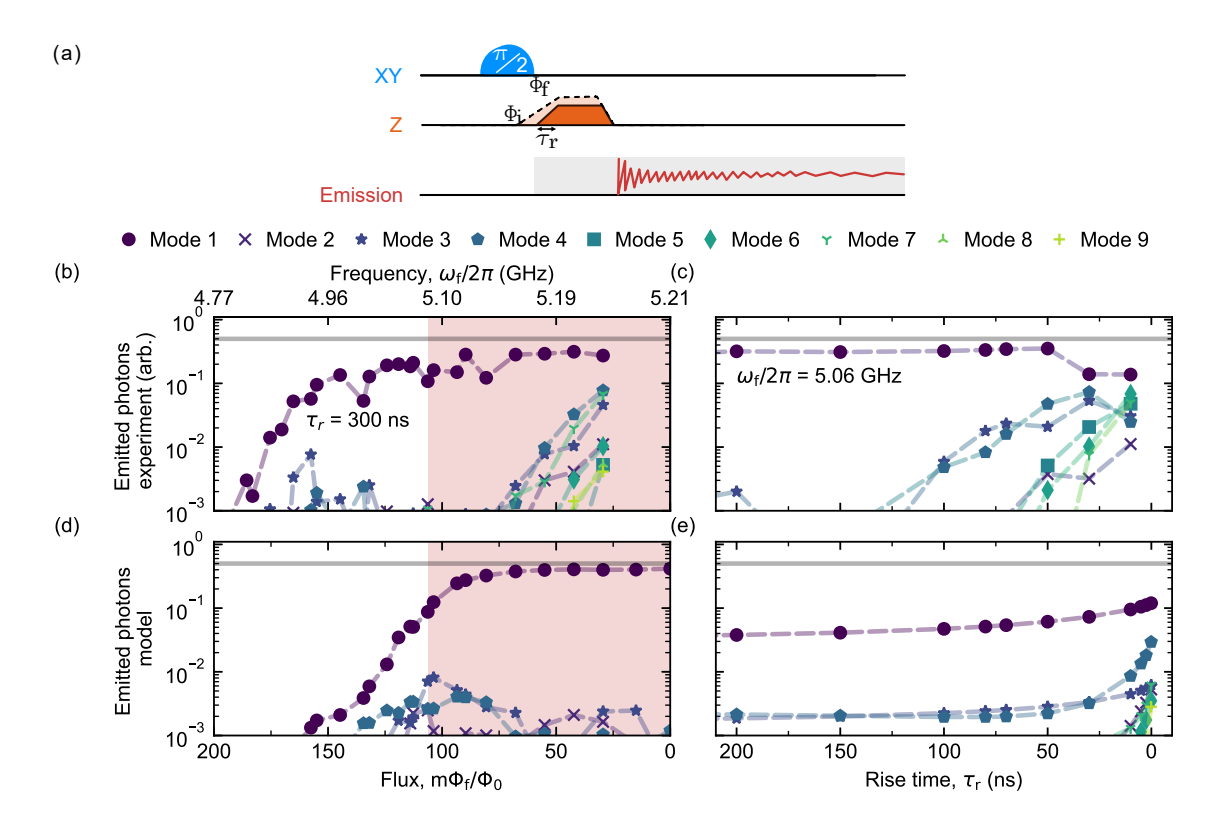


Figure 4.7: Control and modelling of the emission. (a) Pulse sequence. (b) Recorded emitted photon number for an adiabatic formation of the atom-photon bound state with different final frequencies. (c) Recorded emitted photons number depending on the dynamics in the formation of the atom-photon bound state close to the band-edge. (d) Effective model prediction of (b). (e) Effective model prediction of (c).

2. Uncorrected flux line:

Flux pulses experience distortions in its profile as they propagate through various microwave components in the flux line. A dominant distortion arises from low-pass filters causing square pulses to be smeared into a smoother shape, thereby altering their effect on the device [130, 131] and changing the dynamics.

This effect could explain the deviations in the peaks and frequency components in Fig. 4.5(c),(e), and the exponential increase in the emission within Fig. 4.7(b),(d), and the discrepancy in the transition between the adiabatic and non-adiabatic regimes in Fig. 4.7(c),(e).

3. Uneven coupling to the measurement ports:

The disorder in our system can also affect the way that the different modes couple to the ports. In this work, we only capture the emission from the output port and lose the information at the input port.

This effect affects the relative proportion of the emission into the different modes, and it is reproducible over repetitions of the experiment.

4.9 Conclusion

In this experiment, we used a metamaterial, with transmission bands and band-gaps. By coupling an emitter to this engineered environment, an atom-photon bound state is formed. In this atom-photon bound state, the photonic component becomes spatially localized around the emitter as a result of the metamaterial's photonic band-structure, particularly near the edges of a band gap.

Our experiment studies the dynamics of the formation and melting of an atomphoton bound state. We identify the adiabatic and non-adiabatic regime and the threshold between them. In addition, we directly measure the melting of an atomphoton bound state following the quench of the emitter's frequency, by detecting its emitted radiation of its photonic component. Our study of this emission yields a direct measure of the relative photonic probability densities in the atom-photon bound state, a study not reported before. We expect our work to be used as a new methodology for studying more exhotic bound states.

Chapter 5

Dissipation engineering and emergent dynamics in a metamaterial

5.1 Introduction

In this chapter, we study a first-order dissipative phase-transition that occurs in a Bose-Hubbard metamaterial. Unlike closed systems, which evolve with purely unitary dynamics, open quantum systems exchange energy and information with their environment. By engineering dissipation channels and tuning a coherent drive, it is possible to stabilize well-defined non-equilibrium steady states that lack an equilibrium analogue [132–143].

Dissipative phase transitions occur when a steady state undergoes a qualitative change as an external control parameter, such as drive amplitude or frequency detuning, is varied. In first-order transitions, the system exhibits bistability, characterized by the coexistence of two distinct steady states connected by a discontinuous jump. Near the transition line, the relaxation dynamics slow down markedly, with timescales that can exceed the system's intrinsic rates by orders of magnitude. Such transitions have been extensively studied theoretically [132–143], and observed experimentally across a variety of platforms, including cold atomic gases [144–147], semiconductor quantum dots [148–151], and superconducting circuits [7, 152–163]. To date, however, dissipative phase transitions had not yet been experimentally explored in Bose–Hubbard metamaterials, which we address in Paper 2.

In this work, we study the driven-dissipative dynamics in a 1-D superconducting metamaterial implementing a Bose-Hubbard lattice. In our experiments, we observe signatures of a multimode first-order phase transition with record coherence times, as high as 143 s. In addition, this work proves the existence of this type of transitions in a Bose-Hubbard lattice, that was theoretically dismissed earlier [164].

This chapter is structured as follows: Section 5.2 introduces a standard theoretical framework used to describe and understand first-order dissipative phase transitions. In Section 5.3, we present the experimental implementation of our platform. In Section 5.4, we present the theoretical framework we use to model our experiments.

In Section 5.5, we explain our spectroscopy measurements showing the multimode nature of the transition. In Section 5.6, we reconstruct the emission characteristics and map the phase diagram of the transition. In Section 5.7, we analyze the system's dynamical response and validate the phase diagram. Finally, in Section 5.8, we conclude our findings.

5.2 Liouvillian interpretation of first-order dissipative phase transitions

An intuitive way to understand the emergence of dissipative phase transitions is through the Liouvillian formalism [136]. In what follows, we use this framework to illustrate the concept of dissipative phase transitions, even though our experimental results are not explicitly modeled within this formalism.

5.2.1 Liouvillian

We describe our open quantum system using the Lindblad master equation (Sec. 2.7, Eq. 2.18),

$$\dot{\rho}(t) = \mathcal{L}\rho(t),\tag{5.1}$$

where the Liovillian superoperator, \mathcal{L} , describes the dynamics of the system. In practice, this means that the time evolution of the density matrix is always physical: it preserves probabilities (trace preserving) and does not produce unphysical states (completely positive).

For a time-independent Liouvillian, there is always at least one steady state, ρ_{ss} , defined by

$$\mathcal{L}\rho_{ss} = 0 \tag{5.2}$$

This steady state is the long-time limit of the dynamics and, under general conditions, is unique.

To understand not just the final state but the entire relaxation process, we look at eigenvalue spectrum of the Liouvillian. Its eigenvalues describe how different modes of the system decay or oscillate in time. The zero eigenvalue corresponds to the steady state, while all others have negative real parts, which set the rates at which excitations decay away. Imaginary parts, if present, mean oscillatory response.

The slowest of these decays is of particular importance. We call this the Liouvillian gap, defined as the smallest (in magnitude) nonzero decay rate. It sets the timescale over which the system relaxes to its steady state. If the Liouvillian gap is large, the system relaxes quickly; if the gap is small, relaxation is slow.

5.2.2Dissipative phase transitions

Dissipative phase transitions occur in driven open quantum systems when their steady-state behavior changes abruptly as a control parameter (for example, pump power or detuning) is varied. Instead of relaxing to a single steady configuration, the system can support multiple steady states [136].

From an experimental point of view, these transitions show up as sudden changes in a measurable quantity: the system may abruptly switch between distinct states of light intensity, resonance frequency, or qubit population. The underlying reason comes from the spectral properties of the Liouvillian. At the transition point, the so-called Liouvillian gap closes. Physically, this means the system takes longer and longer to relax, a phenomenon known as critical slowing down. Near the transition, switching between states becomes rare and slow, which is a direct signature in time-trace measurements.

5.2.3 First-order dissipative phase transition

A first-order dissipative phase transition is the non-equilibrium analog of a first-order transition in thermodynamics, such as liquid–gas condensation. At the transition point, the system does not gradually change from one phase to another—instead, the steady state jumps from one solution to a different one. Concretely, when the control parameter is below the transition threshold, the system relaxes into one steady state, while above the threshold it stabilizes in a completely different state. Exactly at the transition point, both states can coexist, and the system may randomly switch between them. In experiments, this manifests as bistability: the system can remain in either a dim or a bright state, depending on fluctuations, history, and noise.

Near the transition point, the system often spends long times trapped in one of two metastable states before eventually hopping to the other. This leads to phenomena such as hysteresis (the observed state depending on the direction of the parameter sweep), metastability (long-lived but not permanent states), and extremely slow relaxation times—sometimes orders of magnitude longer than the system's natural timescales. These are the hallmarks of first-order dissipative phase transitions.

5.3 Experimental implementation

We consider the one-dimensional Bose–Hubbard chain shown in Fig. 5.1 and simulate its dynamics using the metamaterial introduced in Section 4.2. In Section 4.2, we modeled the system as an array of linear resonators, which was sufficient when restricting ourselves to the single-excitation manifold. However, in the present case, the number of injected photons is large enough that the system's intrinsic nonlinearity, U, must be taken into account. The Hamiltonian that describes the system is given by

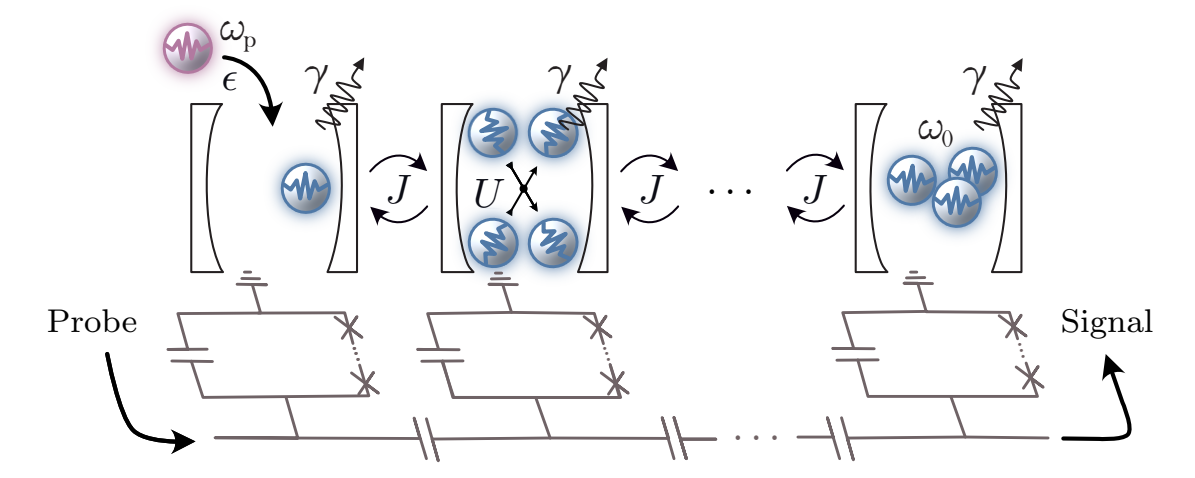


Figure 5.1: Schematic of a one-dimensional Bose-Hubbard chain. We include the intracavity coupling J, a pump with power ϵ and frequency ω_p , dissipation γ , and non-linearity U. The equivalent circuit diagram is also included.

$$\frac{H}{\hbar} = \omega_{\rm r} \sum_{i=1}^{N} a_i^{\dagger} a_i - J \sum_{\langle i,j \rangle}^{N} a_i^{\dagger} a_j - \frac{U_{\rm r}}{2} \sum_{i=1}^{N} a_i^{\dagger 2} a_i^2 + \epsilon \sqrt{U/\gamma} \left(a_0 e^{-i\omega_{\rm p} t} + a_0^{\dagger} e^{i\omega_{\rm p} t} \right)$$
(5.3)

In this model, a_i and a_i^{\dagger} denote the annihilation and creation operators for the i-th cavity, while ω_0 specifies the common resonant frequency of all cavities. The parameter U_i characterizes the strength of the on-site Kerr nonlinearity, J sets the hopping rate between neighboring sites, ϵ is the normalized drive amplitude, and ω_p is the frequency of the external pump. Each cavity is subject to photon loss, described by a Lindblad dissipator with decay rate γ in the Lindblad master equation.

The Hamiltonian terms have clear physical interpretations: the first represents the energy of the cavity modes (assuming identical resonators), the second accounts for photon tunneling between adjacent sites, the third introduces the nonlinear interaction that penalizes multiple excitations within a single cavity, and finally, the fourth term drives the system by coherently injecting photons into the first site. Dissipation into the environment is captured by the Lindblad term.

The behavior of the system at low power without adding any pump can be modeled using a tight-binding model, already used in Section 4.4, from which we extract $\omega_r/2\pi \approx 5.43$ GHz and $J/2\pi \approx 209$ MHz. In addition, we obtain the total loss of the center resonator by fitting the expression $S_{21}(\omega) = 2\frac{\kappa}{\gamma + 2i(\omega - \omega_0)}$ [165]. In this expression, κ is the total radiative decay to both the input and output ports, and γ is the total decay. We obtain $\gamma/2\pi \approx 1$ MHz with a non-radiative decay $\gamma_{\rm nr}/2\pi = 10.25$ KHz for mode thirteen, the pumped one in the following experiments. Deviations from the previous numbers reported in Section 4.4 arise from the aging of the Josephson junctions in our metamaterial, which changes the frequency of the modes [166].

5.4 Theoretical model

We model our system using the Hamiltonian in Eq. 5.3, but expressed in terms of the modes in the system as

$$H/\hbar = \sum_{k=1}^{N} \omega_k a_k^{\dagger} a_k - \frac{U_r}{2N} \sum_{k,p,q=1}^{N} a_{p+k}^{\dagger} a_{q-k}^{\dagger} a_p a_q,$$
 (5.4)

with ω_k the frequency of mode k. The second term sum contains self-Kerr terms $\propto a_k^{\dagger 2} a_k^2$, cross-Kerr terms $\propto a_q^{\dagger} a_q a_p^{\dagger} a_p$, and finally photon conversion terms that we neglect on the basis that they are not energy-conserving (RWA).

Since the external pump is nearly resonant with a single mode of the array, we assume that only this mode is populated. The other modes are affected only indirectly, through frequency renormalization caused by the cross-Kerr effect. With this approximation, the multimode dynamics reduce to an effective single-mode description.

In the rotating frame of the pump, the Hamiltonian becomes

$$H = -\Delta a^{\dagger} a - \frac{U}{2N} a^{\dagger 2} a^2 + \sqrt{\frac{U}{\gamma N}} \epsilon (a^{\dagger} + a), \qquad (5.5)$$

with $\Delta = \omega_p - \omega_0$ the detuning between the pump frequency and the bare resonance, and ϵ the effective pump strength normalized by the interaction energy. Dissipation is included through the Lindblad operator

$$L = \sqrt{2\gamma}a,\tag{5.6}$$

with γ the photon decay rate.

This driven-dissipative Kerr oscillator provides the textbook example of optical bistability [167]. Depending on the detuning, Δ , and drive strength, ϵ , the system settles into two distinct semiclassical steady states: a low-photon "dim" state or a high-photon "brigh" state. Although it is guaranteed theoretically that the quantum steady state is strictly unique [168], in practice the system exhibits rapid switching between the two classical solutions, giving rise to hysteresis in response to slow parameter sweeps. These features mirror the general discussion of dissipative phase transitions introduced earlier. As the system approaches the transition, relaxation becomes increasingly slow, and fluctuations can drive rare jumps between competing states.

As the effective nonlinearity, quantified by $U/(\gamma N)$, decreases, the photon population grows to macroscopic values. In this regime, quantum fluctuations are suppressed and mean-field description becomes increasingly accurate. This behavior can be interpreted as approaching a thermodynamic limit, due to the large number of particles in interaction; this connection to a thermodynamic limit can be formalized via a path-integral treatment [169].

In our platform, nonlinearity is further reduced by the presence of $N_{\rm JJ}$ Josephson junctions in the unit cell, which leads to an effective scaling:

$$U' = \frac{U}{\gamma N N_{\rm IJ}^2}. (5.7)$$

With the experimental parameter, $U/(\gamma N N_{\rm JJ}^2) = 0.123$, placing the system well within the regime where the mean-field description accurately captures the observed dissipative phase transitions.

From mean-field theory, we extract the nonlinear steady-state equation

$$\left(1 + \left(\frac{\Delta}{\gamma} + |\alpha|^2\right)^2\right) |\alpha|^2 = \frac{\epsilon^2}{\gamma^2} \tag{5.8}$$

In this equation, $\alpha = \sqrt{U/\gamma N \langle a \rangle_{\rm ss}}$ defines the mean field value of the photon annihilation operator, and $\langle a \rangle_{\rm ss}$ the quantum steady state expectation value of the photon annihilation operator. The solutions of this expression give two bistable solutions.

5.5 Observation of multimode phase transitions

We measure the transmission parameter through our metamaterial, similar to what is shown in Fig. 4.2. In this experiment, however, we introduce an additional pump signal, which we vary in both frequency and power [Fig. 5.2]. To make the results comparable, the input power is normalized by the total decay rate of the system, γ . At low input power, $\epsilon/\gamma = 0.14$, the transmission spectrum is unaffected, and we clearly resolve 21 peaks corresponding to the 21 modes of the metamaterial array. As we increase the input power to $\epsilon/\gamma = 14.07$, the spectrum is altered qualitatively: the transmission becomes pump-dependent, and the metamaterial modes shift in frequency along with the pump. This is the regime we focus on in detail, as the frequency jumps observed here are the hallmark of a first-order dissipative phase transition. When the power is increased further, to $\epsilon/\gamma = 28.08$, the metamaterial's state has crossed this transition. In this high-power regime, we observe the disappearance of certain transmission modes—a signature of chaos.

We examine in more detail the pump power at which the system enters the regime of dissipative phase transitions [Fig. 5.3]. When the pump frequency approaches any of the resonant frequencies of the metamaterial array, all modes undergo a collective frequency shift of a few tens of MHz, a clear experimental signature of the dissipative phase transition.

We perform spectroscopy measurements focusing on two modes of the array, with the pump frequency swept faster than the system's relaxation rate near the transition [Fig. 5.4]. Under these conditions, the system cannot fully stabilize, and the frequency at which the system undergoes a shift depends on its prior state. Specifically, when sweeping the pump frequency downward, the jump occurs at $\omega_p/2\pi=5.3463$ GHz, whereas when sweeping upward, the jump occurs at $\omega_p/2\pi=5.3493$ GHz. This hysteresis is a hallmark of bistability, arising at the phase transition between the bright (high-population) and dim (low-population) states. Therefore, the sharp

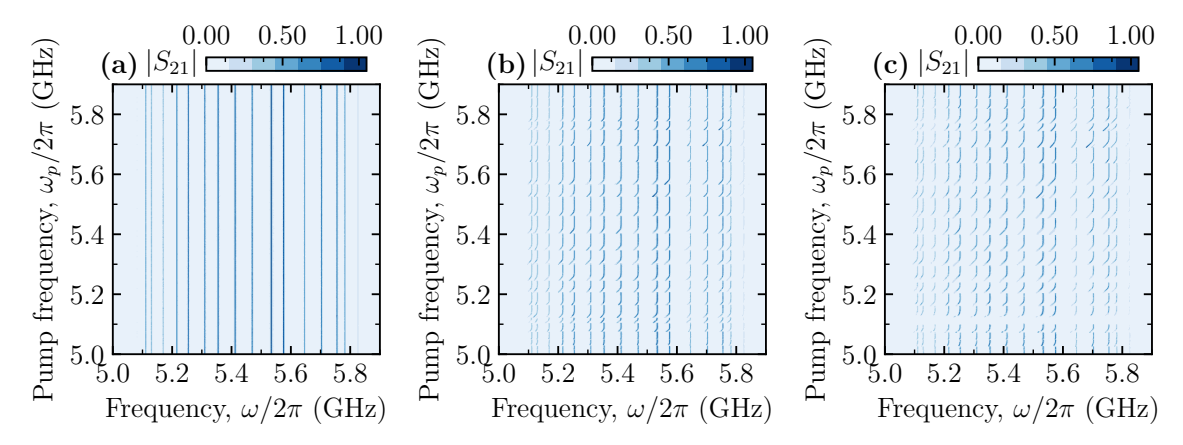


Figure 5.2: Transmission spectrum as a function of pump frequency and pump power. (a) Low pump power $\epsilon/\gamma = 0.14$. The transmission response is not affected by the pump. (b) At intermediate powers, $\epsilon/\gamma = 14.07$, first-order transitions emerge. (c) At high pump power $\epsilon/\gamma = 28.08$, some modes disappear.

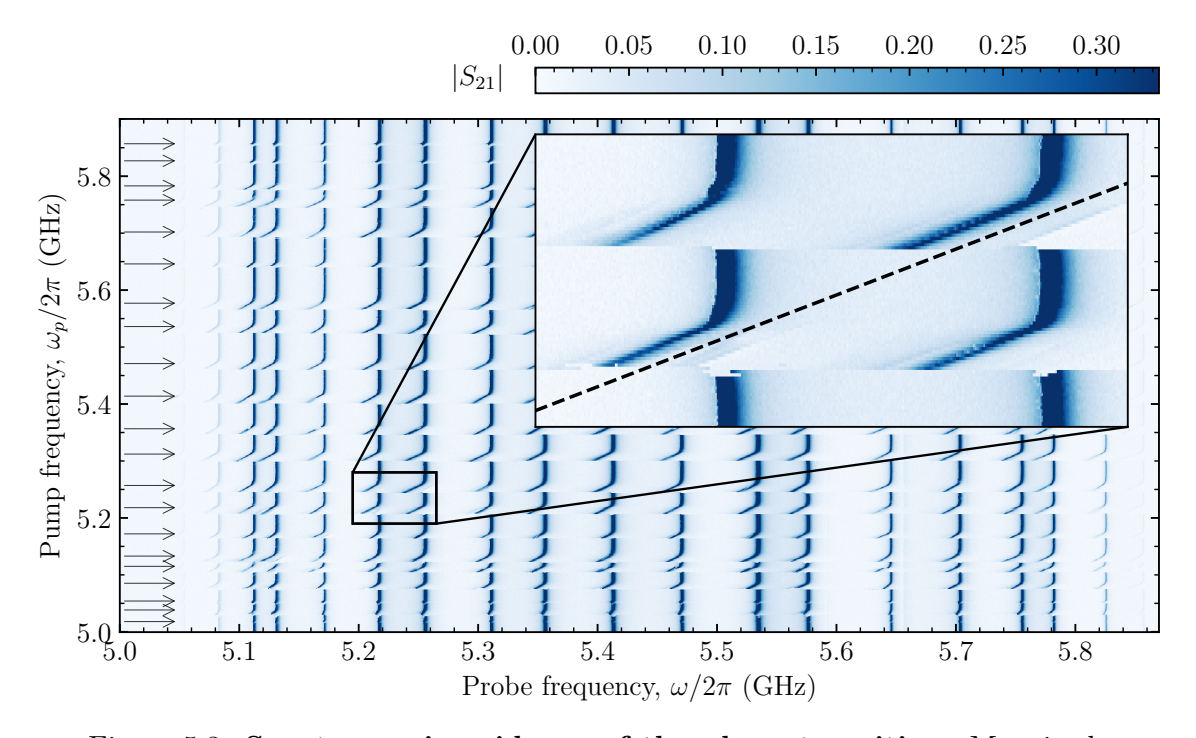


Figure 5.3: Spectroscopic evidence of the phase transition. Magnitude of transmission parameter across the chain, $|S_{21}|$ as a function of probe and pump frequencies at a fixed pump amplitude $\epsilon/\gamma=14.07$. Each horizontal arrow corresponds to the resonant frequency of a mode of the chain. When the pump is close in frequency to any of the modes (dashed black line in the inset), the resonance frequencies of all modes shift abruptly.

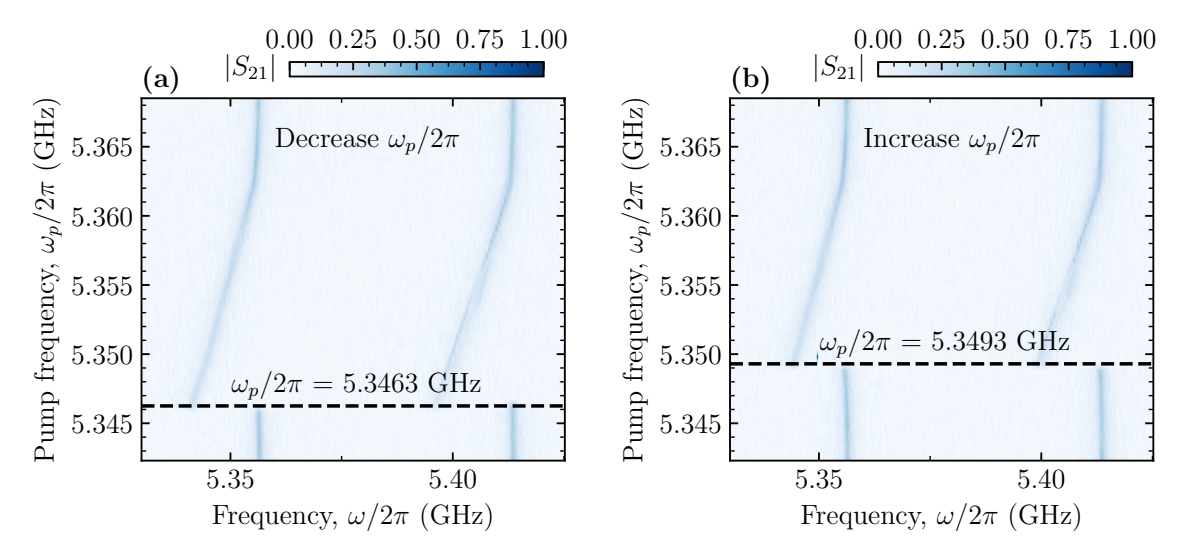


Figure 5.4: Measurement of the hysteresis of the system. (a) Transmission when the pump frequency is decreased from $\omega_p/2\pi \approx 5.368$ GHz to $\omega_p/2\pi \approx 5.343$ GHz. The system jumps at $\omega_p/2\pi = 5.3463$ GHz. (b) Same as (a) but with the pump frequency increases from $\omega_p/2\pi \approx 5.343$ GHz to $\omega_p/2\pi \approx 5.368$. The system jumps at $\omega_p/2\pi = 5.3493$ GHz.

jumps arise at the limits of the bistable region, where the metastable configuration collapses and the system reverts to its ground state.

Solving the mean-field equation for the quasi-resonant mode 5.4 gives the pole of the response function, whose real part defines the renormalized mode frequency

$$\omega_* = \sqrt{(\Delta + 2\gamma |\alpha|^2)^2 - \gamma^2 |\alpha|^4} + \omega_p, \tag{5.9}$$

The amplitude α is obtained from solving the mean-field equation 5.8. To test the theory, we compare the experimental normalized frequency shift of the pumped mode, $(\omega^* - \omega_0)/\gamma$, with the theoretical prediction, as a function of the applied pump amplitude ϵ . for the pumped mode with the theoretical prediction as a function of the drive power ϵ . A single global scaling factor is used as the only fit parameter [Fig. 5.5(a)]. Remarkably, this single parameter accurately captures the behavior over the full range of pump powers, across both sides of the transition. The excellent agreement demonstrates the validity of our theoretical model.

In addition, we require to model the effect on the other modes due to the cross-Kerr term. From our Bose-Hubbard model, we can extract the value of the self- and cross-kerr by diagonalizing the site-equation 5.3 and re-expressing the Kerr term in the mode basis. We find that the photon population in the quasi-resonant mode induces a frequency shift in all other modes of magnitude $4U/3\langle a_0^{\dagger}a_0\rangle \simeq 4\gamma |\alpha|^2/3$. When normalized to the scaled shift $(\omega_i - \omega_0)/\gamma |\alpha|^2$, we obtain the global shift for all of the modes of 4/3. Experimentally, we confirm this prediction by measuring the shift of the 6 center modes while pumping the center one. Despite the presence of disorder, the extracted values agree well with the expected factor of 4/3 4.2 [Fig.5.5(b)]. By contrast, the pumped mode itself exhibits a shift given by 5.5.

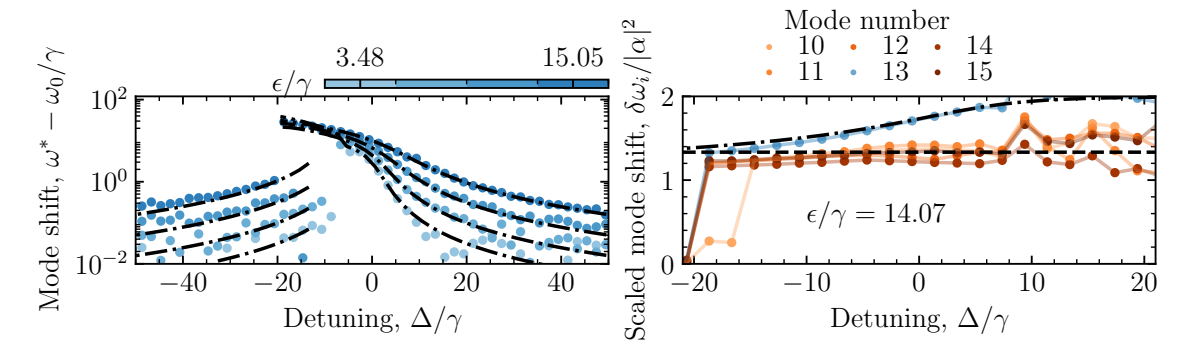


Figure 5.5: Comparison of the measured spectroscopy with the theoretical model. (a) Frequency shift of mode 13 (the pumped mode) at different pump amplitudes. The circles represent the experimental data, while the dashed curves represent the theoretical model.(b) Scaled mode shifts for selected modes when pumping mode 13. The dashed lines are the model results.

5.6 Emission from the phase transition and phase diagram

As discussed earlier, the transmission through the metamaterial is hysteretical and cannot be used to directly determine the transition line between the "bright" and "dim" states. To extract this transition more reliably, we instead analyze the system's emission at the phase boundary using the power spectral density (PSD) as a function of the pump frequency and amplitude [Fig.5.6(a),(b),(c)].

This approach does not require a probe tone to track the mode frequency, unlike in the spectroscopic measurement, so the probe is inactive during these measurements. In addition, to reduce unwanted thermal noise and fluctuations, we perform the measurements in an interleaved fashion: alternating between the pump active (ON) and the pump inactive (OFF) conditions and taking the difference of the corresponding spectra. This interleaving scheme ensures that the measurement is robust against signal drifts originating, for example, from the amplification chain. The PSD is collected over a 450-MHz bandwidth centered on the pumped mode. The pump is varied in frequency and amplitude, and its direct contribution is eliminated from the recorded spectra in post-processing by filtering around the pump frequency.

Depending on the pump power, we observe two regimes [Fig. 5.6(a-b)]. When the input power is moderate, $\epsilon/\gamma=1.5$, the emission occurs around the frequency of the pumped mode. However, at higher powers, $\epsilon/\gamma=9.5$, the emission becomes multimode, signaling the onset of a collective behavior. Our model, based on a single-mode transition, can only capture the behavior at moderate powers.

We take a closer look at the transition at moderate power to further investigate this regime [Fig. 5.6(c)] and use our model to reproduce this behavior [Fig. 5.6(d)]. The spectrum is obtained from the Keldysh formalism and is given by [170].

$$S_{\text{incoh}}(\omega) = \frac{2|\alpha|^4}{\left(1 + \left(\frac{\omega - \omega_*}{\gamma}\right)^2\right) \left(1 + \left(\frac{\omega + \omega_*}{\gamma}\right)^2\right)}$$
(5.10)

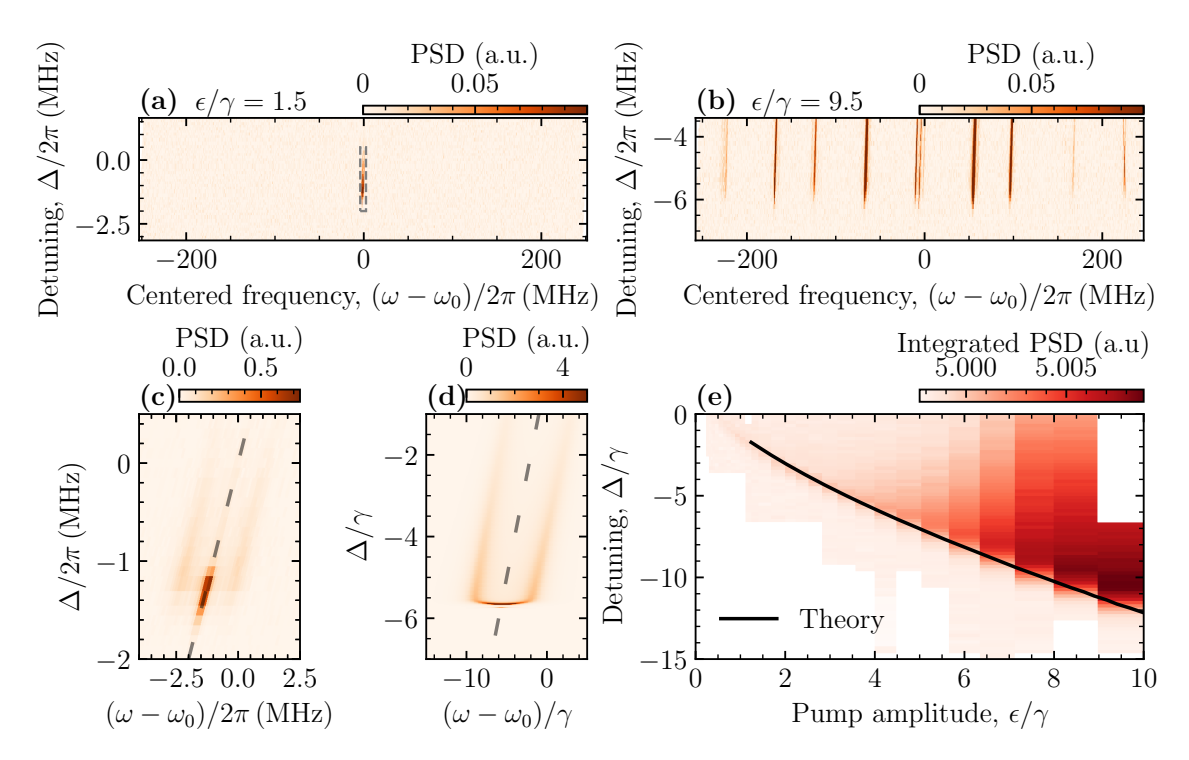


Figure 5.6: Photon emission from the metamaterial. (a) Power spectral density (PSD) as a function of pump detuning at $\epsilon/\gamma=1.5$. In this regime, only the quasi-resonant mode emits. (b) PSD versus detuning at $\epsilon/\gamma=9.5$. Additional modes of the chain emit. (c) Zoomed-in view of the emission spectrum of the resonant mode in (a). (d) Theoretical prediction for the emission spectrum shown in (c). (e) Integrated PSD as a function of detuning and pump amplitude. Regions of high emission correspond to large photon occupation in the mode, revealing a phase boundary between dim and bright states. The numerically computed transition line is shown as a black curve.

When the system is in the dim state, $|\alpha|$ is very small, and no emission is observed. At the transition, a single emission peak appears, and at the bright state, there are two peaks symmetric to the pump frequency at $\omega_p - \omega_*$ and $\omega_p + \omega_*$. Therefore, from this measurement, we can extract the point of transition for each pump frequency and amplitude, forming the transition line.

Integrating the PSD yields an estimate of the number of photons emitted by the metamaterial [Fig.5.6(e)]. If we, therefore, integrate the PSD for different normalized pump detunings, Δ , and amplitudes, ϵ/γ , we can extract the phase diagram of the transition. The fitted amplitude shows a difference of 4 dBm between the spectroscopy and PSD measurements. We attribute this difference to the power injected by the probe tone in the spectroscopy measurements.

5.7 Dynamics of the transition

We measure the dynamics of our system by tracking the system at the dim-state frequency, which is signaled as a peak in transmission parameter while applying the pump. Therefore, whenever the system evolves from this state, there will be

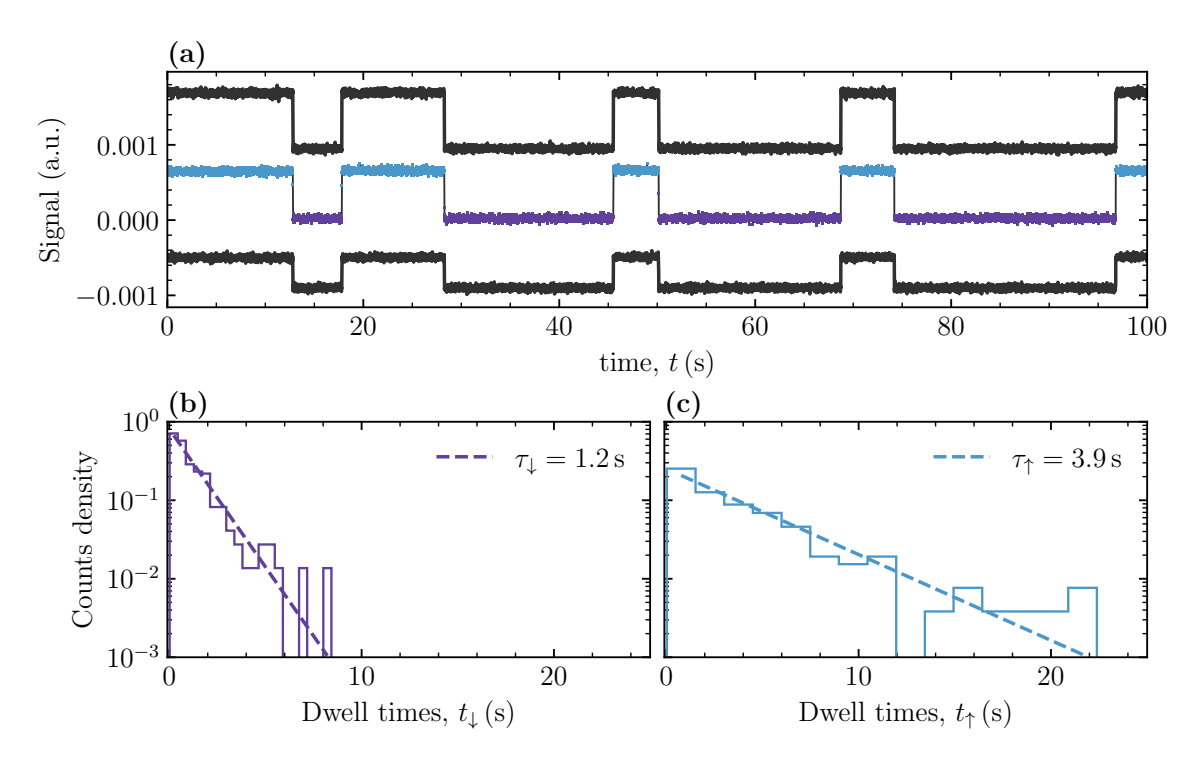


Figure 5.7: Multimode dynamcs of the system. (a) Time-traces for three selected modes, showing that the system switches between the two states collectively. The pumped mode is colored and adjacent modes are left in black. The bright dwell times are colored in purple, the dim dwell times in blue. (b) and (c) Selected histograms of the dwell times showing an exponential distribution. Modelled exponential density probability functions as dashed lines, providing the characteristic dwell times.

a dip in the signal. We acquire the time-resolved traces for three selected modes with an integration time of 0.01 s [Fig.5.7(a)]. We observe that all modes switch simultaneously between the two states.

We study the dynamics by extracting the average dwell times in the bright state, t_{\downarrow} , and in the dim state, t_{\uparrow} . The transitions are expected to follow Poissonian statistics, with probability distribution $P(t) = \frac{1}{\tau} \exp(-t/\tau)$ and characteristic dwell times τ_{\uparrow} and τ_{\downarrow} , respectively. Our experimental data confirms this expectation: the dwell-time histograms are well described by exponential decay [Fig. 5.7(b)].

In addition, we verify that our results were not contaminated by other sources of errors by applying an Anderson-Darling test [171] and rejecting time traces failing at 15%.

We study the dynamics across the bistable region by varying the detuning of the pump frequency [Fig. 5.8]. These rates are expected to obey a generalized Boltzmann form $1/\tau \propto \exp(-E(\Delta, \epsilon)/U)$, where E represents an activation barrier and U measures the strength of the quantum fluctuations triggering the jumps [169]. Assuming that the activation barrier is constant through the bistable region, the rates vary exponentially around in the region, with the dim rates reducing and the bright rates increasing. At the crossing point, the system has an equal probability of being in either of the two states. This crossing corresponds to the transition point.

We measure the dwell times for different pump amplitudes and extract the dwell times at the transition points $\tau_{\downarrow,\uparrow}$ [Fig.5.8(b)]. The dwell times cover three orders of magnitude. Therefore, we require to adjust accordingly both the integration time and the total measurement time accordingly. We impose, for the measurements, that at least 100 jumps should be recorded. We measure with integration times from 1 ms to 0.1 s and record dwell times from a few ms up to 143 s.

The statistical analysis of dwell times reveals a clear separation between two dynamical regimes. At small pump amplitudes, specifically for $\epsilon/\gamma < 9.5$, the residence times follow an exponential law, scaling as $e^{1.33\,\epsilon/\gamma}$. This scaling behavior is a hallmark of first-order transitions activated through tunneling processes, in agreement with established theoretical expectations [132]. In contrast, for amplitudes above this threshold, the exponential growth no longer persists: the dwell times saturate. Such a plateau suggests either a change in the underlying escape mechanism or the onset of systematic errors that become relevant at very long observation windows. The maximum dwell time observed in this regime reaches 143 s, which exceeds the longest values previously reported in comparable experiments [162].

To place these observations in the context of the rest of our experiments, we map the extracted transition points onto the phase diagram spanned by $(\Delta/\gamma, \epsilon/\gamma)$ [Fig. 5.8(c)]. A key feature of this analysis is that no adjustable parameters are required: the pump amplitude has already been calibrated for both probed and non-probed measurements. The comparison demonstrates striking consistency between the experimentally determined boundaries, obtained from jump-rate statistics, and the theoretical phase lines. Furthermore, this approach extends the reach of transition-line measurements well beyond the values extracted using power spectral density (PSD) data alone, covering larger detunings and stronger pump amplitudes. In doing so, it provides an independent and robust confirmation of the theoretical predictions while simultaneously broadening the experimentally accessible parameter space.

A systematic offset of approximately 4 dBm is consistently observed between transition frequencies obtained via power spectral density (PSD) measurements and those extracted from jump-rate analysis or direct spectroscopy. This discrepancy is explicitly incorporated into the fitting procedure in Fig. 5.8(c).

To uncover the physical origin of this offset, we investigated the influence of the probe on the system dynamics [Fig. 5.9]. Both the probe power and the number of simultaneously probed modes were found to strongly affect the observed rates, in line with earlier reports [157]. Interestingly, even small adjustments in probe power were sufficient to produce significant modifications.

Closer inspection reveals that increasing the probe amplitude at fixed pump parameters [Fig. 5.9(a)] effectively drives the system through the transition sequence: from the dim state, to the critical point, and finally into the bright state. This behavior mimics the effect of raising the pump strength directly. A parallel outcome arises when additional modes are probed [Fig. 5.9(b)]. Each added probe (0.2 a.u.) produces an apparent pump-power shift of roughly 4 dBm, which coincides with the systematic offset observed under standard single-probe conditions.

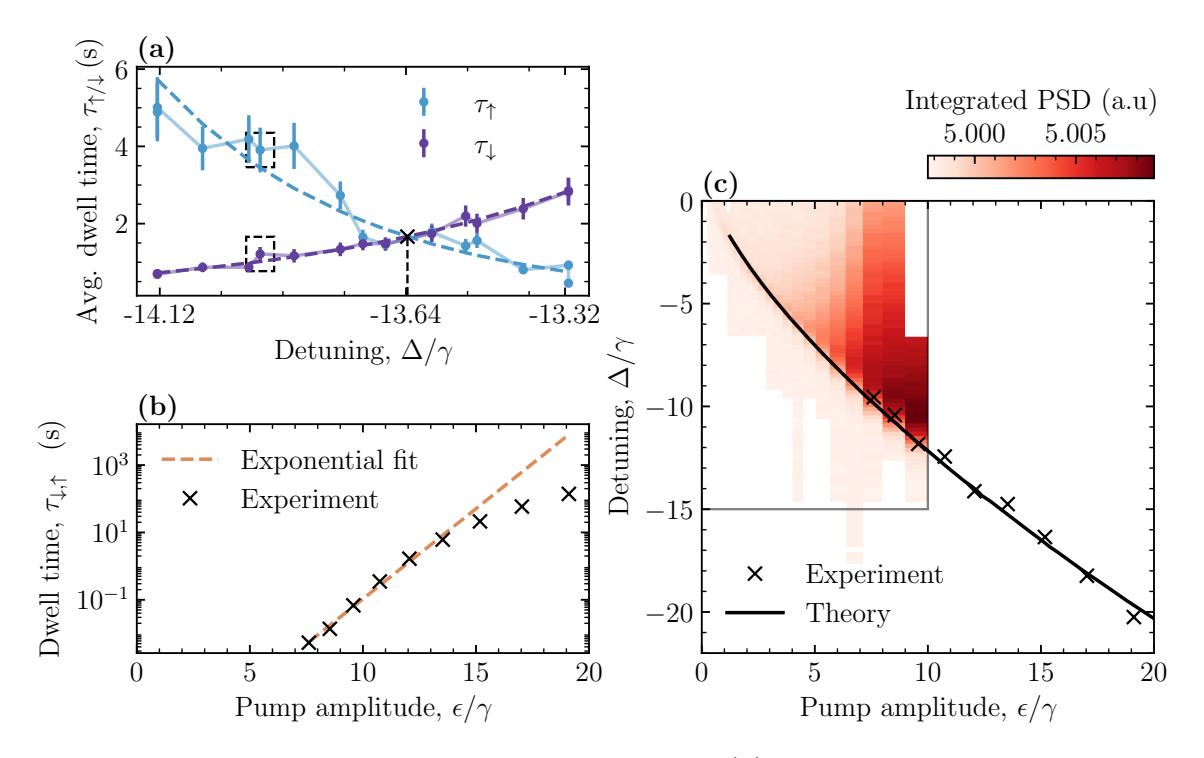


Figure 5.8: **Dwell times and phase diagram.** (a) Average dwell times of the bright and dim states across the transition at a fixed amplitude $\epsilon/\gamma=7.5$. Dashed line: theoretical prediction. (b) Dwell time at the transition point as a function of pump amplitude. Dashed line: exponential fit. (c) Phase diagram extracted from the PSD (color map), compared with that obtained from the dwell-time transition points (crosses) and with the theoretical prediction (black line).

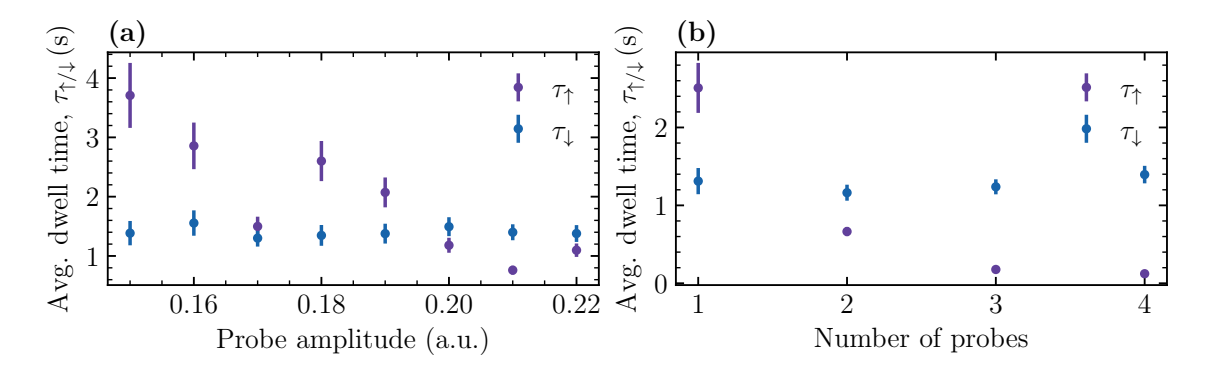


Figure 5.9: Effect of the probe tone in the dynamics. (a) Increasing the probe amplitudes. (b) Increasing the number of probes.

62 5.8. Conclusion

5.8 Conclusion

In this measurement, we have investigated the driven-dissipative dynamics of a one-dimensional superconducting Bose-Hubbard lattice. In this system, we identified and characterized a multimode first-order phase transition, directly confirming its existence where theory had previously ruled it out.

By combining power spectral density analysis with switching-rate statistics, we reconstructed the phase diagram and found excellent agreement with theoretical predictions, achieved without additional fitting parameters. Our measurements revealed dwell times as long as 143 s, the longest reported to date in such a platform, highlighting the remarkable stability of these non-equilibrium phases. Furthermore, building on previous proposals and based on the pronounced sensitivity of the transition to weak perturbations, we suggest this platform as a great candidate for quantum metrology and sensing.

Part III Conclusion

Chapter 6

Conclusion and outlook

In this thesis, we have studied a variety of superconducting quantum circuits implementing light–matter interactions between microwave modes and artificial atoms, unified by the themes of *Structured environments and engineered dissipation*. Our objective has been to understand and control how tuning the coupling to the environment, and the environment itself, influences the behavior of our quantum systems.

We implemented these ideas using a metamaterial platform composed of lumpedelement resonators with inductances provided by arrays of Josephson junctions. This arrangement enabled fine control over the photonic environment and served as a versatile system for studying different regimes of light-matter coupling. Within this framework, we performed two main experimental investigations.

In the first study, we coupled a quantum emitter to the structured metamaterial, forming a hybridized state known as an atom-photon bound state (APBS). Our experiments focused on the formation dynamics of this state, identifying the threshold between adiabatic and non-adiabatic regimes and characterizing the transfer of the emitter's population into the metamaterial modes. Once this effect was established, we studied the photonic composition of the APBS by preparing it adiabatically and subsequently quenching it. This approach allowed us to resolve the relative photonic populations in the metamaterial constituting the bound state. These results open new directions for investigating exotic emission processes from APBSs and provide valuable insight into their spectral structure.

The second study investigated collective phenomena arising in a weakly nonlinear metamaterial, where dissipation and photon injection act as competing processes. By continuously driving the system with a coherent pump, we uncovered a dissipative phase transition at the boundary between quantum and classical behavior in a Bose-Hubbard model, an effect not previously observed experimentally. Remarkably, all modes of the metamaterial transitioned synchronously between "dim" and "bright" states on exceptionally long timescales, far exceeding those reported in comparable systems. This observation provides new experimental evidence of critical behavior in driven–dissipative systems close to the thermodynamic limit and establishes the platform as a promising candidate for realizing quantum switches, and for quantum metrology and sensing.

6.1. Outlook

Furthermore, with two different setups and studies, we explored how the decay of an atom into a waveguide can be deliberately controlled.

In the first, we coupled two interacting atoms to two separate waveguides. The interaction between the atoms led to the formation of hybridized molecular-like modes. By carefully designing the coupling geometry, we achieved selective decay of each molecular mode into a specific waveguide, reaching a selectivity ratio of 50. This high degree of control opens new experimental possibilities in waveguide quantum electrodynamics (wQED), including deterministic Bell-state emission, photodetection, and applications in quantum thermodynamics.

In the second study, we engineered the decay of a qubit coupled to a readout resonator by incorporating a Purcell filter, designed to suppress unwanted relaxation while preserving fast dispersive readout. Our setup, made of lumped resonators with Josephson junctions arrays, has the advantage of being very compact. In our design, we kept a dispersive coupling between the readout mode and the qubit, 2χ and a coupling of the readout mode to the waveguide, κ , in the order of a few MHz. These couplings allow for fast, quantum non-demolition readout. In addition, we characterized the Purcell decay using an auxiliary transmon directly coupled to the waveguide as a power sensor. We obtained a single-shot fidelity between $|g\rangle$ and $|e\rangle$ and between $|g\rangle$ and $|f\rangle$ as high as 94.73 % and 89.50 %, respectively, in 1.9 μ s with 17 noise photons in the gain chain and a Purcell lifetime above 3 ms. This setup allowed for fast-readout with a good Purcell protection while keeping the system very compact, and opens new possibilities for scalable quantum computing.

Across these studies, a unifying theme emerges: structured electromagnetic environments and controlled dissipation are powerful resources for quantum electrodynamics. By engineering the spectral and spatial properties of the environment, it is possible to modify both the coherent and incoherent components of light–matter interactions. This level of control enables the realization of atom–photon bound states, the observation of collective nonlinear phenomena, and the implementation of selective and Purcell-protected decay channels. Together, these findings advance our understanding of open quantum systems and demonstrate practical strategies for controlling environmental effects in quantum technologies.

6.1 Outlook

The work presented here opens several promising directions:

The controlled formation and quenching of atom—photon bound states can be extended to explore more complex regimes, including directional emission, strongly correlated multi-emitter configurations, and the manifestation of non-Markovian dynamics in structured reservoirs. These extensions would deepen our understanding of light-matter interactions.

The slow, multimode transition and emission observed in the driven nonlinear metamaterial suggest the presence of collectivity at the Bose-Hubbard metamaterial, which is left for further studies. Beyond fundamental interest, this transition can be used for quantum metrology and quantum sensing.

The demonstrated control of selective decay and Purcell-protected readout offers a modular approach to building large-scale quantum systems with engineered connectivity and dissipation. Future efforts should aim to increase readout fidelity while maintaining high speed. A natural next step is to target a coupling regime $\kappa/2\chi=1$, and further detune the readout and the qubit frequencies to suppress cross-coupling.

The engineered decay pathways and controllable photon emission in coupledwaveguide systems could be exploited for energy-conversion experiments, quantum sensors, and fundamental tests of fluctuation theorems in quantum thermodynamics.

Ultimately, the results of this thesis demonstrate that dissipation is not merely a source of decoherence but a powerful design element in quantum engineering. By mastering the structure of the electromagnetic environment, we gain new means to manipulate, protect, and harness quantum information, paving the way toward a more robust and scalable quantum technology.

Part IV Appendix

Chapter 7

Methods

7.1 Introduction

In this chapter, we describe the experimental methods used to fabricate and measure our devices. The chapter is organized as follows. Section 7.2 presents the low-temperature setup, which enables control over the excitations in our devices. Section 7.3 details the room-temperature connections required for device measurements. Finally, Section 7.4 outlines the fabrication process.

7.2 Low-temperature setup

Superconducting quantum devices require cryogenic temperatures to maintain superconductivity and minimize thermal excitations. Superconductivity ensures minimal dissipative losses (zero electrical resistance) and enables the proper behavior of Josephson Junctions (JJs) through the formation of Cooper pairs. Minimizing thermal excitations is crucial for keeping the system in its ground state, allowing precise control.

In our samples, we use aluminium as the superconducting material, which becomes superconducting at temperatures below 1.2 K. To reduce thermal excitations, the resonant energy of our resonators must be significantly greater than the system's thermal energy, following the condition $\hbar\omega \gg k_BT$. In this expression, \hbar is the reduced Planck's constant, ω is the angular frequency, k_B is the Boltzmann's constant, and T is the temperature. For example, to keep a readout resonator at 5 GHz with less than 1 % thermal population, the temperature must be below roughly 50 mK.

Such low temperatures are achieved with a dilution refrigerator, which includes different cooling stages, each thermally shielded. At their last stage, the temperature is below 10 mK by exploiting the properties of a mixture of helium-3 / helium-4 (He-3/He-4). At very low temperatures, the mixture separates into two phases: A He-3 concentrated phase and a He-3 diluted phase. He-3 atoms moving from the concentrated to the diluted phase require energy, which is drawn from the system, effectively cooling it.

In addition, to protect our devices from electromagnetic interference, we use RF-tight copper shields, and from static magnetic fields, we use two Cryoperm shields and a superconducting shield. We use coaxial cables to transmit signals to and from the samples. The low-temperature experimental setup is shown in Fig. 7.1.

Our wiring setup consists of three distinct types of lines, each serving a specific function: input-output lines, charge lines, and flux lines. Input-output lines are connected to the transmission line coupled to one (or more) resonator(s) and serve to characterize both the resonator(s) and qubits. We drive the qubits with the charge lines and apply current to the flux lines to change the tunable-qubits' frequencies. Our input signals pass through multiple attenuation stages to minimize thermal noise. Additionally, we use 0 dBm attenuators as thermal anchoring points to dissipate heat along the coaxial cables. Stray radiation at frequencies outside the desired band is suppressed using filters. On the output line, signals from the device are amplified by a low-noise cryogenic amplifier based on a high-electron-mobility transistor (HEMT). To prevent unwanted signal and noise from propagating back to the sample, isolators and low-pass filters are strategically placed, to prevent unwanted effects on the device.

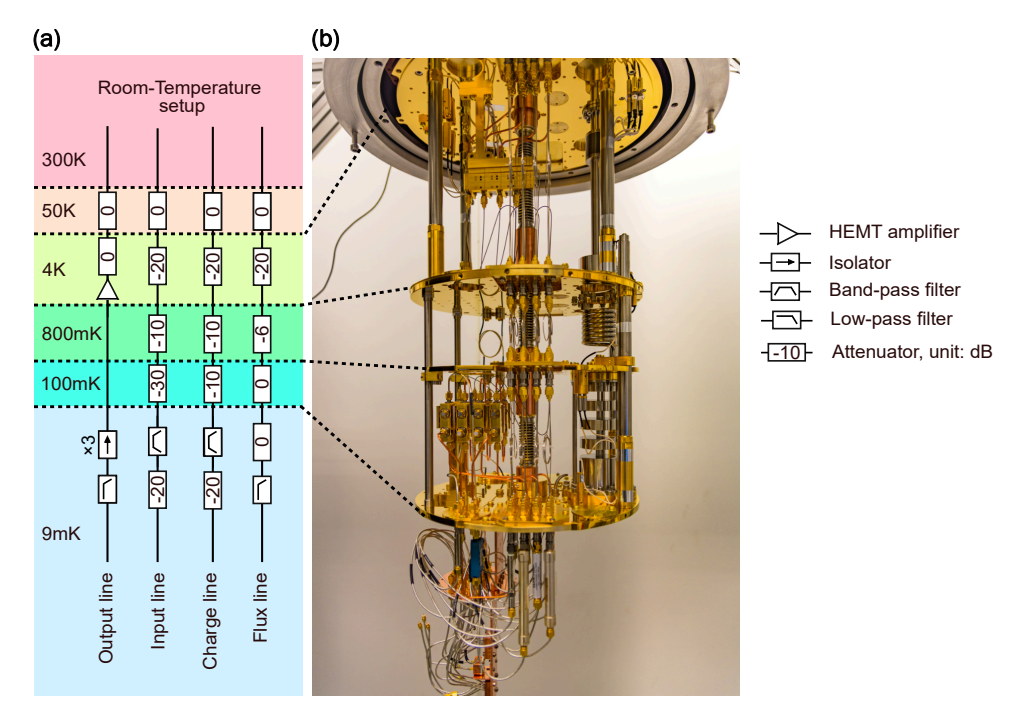


Figure 7.1: **Cryo-setup.** (a) Example of a standard wiring diagram in the dilution refrigerator for measurements done in transmission. Cooling stages are colored from room temperature, in red, to 9 mK, in blue. (b) Image of the cryo-setup, showing the different cooling stages and electrical components. At the lowest stage is the connected device.

7.3 Room-temperature setup

To characterize and perform the desired measurements on our samples, we perform two main different sets of measurements, each requiring different equipments.

For continuous wave (CW) spectroscopy measurements, we use a vector network analyzer (VNA) along with one or more local oscillators (LOs) and a source measure unit (SMU). The VNA is used to extract the scattering parameters of our system. Since our devices are measured in transmission (with separate input and output ports), we specifically extract the S_{21} parameter. The scattering parameters provide information about the resonant frequencies of our resonators. The LO is used to drive an extra element, such as the resonators in Paper 2, while the SMU supplies current to the flux lines [Fig. 7.2(a)].

For time-domain measurements, whether involving pulsed signals (as in Paper 1 and Paper 3) or analyzing the time response to a continuous drive (as in Paper 2), we track the time-dependent response of our system. A standard setup requires an arbitrary wave generator (AWG) to synthesize pulses with a carrier frequency of a few hundred MHz. These pulses are up-converted to the target frequency using an analog mixer and a LO source. Finally, they are routed to the device via the coaxial cables inside the dilution refrigerator. After interacting with the sample, the output signal is down-converted using another analog mixer and the same LO source frequency as for the up-conversion. Then, the analog signal is digitized.

An alternative approach is to use an equipment that integrates the AWG, LO, and mixers and digitally up- and down-converts the signal. In our case, we used a microwave transceiver, *Presto* from *Intermodulation Products*. The main advantage of this setup over the first one is that the mixing does not produce spurious tones, as is the case with analog mixers. However, the digital output is limited to 1 V. Therefore, in our case, we required an extra SMU or AWG with a larger voltage range to drive our flux lines [Fig. 7.2(b)].

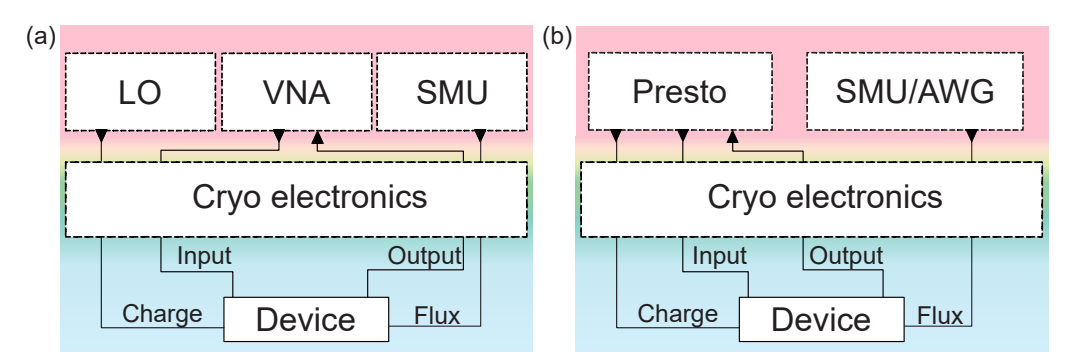


Figure 7.2: Standard room-temperature setup. The device includes input and output ports, a charge line, and a flux line. Color-coded: Temperature. (a) Setup when doing continuous wave or spectroscopy measurements. VNA is used to track the response of the device, charge line to excite the qubit with a LO and flux line to change its frequency with an applied current through an SMU. (b) Setup for time domain measurements.

7.4. Fabrication

7.4 Fabrication

Our devices, made out of aluminum on silicon, are fabricated inside a class 100 cleanroom, MyFab Chalmers. This environment ensures minimal contaminants and particle presence, required for fabricating high-coherence qubits.

The fabrication process consists of four lithographic steps for: The ground plane, the Josephson junctions, the patches and the air bridges.

7.4.1 Ground plane

Before fabricating the ground plane, the sample undergoes a cleaning process. This involves an SC1 clean followed by a one-minute HF dip to remove the native oxide layer. To minimize oxide regrowth, the sample is immediately loaded into a high-vacuum chamber. In the same chamber, an aluminum layer is deposited under ultra-high vacuum using evaporation, a physical vapor deposition (PVD) technique. Because the development is carried out using MF312, which etches the aluminum, a two-layer photoresist stack is spin-coated. The first layer, PMMA A2, is the aluminum-protective barrier. The second layer, S1805, undergoes photolithography. The exposed regions are then ashed to remove the S1805 layer, and the aluminum is wet etched in Transene.

7.4.2 Josephson junctions

The second lithography step is dedicated to the fabrication of the Josephson junctions. The JJ sizes in our lab range from 100 nm to 2.5 μ m. These small sizes, way below the resolution limit of the photolithography, require the use of electron-beam lithography (EBL). In addition, a lift-off step is done instead of an etching step to avoid damaging the already deposited aluminum. Our junctions are bridge-less Manhattan style [172–175], and as so, they require a thick resist stack to guarantee a good shadowing between deposition steps. The stack is composed of EL12 and PMMA A6. Once the resist is exposed in the EBL and developed in MIBK:IPA, two angled depositions are made with 50 and 110 nm thicknesses and an oxidation step in between. Then, the layer is lifted-off in a resist remover, in our case, remover 1165.

7.4.3 Patches

The third lithography step corresponds to the deposition of patches that connect the Josephson junctions to both the transmon and the ground plane. To avoid any damage to the ground plane or josephson junctions, this step again relies on a lift-off process. The same resist stack is used as in the previous step and previous to the deposition, the native oxide of the previous deposited aluminium layers is removed with an ion argon milling.

7.4.4 Air-bridges

The final lithography step consists of adding air-bridges, which are metallic bridges that connect separated ground planes across the device. Although all grounds are nominally at the same potential, at high frequencies, parasitic inductance, finite conductivity, and geometric separation can lead to non-negligible voltage differences between ground regions. These differences give rise to electric fields across the ground slot, which can support the propagation of unwanted slotline modes.

To fabricate the air-bridges, we perform a lithography step similar to that one in [176]. We spin-coat SPR220 resist and do the lithography of the base layer of the airbridge. After a reflow step, the edges of our resist become less stiff. We deposit aluminum through the whole wafer area and, with a second lithographic step of AZ1512, we develop all the wafer region except for the second air-bridge region. Then, this area is etched.

- [1] S. Haroche and J.-M. Raimond. *Exploring the Quantum: Atoms, Cavities, and Photons*. 1st. New York, USA: Oxford University Press, 2006 (cit. on p. 3).
- [2] J. M. Raimond, M. Brune, and S. Haroche. "Manipulating quantum entanglement with atoms and photons in a cavity". In: *Rev. Mod. Phys.* 73, Publisher: American Physical Society, pp. 565–582 (cit. on p. 3).
- [3] A. Blais, R.-S. Huang, A. Wallraff, S. M. Girvin, and R. J. Schoelkopf. "Cavity quantum electrodynamics for superconducting electrical circuits: An architecture for quantum computation". In: *Phys. Rev. A.* 69, Publisher: American Physical Society, p. 062320 (cit. on pp. 3, 7).
- [4] A. Wallraff, D. I. Schuster, A. Blais, L. Frunzio, R.-S. Huang, J. Majer, S. Kumar, S. M. Girvin, and R. J. Schoelkopf. "Strong coupling of a single photon to a superconducting qubit using circuit quantum electrodynamics". In: *Nature*. 431, pp. 162–167 (cit. on p. 3).
- [5] A. Blais, A. L. Grimsmo, S. M. Girvin, and A. Wallraff. "Circuit quantum electrodynamics". In: *Reviews of Modern Physics*. 93, Publisher: American Physical Society, p. 025005 (cit. on pp. 3, 8, 9, 23, 26, 29).
- [6] A. A. Houck, H. E. Türeci, and J. Koch. "On-chip quantum simulation with superconducting circuits". In: *Nat. Phys.* 8, Publisher: Nature Publishing Group, pp. 292–299. ISSN: 1745-2473 (cit. on p. 3).
- [7] M. Fitzpatrick, N. M. Sundaresan, A. C. Li, J. Koch, and A. A. Houck. "Observation of a Dissipative Phase Transition in a One-Dimensional Circuit QED Lattice". In: *Physical Review X.* 7, Publisher: American Physical Society (APS), p. 011016. ISSN: 2160-3308 (cit. on pp. 3, 49).
- [8] D. L. Underwood, W. E. Shanks, J. Koch, and A. A. Houck. "Low-disorder microwave cavity lattices for quantum simulation with photons". In: *Phys. Rev. A.* 86, Publisher: American Physical Society, p. 023837 (cit. on p. 3).
- [9] X. Gu, A. F. Kockum, A. Miranowicz, Y.-x. Liu, and F. Nori. "Microwave photonics with superconducting quantum circuits". In: *Physics Reports.* 718-719, pp. 1–102. ISSN: 0370-1573 (cit. on pp. 3, 9, 18).

[10] O. Astafiev, A. M. Zagoskin, A. A. Abdumalikov Jr., Y. A. Pashkin, T. Yamamoto, K. Inomata, Y. Nakamura, and J. S. Tsai. "Resonance Fluorescence of a Single Artificial Atom". In: *Science*. 327, pp. 840–843 (cit. on pp. 3, 19, 22, 30).

- [11] P. Forn-Diaz, C. W. Warren, C. W. S. Chang, A. M. Vadiraj, and C. M. Wilson. "On-Demand Microwave Generator of Shaped Single Photons". In: *Phys. Rev. Applied.* 8, Publisher: American Physical Society, p. 054015 (cit. on p. 3).
- [12] M. Mirhosseini, E. Kim, V. S. Ferreira, M. Kalaee, A. Sipahigil, A. J. Keller, and O. Painter. "Superconducting metamaterials for waveguide quantum electrodynamics". In: *Nat. Comm.* 9, p. 3706 (cit. on pp. 3, 8, 33).
- [13] I. Carusotto and C. Ciuti. "Quantum fluids of light". In: *Rev. Mod. Phys.* 85, Publisher: American Physical Society, pp. 299–366 (cit. on p. 3).
- [14] M. J. Hartmann. "Quantum Simulation with Interacting Photons". In: arXiv:1605.00383 [cond-mat, physics:physics, physics:quant-ph], (cit. on p. 3).
- [15] T. Roy, S. Kundu, M. Chand, S. Hazra, N. Nehra, R. Cosmic, A. Ranadive, M. P. Patankar, K. Damle, and R. Vijay. "Implementation of Pairwise Longitudinal Coupling in a Three-Qubit Superconducting Circuit". In: *Phys. Rev. Applied.* 7, Publisher: American Physical Society, p. 054025 (cit. on pp. 3, 23).
- [16] P. Lodahl, S. Mahmoodian, S. Stobbe, A. Rauschenbeutel, P. Schneeweiss, J. Volz, H. Pichler, and P. Zoller. "Chiral quantum optics". In: *Nature*. 541, pp. 473–480 (cit. on p. 3).
- [17] I.-C. Hoi, C. M. Wilson, G. Johansson, J. Lindkvist, B. Peropadre, T. Palomaki, and P. Delsing. "Microwave quantum optics with an artificial atom in one-dimensional open space". en. In: *New Journal of Physics*. 15, Publisher: IOP Publishing, p. 025011. ISSN: 1367-2630 (cit. on pp. 3, 19, 30).
- [18] N. M. Sundaresan, R. Lundgren, G. Zhu, A. V. Gorshkov, and A. A. Houck. "Interacting Qubit-Photon Bound States with Superconducting Circuits". In: *Phys. Rev. X.* 9, Publisher: American Physical Society, p. 011021 (cit. on pp. 3, 33, 34, 37).
- [19] M. Scigliuzzo, G. Calajò, F. Ciccarello, D. Perez Lozano, A. Bengtsson, P. Scarlino, A. Wallraff, D. Chang, P. Delsing, and S. Gasparinetti. "Controlling Atom-Photon Bound States in an Array of Josephson-Junction Resonators". In: *Physical Review X*. 12, Publisher: American Physical Society, p. 031036 (cit. on pp. 3, 33, 34, 36, 37).
- [20] R. G. DeVoe and R. G. Brewer. "Observation of Superradiant and Subradiant Spontaneous Emission of Two Trapped Ions". In: *Phys. Rev. Lett.* 76, Publisher: American Physical Society, pp. 2049–2052 (cit. on pp. 3, 18).
- [21] W. Guerin, M. O. Araujo, and R. Kaiser. "Subradiance in a Large Cloud of Cold Atoms". In: *Physical Review Letters*. 116, Publisher: American Physical Society (APS), p. 083601. ISSN: 1079-7114 (cit. on pp. 3, 18).

P. Solano, P. Barberis-Blostein, F. K. Fatemi, L. A. Orozco, and S. L. Rolston. "Super-radiance reveals infinite-range dipole interactions through a nanofiber". In: *Nature Communications*. 8, Number: 1 Publisher: Nature Publishing Group, p. 1857. ISSN: 2041-1723 (cit. on pp. 3, 18).

- [23] N. V. Corzo, J. Raskop, A. Chandra, A. S. Sheremet, B. Gouraud, and J. Laurat. "Waveguide-coupled single collective excitation of atomic arrays". In: *Nature*. 566, Number: 7744 Publisher: Nature Publishing Group, pp. 359–362. ISSN: 1476-4687 (cit. on pp. 3, 18).
- [24] K. Lalumière, B. C. Sanders, A. F. van Loo, A. Fedorov, A. Wallraff, and A. Blais. "Input-output theory for waveguide QED with an ensemble of inhomogeneous atoms". In: *Phys. Rev. A.* 88, Publisher: American Physical Society, p. 043806 (cit. on pp. 3, 18).
- [25] A. van Loo, A. Fedorov, K. Lalumière, B. Sanders, A. Blais, and A. Wallraff. "Photon-Mediated Interactions Between Distant Artificial Atoms". In: *Science*. 342, pp. 1494–1496 (cit. on pp. 3, 18).
- [26] M. Mirhosseini, E. Kim, X. Zhang, A. Sipahigil, P. B. Dieterle, A. J. Keller, A. Asenjo-Garcia, D. E. Chang, and O. Painter. "Cavity quantum electrodynamics with atom-like mirrors". In: *Nature*. 569, Publisher: Springer Science and Business Media LLC, p. 692 (cit. on pp. 3, 18).
- [27] S. J. Masson and A. Asenjo-Garcia. "Atomic-waveguide quantum electrodynamics". In: *Physical Review Research*. 2, Publisher: American Physical Society, p. 043213 (cit. on pp. 3, 18).
- [28] M. Zanner, T. Orell, C. M. F. Schneider, R. Albert, S. Oleschko, M. L. Juan, M. Silveri, and G. Kirchmair. "Coherent control of a multi-qubit dark state in waveguide quantum electrodynamics". In: *Nature Physics*, ISSN: 1745-2473, 1745-2481 (cit. on pp. 3, 18).
- [29] G. Andersson, B. Suri, L. Guo, T. Aref, and P. Delsing. "Non-exponential decay of a giant artificial atom". In: *Nature Physics*. 15, pp. 1123–1127. ISSN: 1745-2481 (cit. on p. 3).
- [30] V. S. Ferreira, J. Banker, A. Sipahigil, M. H. Matheny, A. J. Keller, E. Kim, M. Mirhosseini, and O. Painter. "Collapse and Revival of an Artificial Atom Coupled to a Structured Photonic Reservoir". In: *Physical Review X*. 11, Publisher: American Physical Society, p. 041043 (cit. on pp. 3, 33).
- [31] Y. Liu and A. A. Houck. "Quantum electrodynamics near a photonic bandgap". In: *Nature Physics.* 13, pp. 48–52. ISSN: 1745-2481 (cit. on pp. 3, 33).
- [32] J. D. Brehm, A. N. Poddubny, A. Stehli, T. Wolz, H. Rotzinger, and A. V. Ustinov. "Waveguide bandgap engineering with an array of superconducting qubits". In: *npj Quantum Materials*. 6, Number: 1 Publisher: Nature Publishing Group, pp. 1–5. ISSN: 2397-4648 (cit. on pp. 3, 33).
- [33] M. Pechal. "Microwave photonics in superconducting circuits". PhD Thesis. ETH Zurich, Aug. 2016 (cit. on p. 5).

[34] D. Gottesman, A. Kitaev, and J. Preskill. "Encoding a qubit in an oscillator". In: *Phys. Rev. A*. 64, Publisher: American Physical Society, p. 012310 (cit. on p. 7).

- [35] H. Wang et al. "Measurement of the Decay of Fock States in a Superconducting Quantum Circuit". In: *Physical Review Letters*. 101, Publisher: American Physical Society, p. 240401 (cit. on p. 7).
- [36] P. Krantz, M. Kjaergaard, F. Yan, T. P. Orlando, S. Gustavsson, and W. D. Oliver. "A quantum engineer's guide to superconducting qubits". en. In: *Applied Physics Reviews.* 6, p. 021318. ISSN: 1931-9401 (cit. on pp. 8, 9, 11, 13, 23).
- [37] A. Shearrow, G. Koolstra, S. J. Whiteley, N. Earnest, P. S. Barry, F. J. Heremans, D. D. Awschalom, E. Shirokoff, and D. I. Schuster. "Atomic layer deposition of titanium nitride for quantum circuits". In: *Applied Physics Letters*. 113, p. 212601. ISSN: 0003-6951 (cit. on p. 8).
- [38] S. Frasca, I. Arabadzhiev, S. B. de Puechredon, F. Oppliger, V. Jouanny, R. Musio, M. Scigliuzzo, F. Minganti, P. Scarlino, and E. Charbon. "NbN films with high kinetic inductance for high-quality compact superconducting resonators". In: *Physical Review Applied.* 20, Publisher: American Physical Society, p. 044021 (cit. on p. 8).
- [39] M. Peruzzo, F. Hassani, G. Szep, A. Trioni, E. Redchenko, M. Žemlička, and J. M. Fink. "Geometric Superinductance Qubits: Controlling Phase Delocalization across a Single Josephson Junction". en. In: *PRX Quantum.* 2, p. 040341. ISSN: 2691-3399 (cit. on p. 8).
- [40] E. Kim, X. Zhang, V. S. Ferreira, J. Banker, J. K. Iverson, A. Sipahigil, M. Bello, A. González-Tudela, M. Mirhosseini, and O. Painter. "Quantum Electrodynamics in a Topological Waveguide". In: *Physical Review X*. 11, Publisher: American Physical Society, p. 011015 (cit. on pp. 8, 33, 34, 37).
- [41] N. A. Masluk, I. M. Pop, A. Kamal, Z. K. Minev, and M. H. Devoret. "Microwave Characterization of Josephson Junction Arrays: Implementing a Low Loss Superinductance". In: *Physical Review Letters*. 109, Publisher: American Physical Society, p. 137002 (cit. on p. 8).
- [42] M. Pechal, J.-C. Besse, M. Mondal, M. Oppliger, S. Gasparinetti, and A. Wallraff. "Superconducting Switch for Fast On-Chip Routing of Quantum Microwave Fields". In: *Phys. Rev. Applied.* 6, p. 024009 (cit. on pp. 9, 24).
- [43] Y. Makhlin, G. Schön, and A. Shnirman. "Quantum-state engineering with Josephson-junction devices". en. In: *Reviews of Modern Physics*. 73, pp. 357–400. ISSN: 0034-6861, 1539-0756 (cit. on p. 9).
- [44] J. Koch, T. M. Yu, J. Gambetta, A. A. Houck, D. I. Schuster, J. Majer, A. Blais, M. H. Devoret, S. M. Girvin, and R. J. Schoelkopf. "Charge-insensitive qubit design derived from the Cooper pair box". In: *Phys. Rev. A*. 76, Publisher: APS, p. 042319 (cit. on p. 9).

[45] M. D. Hutchings, J. B. Hertzberg, Y. Liu, N. T. Bronn, G. A. Keefe, M. Brink, J. M. Chow, and B. L. T. Plourde. "Tunable Superconducting Qubits with Flux-Independent Coherence". In: *Physical Review Applied.* 8, p. 044003 (cit. on p. 10).

- [46] S. E. Nigg, H. Paik, B. Vlastakis, G. Kirchmair, S. Shankar, L. Frunzio, M. H. Devoret, R. J. Schoelkopf, and S. M. Girvin. "Black-Box Superconducting Circuit Quantization". In: *Phys. Rev. Lett.* 108, Publisher: American Physical Society, p. 240502 (cit. on p. 13).
- [47] M. F. Gely and G. A. Steele. "QuCAT: quantum circuit analyzer tool in Python". en. In: *New Journal of Physics*. 22, Publisher: IOP Publishing, p. 013025. ISSN: 1367-2630 (cit. on pp. 13, 14, 24).
- [48] A. Narla et al. "Robust Concurrent Remote Entanglement Between Two Superconducting Qubits". In: *Phys. Rev. X.* 6, Publisher: American Physical Society, p. 031036 (cit. on p. 17).
- [49] P. Kurpiers et al. "Deterministic quantum state transfer and remote entanglement using microwave photons". In: *Nature*. 558, pp. 264–267 (cit. on p. 17).
- [50] C. Axline et al. "On-demand quantum state transfer and entanglement between remote microwave cavity memories". In: *Nature Physics.* 14, pp. 705–710 (cit. on p. 17).
- [51] P. Campagne-Ibarcq et al. "Deterministic Remote Entanglement of Superconducting Circuits through Microwave Two-Photon Transitions". In: *Phys. Rev. Lett.* 120, Publisher: American Physical Society, p. 200501 (cit. on p. 17).
- [52] B. Kannan et al. "Generating spatially entangled itinerant photons with waveguide quantum electrodynamics". In: *Science Advances*. 6, eabb8780 (cit. on p. 17).
- [53] S. Sundelin, M. A. Aamir, V. M. Kulkarni, C. Castillo-Moreno, and S. Gasparinetti. *Quantum refrigeration powered by noise in a superconducting circuit.* arXiv:2403.03373 [quant-ph]. 2024 (cit. on p. 17).
- [54] A. S. Sheremet, M. I. Petrov, I. V. Iorsh, A. V. Poshakinskiy, and A. N. Poddubny. "Waveguide quantum electrodynamics: collective radiance and photon-photon correlations". In: arXiv:2103.06824 [physics, physics:quant-ph], arXiv: 2103.06824 (cit. on p. 18).
- [55] D. Roy, C. M. Wilson, and O. Firstenberg. "Colloquium: Strongly interacting photons in one-dimensional continuum". In: *Rev. Mod. Phys.* 89, Publisher: American Physical Society, p. 021001 (cit. on p. 18).
- [56] P. Lodahl, S. Mahmoodian, and S. Stobbe. "Interfacing single photons and single quantum dots with photonic nanostructures". In: *Rev. Mod. Phys.* 87, Publisher: American Physical Society, pp. 347–400 (cit. on p. 18).
- [57] E. Wiegand. "Quantum Optics and Waveguide Quantum Electrodynamics in Superconducting Circuits". en. PhD thesis (cit. on p. 18).

[58] K. Koshino and Y. Nakamura. "Control of the radiative level shift and linewidth of a superconducting artificial atom through a variable boundary condition". en. In: *New Journal of Physics*. 14, p. 043005. ISSN: 1367-2630 (cit. on p. 18).

- [59] Y. Lu et al. "Characterizing decoherence rates of a superconducting qubit by direct microwave scattering". In: *npj Quantum Information*. 7, Number: 1 Publisher: Nature Publishing Group, pp. 1–9. ISSN: 2056-6387 (cit. on pp. 18, 19, 30).
- [60] S. Filipp, M. Göppl, J. M. Fink, M. Baur, R. Bianchetti, L. Steffen, and A. Wallraff. "Multimode mediated qubit-qubit coupling and dark-state symmetries in circuit quantum electrodynamics". In: *Phys. Rev. A.* 83, Publisher: American Physical Society, p. 063827 (cit. on p. 20).
- [61] A. G. Fowler, M. Mariantoni, J. M. Martinis, and A. N. Cleland. "Surface codes: Towards practical large-scale quantum computation". In: *Phys. Rev. A*. 86, Publisher: American Physical Society, p. 032324 (cit. on p. 23).
- [62] Z. Chen et al. "Exponential suppression of bit or phase errors with cyclic error correction". en. In: *Nature*. 595, Publisher: Nature Publishing Group, pp. 383–387. ISSN: 1476-4687 (cit. on p. 23).
- [63] R. Acharya et al. "Suppressing quantum errors by scaling a surface code logical qubit". en. In: *Nature*. 614, Publisher: Nature Publishing Group, pp. 676–681. ISSN: 1476-4687 (cit. on p. 23).
- [64] S. Krinner et al. "Realizing repeated quantum error correction in a distance-three surface code". en. In: *Nature*. 605, Publisher: Nature Publishing Group, pp. 669–674. ISSN: 1476-4687 (cit. on p. 23).
- [65] M. D. Reed, B. R. Johnson, A. A. Houck, L. DiCarlo, J. M. Chow, D. I. Schuster, L. Frunzio, and R. J. Schoelkopf. "Fast reset and suppressing spontaneous emission of a superconducting qubit". In: Applied Physics Letters. 96, Publisher: American Institute of Physics, p. 203110. ISSN: 0003-6951 (cit. on p. 23).
- [66] J. M. Gambetta, A. A. Houck, and A. Blais. "Superconducting Qubit with Purcell Protection and Tunable Coupling". In: *Phys. Rev. Lett.* 106, Publisher: American Physical Society, p. 030502 (cit. on p. 23).
- [67] N. T. Bronn, Y. Liu, J. B. Hertzberg, A. D. Córcoles, A. A. Houck, J. M. Gambetta, and J. M. Chow. "Broadband filters for abatement of spontaneous emission in circuit quantum electrodynamics". In: *Applied Physics Letters*. 107, pp. (cit. on p. 23).
- [68] N. T. Bronn, E. Magesan, N. A. Masluk, J. M. Chow, J. M. Gambetta, and M. Steffen. "Reducing Spontaneous Emission in Circuit Quantum Electrodynamics by a Combined Readout/Filter Technique". In: *IEEE Transactions* on Applied Superconductivity. 25, Conference Name: IEEE Transactions on Applied Superconductivity, pp. 1–10. ISSN: 1558-2515 (cit. on p. 23).

[69] A. Y. Cleland, M. Pechal, P. C. Stas, C. J. Sarabalis, and A. H. Safavi-Naeini. "Mechanical Purcell Filters for Microwave Quantum Machines". In: *Applied Physics Letters*. 115, p. 263504 (cit. on p. 23).

- [70] J. Heinsoo et al. "Rapid High-fidelity Multiplexed Readout of Superconducting Qubits". In: *Phys. Rev. Applied.* 10, Publisher: American Physical Society, p. 034040 (cit. on p. 23).
- [71] A. A. Houck et al. "Controlling the Spontaneous Emission of a Superconducting Transmon Qubit". In: *Phys. Rev. Lett.* 101, Publisher: APS, p. 080502 (cit. on p. 23).
- [72] E. Jeffrey et al. "Fast Accurate State Measurement with Superconducting Qubits". In: *Phys. Rev. Lett.* 112, Publisher: American Physical Society, p. 190504 (cit. on p. 23).
- [73] S. H. Park, G. Choi, G. Kim, J. Jo, B. Lee, G. Kim, K. Park, Y.-H. Lee, and S. Hahn. "Characterization of broadband Purcell filters with compact footprint for fast multiplexed superconducting qubit readout". In: *Applied Physics Letters*. 124, p. 044003. ISSN: 0003-6951 (cit. on p. 23).
- [74] G. Kim, A. Butler, V. S. Ferreira, X. (Zhang, A. Hadley, E. Kim, and O. Painter. "Fast unconditional reset and leakage reduction of a tunable superconducting qubit via an engineered dissipative bath". In: *Physical Review Applied.* 24, Publisher: American Physical Society, p. 014013 (cit. on p. 23).
- [75] F. Swiadek et al. "Enhancing Dispersive Readout of Superconducting Qubits through Dynamic Control of the Dispersive Shift: Experiment and Theory". In: *PRX Quantum.* 5, Publisher: American Physical Society, p. 040326 (cit. on pp. 23, 29).
- [76] T. Walter et al. "Rapid, High-Fidelity, Single-Shot Dispersive Readout of Superconducting Qubits". In: *Phys. Rev. Applied.* 7, p. 054020 (cit. on p. 23).
- [77] Y. Sunada, S. Kono, J. Ilves, S. Tamate, T. Sugiyama, Y. Tabuchi, and Y. Nakamura. "Fast readout and reset of a superconducting qubit coupled to a resonator with an intrinsic Purcell filter". In: arXiv:2202.06202 [quant-ph], arXiv: 2202.06202 (cit. on pp. 23, 24, 31).
- [78] A. Yen et al. "Interferometric Purcell suppression of spontaneous emission in a superconducting qubit". In: *Physical Review Applied.* 23, Publisher: American Physical Society, p. 024068 (cit. on p. 23).
- [79] P. A. Spring, L. Milanovic, Y. Sunada, S. Wang, A. F. van Loo, S. Tamate, and Y. Nakamura. "Fast Multiplexed Superconducting-Qubit Readout with Intrinsic Purcell Filtering Using a Multiconductor Transmission Line". In: *PRX Quantum.* 6, Publisher: American Physical Society, p. 020345 (cit. on p. 23).
- [80] I. Diniz, E. Dumur, O. Buisson, and A. Auffèves. "Ultrafast quantum non-demolition measurements based on a diamond-shaped artificial atom". In: *Physical Review A*. 87, Publisher: American Physical Society, p. 033837 (cit. on p. 23).

[81] F. Pfeiffer et al. "Efficient Decoupling of a Nonlinear Qubit Mode from Its Environment". In: *Physical Review X.* 14, Publisher: American Physical Society, p. 041007 (cit. on p. 23).

- [82] S. Hazra, W. Dai, T. Connolly, P. D. Kurilovich, Z. Wang, L. Frunzio, and M. H. Devoret. "Benchmarking the Readout of a Superconducting Qubit for Repeated Measurements". In: *Physical Review Letters*. 134, Publisher: American Physical Society, p. 100601 (cit. on p. 23).
- [83] A. Sah, S. Kundu, H. Suominen, Q. Chen, and M. Möttönen. "Decay-protected superconducting qubit with fast control enabled by integrated on-chip filters". en. In: Communications Physics. 7, Publisher: Nature Publishing Group, p. 227. ISSN: 2399-3650 (cit. on p. 23).
- [84] J. Gambetta, A. Blais, M. Boissonneault, A. A. Houck, D. I. Schuster, and S. M. Girvin. "Quantum trajectory approach to circuit QED: Quantum jumps and the Zeno effect". In: *Phys. Rev. A.* 77, p. 012112 (cit. on pp. 24, 29).
- [85] D. I. Schuster, A. Wallraff, A. Blais, L. Frunzio, R.-S. Huang, J. Majer, S. M. Girvin, and R. J. Schoelkopf. "ac Stark Shift and Dephasing of a Superconducting Qubit Strongly Coupled to a Cavity Field". In: *Physical Review Letters*. 94, Publisher: American Physical Society, p. 123602 (cit. on p. 25).
- [86] C. Eichler and A. Wallraff. "Controlling the dynamic range of a Josephson parametric amplifier". en. In: *EPJ Quantum Technology*. 1, Number: 1 Publisher: SpringerOpen, pp. 1–19. ISSN: 2196-0763 (cit. on p. 26).
- [87] S. Probst, F. B. Song, P. A. Bushev, A. V. Ustinov, and M. Weides. "Efficient and robust analysis of complex scattering data under noise in microwave resonators". In: *Review of Scientific Instruments*. 86, p. 024706. ISSN: 0034-6748 (cit. on p. 26).
- [88] S. Krinner et al. "Realizing repeated quantum error correction in a distance-three surface code". en. In: *Nature*. 605, Number: 7911 Publisher: Nature Publishing Group, pp. 669–674. ISSN: 1476-4687 (cit. on p. 28).
- [89] Y. Zhao et al. "Realization of an Error-Correcting Surface Code with Super-conducting Qubits". In: *Physical Review Letters*. 129, Publisher: American Physical Society, p. 030501 (cit. on p. 28).
- [90] K. Geerlings, Z. Leghtas, I. M. Pop, S. Shankar, L. Frunzio, R. J. Schoelkopf, M. Mirrahimi, and M. H. Devoret. "Demonstrating a Driven Reset Protocol for a Superconducting Qubit". In: *Phys. Rev. Lett.* 110, Publisher: American Physical Society, p. 120501 (cit. on p. 29).
- [91] C. Macklin, K. O'Brien, D. Hover, M. E. Schwartz, V. Bolkhovsky, X. Zhang, W. D. Oliver, and I. Siddiqi. "A near-quantum-limited Josephson traveling-wave parametric amplifier". In: Science. 350, Publisher: American Association for the Advancement of Science, pp. 307–310 (cit. on p. 29).

[92] P. Magnard et al. "Fast and Unconditional All-Microwave Reset of a Super-conducting Qubit". In: *Phys. Rev. Lett.* 121, Publisher: American Physical Society, p. 060502 (cit. on p. 29).

- [93] M. O. Tholén et al. "Measurement and control of a superconducting quantum processor with a fully integrated radio-frequency system on a chip". In: *Review of Scientific Instruments*. 93, Publisher: American Institute of Physics, p. 104711. ISSN: 0034-6748 (cit. on p. 30).
- [94] I.-C. Hoi, A. F. Kockum, L. Tornberg, A. Pourkabirian, G. Johansson, P. Delsing, and C. M. Wilson. "Probing the quantum vacuum with an artificial atom in front of a mirror". In: *Nature Physics*. 11, Publisher: Nature Publishing Group, pp. 1045–1049. ISSN: 1745-2481 (cit. on p. 30).
- [95] M. Scigliuzzo, A. Bengtsson, J.-C. Besse, A. Wallraff, P. Delsing, and S. Gasparinetti. "Primary Thermometry of Propagating Microwaves in the Quantum Regime". In: *Physical Review X.* 10, Publisher: American Physical Society, p. 041054 (cit. on p. 30).
- [96] K. Kakuyanagi, T. Meno, S. Saito, H. Nakano, K. Semba, H. Takayanagi, F. Deppe, and A. Shnirman. "Dephasing of a superconducting flux qubit". In: *Phys. Rev. Lett.* 98, p. 047004 (cit. on p. 31).
- [97] J. S. Douglas, H. Habibian, C.-L. Hung, A. V. Gorshkov, H. J. Kimble, and D. E. Chang. "Quantum many-body models with cold atoms coupled to photonic crystals". In: *Nat Photon.* 9, Publisher: Nature Publishing Group, pp. 326–331. ISSN: 1749-4885 (cit. on pp. 33, 37).
- [98] González-Tudela, V. Paulisch, D. E. Chang, and J. I. Kimble H. J. and. Cirac. "Deterministic Generation of Arbitrary Photonic States Assisted by Dissipation". In: *Phys. Rev. Lett.* 115, p. 163603 (cit. on p. 33).
- [99] A. Biella, L. Mazza, I. Carusotto, D. Rossini, and R. Fazio. "Photon transport in a dissipative chain of nonlinear cavities". In: *Phys. Rev. A*. 91, Publisher: American Physical Society, p. 053815 (cit. on p. 33).
- [100] L. Lu, J. D. Joannopoulos, and M. Soljacic. "Topological states in photonic systems". In: *Nat Phys.* 12, Publisher: Nature Publishing Group, a division of Macmillan Publishers Limited. All Rights Reserved., pp. 626–629. ISSN: 1745-2473 (cit. on p. 33).
- [101] G. Calajó, F. Ciccarello, D. Chang, and P. Rabl. "Atom-field dressed states in slow-light waveguide QED". In: *Phys. Rev. A.* 93, Publisher: American Physical Society, p. 033833 (cit. on pp. 33, 37, 38).
- [102] V. M. Martinez Alvarez and M. D. Coutinho-Filho. "Edge states in trimer lattices". In: *Phys. Rev. A.* 99, Publisher: American Physical Society, p. 013833 (cit. on p. 33).
- [103] R. Belyansky, S. Whitsitt, R. Lundgren, Y. Wang, A. Vrajitoarea, A. A. Houck, and A. V. Gorshkov. "Frustration-induced anomalous transport and strong photon decay in waveguide QED". In: *Physical Review Research.* 3, Publisher: American Physical Society, p. L032058 (cit. on p. 33).

[104] G. P. Fedorov et al. "Photon Transport in a Bose-Hubbard Chain of Superconducting Artificial Atoms". In: *Physical Review Letters*. 126, Publisher: American Physical Society, p. 180503 (cit. on p. 33).

- [105] F. Ciccarello. "Resonant atom-field interaction in large-size coupled-cavity arrays". en. In: *Physical Review A*. 83, p. 043802. ISSN: 1050-2947, 1094-1622 (cit. on p. 33).
- [106] A. S. Sheremet, M. I. Petrov, I. V. Iorsh, A. V. Poshakinskiy, and A. N. Poddubny. "Waveguide quantum electrodynamics: Collective radiance and photon-photon correlations". In: *Reviews of Modern Physics*. 95, Publisher: American Physical Society, p. 015002 (cit. on p. 33).
- [107] D. Fernández-Fernández and A. González-Tudela. "Tunable Directional Emission and Collective Dissipation with Quantum Metasurfaces". In: *Physical Review Letters*. 128, Publisher: American Physical Society, p. 113601 (cit. on p. 33).
- [108] J. Romn-Roche, E. Snchez-Burillo, and D. Zueco. "Bound states in ultrastrong waveguide QED". In: *arXiv:2001.07643*, (cit. on p. 33).
- [109] G. Calajó, Y.-L. L. Fang, H. U. Baranger, and F. Ciccarello. "Exciting a Bound State in the Continuum through Multiphoton Scattering Plus Delayed Quantum Feedback". In: *Phys. Rev. Lett.* 122, Publisher: American Physical Society, p. 073601 (cit. on p. 33).
- [110] C.-L. Hung, A. González-Tudela, J. I. Cirac, and H. J. Kimble. "Quantum spin dynamics with pairwise-tunable, long-range interactions". In: *Proceedings of the National Academy of Sciences*. 113, _eprint: http://www.pnas.org/content/113/34/E4946.full. E4946–E4955 (cit. on p. 33).
- [111] D. E. Chang, J. S. Douglas, A. González-Tudela, C.-L. Hung, and H. J. Kimble. "Colloquium: Quantum matter built from nanoscopic lattices of atoms and photons". en. In: Reviews of Modern Physics. 90, p. 031002. ISSN: 0034-6861, 1539-0756 (cit. on p. 33).
- [112] C. D. Bruzewicz, J. Chiaverini, R. McConnell, and J. M. Sage. "Trapped-Ion Quantum Computing: Progress and Challenges". In: arXiv:1904.04178, (cit. on p. 33).
- [113] A. McDonald, T. Pereg-Barnea, and A. A. Clerk. "Phase-Dependent Chiral Transport and Effective Non-Hermitian Dynamics in a Bosonic Kitaev-Majorana Chain". In: *Physical Review X.* 8, Publisher: American Physical Society, p. 041031 (cit. on p. 33).
- [114] T. Manovitz, Y. Shapira, N. Akerman, A. Stern, and R. Ozeri. "Quantum Simulations with Complex Geometries and Synthetic Gauge Fields in a Trapped Ion Chain". In: *PRX Quantum*. 1, Publisher: American Physical Society, p. 020303 (cit. on p. 33).

[115] M. K. Joshi, A. Elben, B. Vermersch, T. Brydges, C. Maier, P. Zoller, R. Blatt, and C. F. Roos. "Quantum information scrambling in a trapped-ion quantum simulator with tunable range interactions". In: arXiv:2001.02176, (cit. on p. 33).

- [116] I. Carusotto, A. A. Houck, A. J. Kollár, P. Roushan, D. I. Schuster, and J. Simon. "Photonic materials in circuit quantum electrodynamics". en. In: *Nature Physics*. 16, Number: 3 Publisher: Nature Publishing Group, pp. 268–279. ISSN: 1745-2481 (cit. on p. 33).
- [117] A. Vrajitoarea, R. Belyansky, R. Lundgren, S. Whitsitt, A. V. Gorshkov, and A. A. Houck. *Ultrastrong light-matter interaction in a multimode photonic crystal.* arXiv:2209.14972 [cond-mat, physics:quant-ph]. Feb. 2024 (cit. on p. 33).
- [118] A. Morvan et al. "Formation of robust bound states of interacting microwave photons". en. In: *Nature*. 612, Number: 7939 Publisher: Nature Publishing Group, pp. 240–245. ISSN: 1476-4687 (cit. on p. 33).
- [119] M. Bello, G. Platero, and A. González-Tudela. "Spin Many-Body Phases in Standard- and Topological-Waveguide QED Simulators". en. In: *PRX Quantum.* 3, p. 010336. ISSN: 2691-3399 (cit. on p. 33).
- [120] X. Zhang, E. Kim, D. K. Mark, S. Choi, and O. Painter. "A scalable superconducting quantum simulator with long-range connectivity based on a photonic bandgap metamaterial". In: *Science*. 379, arXiv:2206.12803 [quant-ph], pp. 278–283. ISSN: 0036-8075, 1095-9203 (cit. on pp. 33, 34, 37).
- [121] C. Tabares, A. Muñoz de las Heras, L. Tagliacozzo, D. Porras, and A. González-Tudela. "Variational Quantum Simulators Based on Waveguide QED". In: *Physical Review Letters.* 131, Publisher: American Physical Society, p. 073602 (cit. on p. 33).
- [122] T. McBroom-Carroll, A. Schlabes, X. Xu, J. Ku, B. Cole, S. Indrajeet, M. D. LaHaye, M. H. Ansari, and B. L. T. Plourde. *Entangling interactions between artificial atoms mediated by a multimode left-handed superconducting ring resonator*. arXiv:2307.15695 [cond-mat, physics:quant-ph]. July 2023 (cit. on p. 33).
- [123] V. S. Ferreira, G. Kim, A. Butler, H. Pichler, and O. Painter. "Deterministic generation of multidimensional photonic cluster states with a single quantum emitter". en. In: *Nature Physics*, Publisher: Nature Publishing Group, pp. 1–6. ISSN: 1745-2481 (cit. on p. 33).
- [124] V. D. Vaidya, Y. Guo, R. M. Kroeze, K. E. Ballantine, A. J. Kollár, J. Keeling, and B. L. Lev. "Tunable-Range, Photon-Mediated Atomic Interactions in Multimode Cavity QED". In: *Physical Review X.* 8, Publisher: American Physical Society, p. 011002 (cit. on p. 33).
- [125] A. J. Kollár, M. Fitzpatrick, P. Sarnak, and A. A. Houck. "Line-Graph Lattices: Euclidean and Non-Euclidean Flat Bands, and Implementations in Circuit Quantum Electrodynamics". In: arXiv:1902.02794, (cit. on p. 34).

[126] A. V. Shytov. "Landau-Zener transitions in a multilevel system: An exact result". In: *Physical Review A*. 70, Publisher: American Physical Society, p. 052708 (cit. on p. 42).

- [127] M. Wubs, K. Saito, S. Kohler, P. Hänggi, and Y. Kayanuma. "Gauging a Quantum Heat Bath with Dissipative Landau-Zener Transitions". en. In: *Physical Review Letters*. 97, p. 200404. ISSN: 0031-9007, 1079-7114 (cit. on p. 42).
- [128] K. Saito, M. Wubs, S. Kohler, Y. Kayanuma, and P. Hänggi. "Dissipative Landau-Zener transitions of a qubit: Bath-specific and universal behavior". en. In: *Physical Review B.* 75, p. 214308. ISSN: 1098-0121, 1550-235X (cit. on p. 42).
- [129] A. Stehli, J. D. Brehm, T. Wolz, A. Schneider, H. Rotzinger, M. Weides, and A. V. Ustinov. "Quantum emulation of the transient dynamics in the multistate Landau-Zener model". en. In: *npj Quantum Information*. 9, Number: 1 Publisher: Nature Publishing Group, pp. 1–5. ISSN: 2056-6387 (cit. on p. 42).
- [130] M. A. Rol et al. "Fast, High-Fidelity Conditional-Phase Gate Exploiting Leakage Interference in Weakly Anharmonic Superconducting Qubits". In: *Phys. Rev. Lett.* 123, Publisher: American Physical Society, p. 120502 (cit. on p. 46).
- [131] M. A. Rol, L. Ciorciaro, F. K. Malinowski, B. M. Tarasinski, R. E. Sagastizabal, C. C. Bultink, Y. Salathe, N. Haandbaek, J. Sedivy, and L. DiCarlo. "Timedomain characterization and correction of on-chip distortion of control pulses in a quantum processor". In: *Appl. Phys. Lett.*, (cit. on p. 46).
- [132] H. Risken, C. Savage, F. Haake, and D. F. Walls. "Quantum tunneling in dispersive optical bistability". In: *Physical Review A*. 35, Publisher: American Physical Society, pp. 1729–1739 (cit. on pp. 49, 60).
- [133] O. V. Zhirov and D. L. Shepelyansky. "Synchronization and Bistability of a Qubit Coupled to a Driven Dissipative Oscillator". In: *Physical Review Letters*. 100, Publisher: American Physical Society, p. 014101 (cit. on p. 49).
- [134] K. C. Stitely, S. J. Masson, A. Giraldo, B. Krauskopf, and S. Parkins. "Superradiant switching, quantum hysteresis, and oscillations in a generalized Dicke model". In: *Physical Review A*. 102, Publisher: American Physical Society, p. 063702 (cit. on p. 49).
- [135] F. Caleffi, M. Capone, and I. Carusotto. "Collective Excitations of a Strongly Correlated Nonequilibrium Photon Fluid across the Insulator-Superfluid Phase Transition". In: *Physical Review Letters*. 131, Publisher: American Physical Society, p. 193604 (cit. on p. 49).
- [136] F. Minganti, A. Biella, N. Bartolo, and C. Ciuti. "Spectral theory of Liouvillians for dissipative phase transitions". en. In: *Physical Review A*. 98, p. 042118. ISSN: 2469-9926, 2469-9934 (cit. on pp. 49–51).

[137] W. H. Zurek, U. Dorner, and P. Zoller. "Dynamics of a Quantum Phase Transition". In: *Physical Review Letters*. 95, Publisher: American Physical Society, p. 105701 (cit. on p. 49).

- [138] F. Minganti, I. I. Arkhipov, A. Miranowicz, and F. Nori. "Liouvillian spectral collapse in the Scully-Lamb laser model". In: *Physical Review Research.* 3, Publisher: American Physical Society, p. 043197 (cit. on p. 49).
- [139] F. Minganti, V. Savona, and A. Biella. "Dissipative phase transitions in \$n\$-photon driven quantum nonlinear resonators". en-GB. In: Quantum.
 7, Publisher: Verein zur Förderung des Open Access Publizierens in den Quantenwissenschaften, p. 1170 (cit. on p. 49).
- [140] D. Goncalves, L. Bombieri, G. Ferioli, S. Pancaldi, I. Ferrier-Barbut, A. Browaeys, E. Shahmoon, and D. Chang. "Driven-Dissipative Phase Separation in Free-Space Atomic Ensembles". In: *PRX Quantum*. 6, Publisher: American Physical Society, p. 020303 (cit. on p. 49).
- [141] M. Soriente, T. Donner, R. Chitra, and O. Zilberberg. "Dissipation-Induced Anomalous Multicritical Phenomena". In: *Physical Review Letters*. 120, Publisher: American Physical Society, p. 183603 (cit. on p. 49).
- [142] M. Soriente, T. L. Heugel, K. Omiya, R. Chitra, and O. Zilberberg. "Distinctive class of dissipation-induced phase transitions and their universal characteristics". In: *Physical Review Research*. 3, Publisher: American Physical Society, p. 023100 (cit. on p. 49).
- [143] L. Pausch, F. Damanet, T. Bastin, and J. Martin. "Dissipative phase transition: From qubits to qudits". en. In: *Physical Review A*. 110, p. 062208. ISSN: 2469-9926, 2469-9934 (cit. on p. 49).
- [144] K. Baumann, G. Guerlin, F. Brennecke, and T. Esslinger. "The Dicke Quantum Phase Transition in a Superfluid Gas Coupled to an Optical Cavity". In: *Nature*. 464, p. 1301 (cit. on p. 49).
- [145] M. Greiner, O. Mandel, T. Esslinger, T. W. Hansch, and I. Bloch. "Quantum phase transition from a superfluid to a Mott insulator in a gas of ultracold atoms". In: *Nature*. 415, pp. 39–44. ISSN: 0028-0836 (cit. on p. 49).
- [146] F. Ferri, R. Rosa-Medina, F. Finger, N. Dogra, M. Soriente, O. Zilberberg, T. Donner, and T. Esslinger. "Emerging Dissipative Phases in a Superradiant Quantum Gas with Tunable Decay". In: *Physical Review X*. 11, Publisher: American Physical Society, p. 041046 (cit. on p. 49).
- [147] R. Labouvie, B. Santra, S. Heun, and H. Ott. "Bistability in a Driven-Dissipative Superfluid". In: *Physical Review Letters*. 116, Publisher: American Physical Society, p. 235302 (cit. on p. 49).
- [148] J. Schliemann, A. Khaetskii, and D. Loss. "Electron spin dynamics in quantum dots and related nanostructures due to hyperfine interaction with nuclei". en. In: *Journal of Physics: Condensed Matter.* 15, R1809. ISSN: 0953-8984 (cit. on p. 49).

[149] A. Russell, V. I. Fal'ko, A. I. Tartakovskii, and M. S. Skolnick. "Bistability of optically induced nuclear spin orientation in quantum dots". In: *Physical Review B*. 76, Publisher: American Physical Society, p. 195310 (cit. on p. 49).

- [150] O. Krebs, P. Maletinsky, T. Amand, B. Urbaszek, A. Lemaître, P. Voisin, X. Marie, and A. Imamoglu. "Anomalous Hanle Effect due to Optically Created Transverse Overhauser Field in Single \$\mathrm{InAs}/\mathrm{GaAs}\$ Quantum Dots". In: *Physical Review Letters*. 104, Publisher: American Physical Society, p. 056603 (cit. on p. 49).
- [151] E. M. Kessler, G. Giedke, A. Imamoglu, S. F. Yelin, M. D. Lukin, and J. I. Cirac. "Dissipative phase transition in a central spin system". en. In: *Physical Review A*. 86, p. 012116. ISSN: 1050-2947, 1094-1622 (cit. on p. 49).
- [152] I. Siddiqi et al. "Direct observation of dynamical bifurcation between two driven oscillation states of a Josephson junction". In: *Phys. Rev. Lett.* 94, Place: ONE PHYSICS ELLIPSE, COLLEGE PK, MD 20740-3844 USA Publisher: AMERICAN PHYSICAL SOC Type: Article. ISSN: 0031-9007 (cit. on p. 49).
- [153] P. Krantz, Y. Reshitnyk, W. Wustmann, J. Bylander, S. Gustavsson, W. D. Oliver, T. Duty, V. Shumeiko, and P. Delsing. "Investigation of nonlinear effects in Josephson parametric oscillators used in circuit quantum electrodynamics". In: *New J. Phys.* 15, p. 105002 (cit. on p. 49).
- [154] T. Weißl, B. Küng, E. Dumur, A. K. Feofanov, I. Matei, C. Naud, O. Buisson, F. W. J. Hekking, and W. Guichard. "Kerr coefficients of plasma resonances in Josephson junction chains". In: *Phys. Rev. B.* 92, Publisher: American Physical Society, p. 104508 (cit. on p. 49).
- [155] J. M. Fink, A. Dombi, A. Vukics, A. Wallraff, and P. Domokos. "Observation of the photon-blockade breakdown phase transition". In: *Phys. Rev. X.* 7, p. 011012 (cit. on p. 49).
- [156] T. K. Mavrogordatos, G. Tancredi, M. Elliott, M. J. Peterer, A. Patterson, J. Rahamim, P. J. Leek, E. Ginossar, and M. H. Szymańska. "Simultaneous Bistability of a Qubit and Resonator in Circuit Quantum Electrodynamics". In: *Phys. Rev. Lett.* 118, Publisher: American Physical Society, p. 040402 (cit. on p. 49).
- [157] P. R. Muppalla, O. Gargiulo, S. I. Mirzaei, B. P. Venkatesh, M. L. Juan, L. Grünhaupt, I. M. Pop, and G. Kirchmair. "Bistability in a mesoscopic Josephson junction array resonator". In: *Phys. Rev. B.* 97, Publisher: American Physical Society, p. 024518 (cit. on pp. 49, 60).
- [158] Y. Chen, K. N. Nesterov, H. Churchill, J. Shabani, V. E. Manucharyan, and M. G. Vavilov. *Voltage Activated Parametric Entangling Gates on Gatemons*. arXiv:2304.08469 [cond-mat, physics:quant-ph]. Apr. 2023 (cit. on p. 49).

[159] R. Sett, F. Hassani, D. Phan, S. Barzanjeh, A. Vukics, and J. M. Fink. "Emergent Macroscopic Bistability Induced by a Single Superconducting Qubit". In: *PRX Quantum*. 5, Publisher: American Physical Society, p. 010327 (cit. on p. 49).

- [160] G. Beaulieu, F. Minganti, S. Frasca, V. Savona, S. Felicetti, R. Di Candia, and P. Scarlino. "Observation of first- and second-order dissipative phase transitions in a two-photon driven Kerr resonator". en. In: *Nature Communications*. 16, Publisher: Nature Publishing Group, p. 1954. ISSN: 2041-1723 (cit. on p. 49).
- [161] G. Beaulieu, F. Minganti, S. Frasca, M. Scigliuzzo, S. Felicetti, R. Di Candia, and P. Scarlino. "Criticality-Enhanced Quantum Sensing with a Parametric Superconducting Resonator". en. In: *PRX Quantum*. 6, p. 020301. ISSN: 2691-3399 (cit. on p. 49).
- [162] C. Berdou et al. "One Hundred Second Bit-Flip Time in a Two-Photon Dissipative Oscillator". In: *PRX Quantum.* 4, Publisher: American Physical Society, p. 020350 (cit. on pp. 49, 60).
- [163] P. Brookes, G. Tancredi, A. D. Patterson, J. Rahamim, M. Esposito, T. K. Mavrogordatos, P. J. Leek, E. Ginossar, and M. H. Szymanska. "Critical slowing down in circuit quantum electrodynamics". In: *Science Advances*. 7, Publisher: American Association for the Advancement of Science, eabe9492 (cit. on p. 49).
- [164] F. Vicentini, F. Minganti, R. Rota, G. Orso, and C. Ciuti. "Critical slowing down in driven-dissipative Bose-Hubbard lattices". en. In: *Physical Review A*. 97, p. 013853. ISSN: 2469-9926, 2469-9934 (cit. on p. 49).
- [165] C. Eichler and A. Wallraff. "Controlling the dynamic range of a Josephson parametric amplifier". In: *EPJ Quantum Technology*. 1, p. 2. ISSN: 2196-0763 (cit. on p. 52).
- [166] P. J. Koppinen, L. M. Vaisto, and I. J. Maasilta. "Complete stabilization and improvement of the characteristics of tunnel junctions by thermal annealing". In: *Appl. Phys. Lett.* 90, Publisher: AIP, pp. 053503–3 (cit. on p. 52).
- [167] P. D. Drummond and D. F. Walls. "Quantum theory of optical bistability. I. Nonlinear polarisability model". In: *Journal of Physics A: Mathematical and General.* 13, pp. 725–741 (cit. on p. 53).
- [168] D. Nigro. "On the uniqueness of the steady-state solution of the Lindblad–Gorini–Kossakowski–Sudarshan equation". en. In: *Journal of Statistical Mechanics: Theory and Experiment.* 2019, Publisher: IOP Publishing and SISSA, p. 043202. ISSN: 1742-5468 (cit. on p. 53).
- [169] T. Sépulcre. Analytical phase boundary of a quantum driven-dissipative Kerr oscillator from classical stochastic instantons. arXiv:2508.13925 [quant-ph]. Sept. 2025 (cit. on pp. 53, 59).

[170] Y. Zhang, J. C. Curtis, C. S. Wang, R. J. Schoelkopf, and S. M. Girvin. "Drive-induced nonlinearities of cavity modes coupled to a transmon ancilla". In: arXiv:2106.09112 [cond-mat, physics:quant-ph], arXiv: 2106.09112 (cit. on p. 57).

- [171] T. W. Anderson and D. A. Darling. "Asymptotic Theory of Certain "Goodness of Fit" Criteria Based on Stochastic Processes". In: *The Annals of Mathematical Statistics*. 23, Publisher: Institute of Mathematical Statistics, pp. 193–212. ISSN: 0003-4851, 2168-8990 (cit. on p. 59).
- [172] A. Potts, P. R. Routley, G. J. Parker, J. J. Baumberg, and P. A. J. de Groot. "Novel fabrication methods for submicrometer Josephson junction qubits". en. In: *Journal of Materials Science: Materials in Electronics*. 12, pp. 289–293. ISSN: 1573-482X (cit. on p. 74).
- [173] F. Lecocq, I. M. Pop, Z. Peng, I. Matei, T. Crozes, T. Fournier, C. Naud, W. Guichard, and O. Buisson. "Junction fabrication by shadow evaporation without a suspended bridge". In: *Nanotechnology*. 22, p. 315302 (cit. on p. 74).
- [174] K. Zhang, M.-M. Li, Q. Liu, H.-F. Yu, and Y. Yu. "Bridge-free fabrication process for Al/AlO x /Al Josephson junctions". en. In: *Chinese Physics B*. 26, Publisher: IOP Publishing, p. 078501. ISSN: 1674-1056 (cit. on p. 74).
- [175] J. J. Raftery. "Nonequilibrium Quantum Simulation in Circuit QED". en. PhD thesis. Princeton University, 2017 (cit. on p. 74).
- [176] Y. Sun, J. Ding, X. Xia, X. Wang, J. Xu, S. Song, D. Lan, J. Zhao, and Y. Yu. "Fabrication of airbridges with gradient exposure". In: *Applied Physics Letters*. 121, Publisher: American Institute of Physics, p. 074001. ISSN: 0003-6951 (cit. on p. 75).